Spring 5-15-2020

The Role of Gene Transcription and Inflammatory Cytokines in Bone Fracture Repair

Brandon Alan Coates
Washington University in St. Louis

WASHINGTON UNIVERSITY IN ST. LOUIS
School of Engineering and Applied Science
Department of Biomedical Engineering

Dissertation Examination Committee:
Matthew Silva, Chair
Roberta Faccio
Anthony French
Daniel Link
Lori Setton

The Role of Gene Transcription and Inflammatory Cytokines in Bone Fracture Repair

by

Brandon A. Coates

A dissertation presented to
The Graduate School
of Washington University in
partial fulfillment of the
requirements for the degree
of Doctor of Philosophy

May 2020
St. Louis, Missouri

Table of Contents

List of Figures v
List of Tables vii
Acknowledgements viii
Abstract of the Dissertation xi

CHAPTER 1: OVERVIEW OF FRACTURE REPAIR AND INFLAMMATION 1

1.1 The Skeleton and Bone Cells 1
1.2 Overview of the Fracture Repair Process 4
1.3 The Inflammatory Phase of Fracture Repair 6
1.4 Non-Union Fractures and Clinical Implications 9
1.5 Animal Models of Fracture Repair 10
1.6 Goals of the Dissertation 12

CHAPTER 2: A FORELIMB FATIGUE MODEL TO STUDY DAMAGE AND REPAIR IN OVARIECTOMIZED RABBITS 13

2.1 Abstract 13
2.2 Introduction 14
2.3 Methods 16
2.3.1 Animals 16
2.3.2 Forelimb Compression Model 17
2.3.3 Experiment 1: Biomechanical Assessment 17
2.3.4 Experiment 1: MicroCT Analysis 22
2.3.5 Experiment 1: Dynamic Histomorphometry 22
2.3.6 Experiment 2: Sub-Fracture Fatigue Loading and Fuchsin Staining 23
2.3.7 Experiment 3: Survival Fatigue Loading 24
2.3.8 Statistics 24
2.4 Results 25
2.4.1 The biomechanics of the forelimb are unchanged by OVX 25
2.4.2 No changes in cortical or cancellous bone are observed by microCT following OVX 26
2.4.3 Increased remodeling was observed in the ulna following OVX 28
2.4.4 Reliable creation of microdamage with sub-fracture fatigue loading was not achieved 30
2.4.5 Fatigue loading resulted in increased intracortical remodeling and periosteal bone formation 33
2.5 Discussion 36
2.6 Conclusions 39

CHAPTER 3: TRANSCRIPTIONAL PROFILING OF INTRAMEMBRANOUS AND ENDOCHONDRAL OSSIFICATION AFTER FRACTURE IN MICE 40

3.1 Abstract: 40
3.2 Introduction 41
3.3 Materials and Methods 44
3.3.1 Mice 44
3.3.2 Stress Fracture 45
3.3.3 Full Fracture 46
3.3.4 RNA extraction and sequencing 47

3.3.5 Validation of RNA-Seq data 49
3.3.6 Gene Ontology and Pathway Analyses 51
3.3.7 Callus Component Phenotyping 51
3.3.8 Histology 53
3.4 Results 55
3.4.1 RNA-seq Data Correlates to Previous Fracture Gene Expression Data 55
3.4.2 Dramatic Transcription Changes during Fracture Repair 57
3.4.3 Stronger Expression Changes in Full Fracture Repair 62
3.4.4 GO Term Analysis 65
3.4.5 Pathway Analysis 67
3.4.6 Callus Component Phenotyping 69
3.4.7 IHC of fracture callus 71
3.5 Discussion 74
3.6 Conclusions 81

CHAPTER 4: INTERLEUKIN-6 (IL-6) DEFICIENCY ENHANCES INTRAMEMBRANOUS OSTEOGENESIS FOLLOWING STRESS FRACTURE 82

4.1 Introduction 82
4.2 Methods 84
4.2.1 Mice 84
4.2.2 Full Fracture 84
4.2.3 Stress Fracture 85
4.2.4 MicroCT Analysis 86
4.2.5 Histology 87
4.2.6 Anabolic Tibia Loading 88
4.2.7 Primary Osteoblast Culture 89
4.2.8 RNA-sequencing 90
4.2.9 IL-6 deletion validation 91
4.3 Results 93
4.3.1 Knockout of IL-6 does not impact skeletal morphology 93
4.3.2 Global knockout of IL-6 does not impair bone formation in endochondral ossification 93
4.3.3 Global knockout of IL-6 increases callus and bone formation in intramembranous ossification 96
4.3.4 Global knockout of IL-6 does not alter immune cell recruitment in stress fracture repair 98
4.3.5 Global knockout of IL-6 decreases inflammatory and increases cell proliferation associated gene expression 100
4.3.6 Global knockout of IL-6 does not alter osteoclasts activity in stress fracture repair 103
4.3.7 Global knockout of IL-6 increases capacity for woven bone formation *in vivo* 104
4.3.8 Global knockout of IL-6 does not impact *in vitro* osteogenesis 108
4.3.9 PCNA staining is unchanged in IL-6 KO stress fracture callus 110
4.3.10 Condition deletion of IL-6 from osteoblasts or myeloid cells does not recapitulate the global knockout phenotype 111
4.4 Discussion 113
4.5 Conclusions 121

CHAPTER 5: CXCR2 DEFICIENCY DECREASES INTRAMEMBRANOUS OSTEOGENESIS FOLLOWING STRESS FRACTURE 122

5.1 Introduction 122
5.2 Methods 123
5.2.1 Mice 123
5.2.2 Full Fracture 124
5.2.3 Stress Fracture 125
5.2.4 MicroCT 126
5.2.5 Histology 127
5.2.6 Deletion efficiency validation with qPCR 127
5.3 Results 128
5.3.1 Cxcr2 KO mice have smaller body size but comparable skeletons to wild types 128
5.3.2 Cxcr2 knockout does not impair endochondral ossification following full fracture 129
5.3.3 Cxcr2 knockout impair intramembranous ossification following stress fracture 131
5.3.4 Cxcr2 knockout impaired neutrophil recruitment to stress fracture callus 133
5.3.5 LysM cKO mice do not phenocopy global knockout mice 135
5.4 Discussion 137

CHAPTER 6: CONCLUSIONS AND FUTURE DIRECTIONS 141

6.1 Conclusions 141
6.2 Future Directions 144

REFERENCES 147

List of Figures

Figure 1.1: Overview of Bone Cells and Their Roles in Skeletal Remodeling 2

Figure 1.2: Overview of Skeletal Anatomy 3

Figure 1.3: Endochondral and Intramembranous Ossification 5

Figure 1.4: Skeletal Injury Models. 11

Figure 2.1: Confirmation of OVX by uterine weight 16

Figure 2.2: Experimental designs and timelines 18

Figure 2.3: Experiment 1 - Biomechanics of the rabbit forelimb under monotonic loading 19

Figure 2.4: Experiment 1 - Biomechanics of the rabbit forelimb under cyclic loading 21

Figure 2.5: Experiment 1 - MicroCT evaluation of the cortical and cancellous compartments of the ulna 27

Figure 2.6: Experiment 1 - Dynamic histomorphometry of baseline remodeling in the rabbit ulna 29

Figure 2.7: Experiment 2 - Analysis of microdamage after sub fracture fatigue loading 31

Figure 2.8: Experiment 2 - Macrocrack formation following low and moderate fatigue 32

Figure 2.9: Experiment 3 - Response to survival sub fracture fatigue loading 34

Figure 2.10: Experiment 3 - Histology of survival fatigue loaded ulna 35

Figure 3.1: Experimental overview of fracture models, time points, and RNA-seq pipeline 45

Figure 3.2: Progression of healing of stress fracture and full fracture over time 54

Figure 3.3: Validation of RNA seq data 56

Figure 3.4: DEG trends across time 59

Figure 3.5: DEG overlap between time points 60

Figure 3.6: Comparison of DEGs between fracture types 61

Figure 3.7: Gene ontology analysis of DEGs 66

Figure 3.8: Pathway analysis of DEGs 68

Figure 3.9: Callus component phenotyping heat maps 70
Figure 3.10: Immune cell infiltration in fracture callus 72
Figure 3.11: Activation of PI3K-Akt signaling in stress fracture callus. 73
Figure 3.12: Comparison of stress fracture transcriptome to anabolic loading transcriptome. 78
Figure 3.13: Ion channels are downregulated following full fracture. 80

Figure 4.1: IL-6 KO is confirmed through ELISA 91
Figure 4.2: IL-6 KO did not impair skeletal morphology 94
Figure 4.3: IL-6 KO did not alter full fracture callus formation 95
Figure 4.4: IL-6 KO increased stress fracture callus formation 97
Figure 4.5: IL-6 KO did not alter immune cell recruitment after stress fracture 99
Figure 4.6: IL-6 KO had more proliferation and less inflammatory gene expression after stress fracture 102
Figure 4.7: IL-6 KO does not alter osteoclast numbers in stress fracture callus 103
Figure 4.8: Post-hoc tibia strain gauging revealed males and females were loaded to different strains 105
Figure 4.9: IL-6 KO mice have increased woven bone formation following anabolic loading 107
Figure 4.10: IL-6 KO does not impact in vitro osteogenesis 109
Figure 4.11: IL-6 KO does not alter PCNA staining following stress fracture 110
Figure 4.12: Conditional deletion of IL-6 with OC Cre or LysM Cre does not alter stress fracture callus formation. 112

Figure 5.1: Cxcr2 mice have lower body weights than wild type controls 128
Figure 5.2: Cxcr2 knockout mice have normal full fracture callus formation 130
Figure 5.3: Cxcr2 knockout mice form smaller callus with less bone following stress fracture 132
Figure 5.4: Cxcr2 knockout mice have reduced neutrophil recruitment after stress fracture 134
Figure 5.5: Figure 5.5: LysM-Cxcr2 mice did not recapitulate the global knockout phenotype 136

List of Tables

Table 2.1: Dynamic histomorphometry outcomes for baseline skeleton 28

Table 3.1: Genes used in comparison of qPCR data to RNA-seq data 50

Table 3.2: Genes used in callus component phenotyping 52

Table 3.3: Top up- and down-regulated DEGs for each injury and time point 64

Table 3.4: Genes displayed in comparison of ion channel expression 80

Table 4.1: Stress fracture calibration data for IL-6 mouse strains 85

Table 4.2: Top up- and down-regulated DEGs for each genotype and time point 101

Table 5.1: Stress fracture calibration data for Cxcr2 mouse strains 125

Table 5.2: Body weight adjusted values for MicroCT evaluation of baseline skeleton in Cxcr2 KO mice 129

Acknowledgements

I would like to begin by thanking my mentor and committee chair Matthew Silva for his invaluable guidance, support, and commitment over the course of my graduate school career. Thank you for being a steady presence and thoughtful advocate of my work, even as it felt like every repeated experiment brought another negative result.

Secondly, I would like to express my sincerest gratitude to Jennifer McKenzie, who I consider to be my second PI. Thank you for all the countless hours you spent teaching lab techniques, editing drafts of papers and posters, planning experiments, and constantly reminding me to wear my lab coat.

I would also like to thank all the other members of the Silva Lab group who have made my time at Washington University not only productive, but also incredibly enjoyable. Special thanks are due to my lab corner of Heather Zannit, Evan Buettmann, and Taylor Harris for their encouragement, both scientific and extracurricular, and for enduring my non-stop leg tapping and sometimes distracting antics. Thanks to Katie Hixon, for indoctrinating me into her workout cult, which was a much needed outlet from graduate school work. Also, thanks to Michael Brodt, Nicole Migotsky, Lisa Lawson, Chris Chermside-Scabbo, Pei Hu, and Susumu Yoneda for being supportive, enjoyable, and helpful co-workers throughout my time here. And lastly thanks to the unofficial Silva Lab member, Christian Weber, for his comradery and commiseration throughout course work, research projects, sports matches, and glasses of beer.

Many thanks are also due to my dissertation committee Lori Setton, Roberta Faccio, Daniel Link, and Anthony French for their guidance, recommendations, and thoughtful discussions throughout my thesis work.

The technical work presented in this dissertation would not be possible without the fantastic assistance from the staff of the Washington University Musculoskeletal Research Center. Especially Dan Leib, who assisted in microCT scanning and analysis, and Crystal Idelburg and Samantha Coleman, who processed and sectioned the histology slides. Other thanks are due to the Alafi Neuroimaging Core (S10 RR027552) for help with Nanozoomer histology imaging. Thanks to the Washington University Genome Technology Access Center (P30 CA91842 and UL1 TR000448) for processing RNA sequencing and Bo Zhang for help analyzing RNA-seq data. Thanks to Daniel Link for donation of Cxcr2 KO mice. Thanks to Phil Bayly and the T32 training program (T32 EB018266) for funding research and conference travel during my dissertation work. I am also grateful for the funding support from the National Institutes of Health (R01 AR050211, P30 AR057235, and P30 AR074992) which sponsored the majority of this work.

I wish to express my gratefulness for having a truly supportive family which has made my journey through graduate school possible. Endless thanks are due to my wonderful and compassionate wife, Ellen, who is always the fastest to celebrate my every victory, no matter how big or small, and whose continuous encouragement and reassurance was of my infinite benefit.

Further appreciation is owed to my sister Kelsey, my grandparents Max, Nancy, Dean, and Sharon, and all my aunts, uncles, cousins, and friends who provided respite from the doldrums of science and the optimism to believe that this all was achievable. Thanks are also due

to my in-laws, Jim and Mary, who have been so very supportive of my pursuits. Lastly, I would like to express my eternal indebtedness to my loving parents, Brad and Laura, who have always been my biggest fans and who instilled within me a deep seeded curiosity and love of discovery which has fueled my scientific pursuits.

Brandon Coates

Washington University in St. Louis

May 2020

ABSTRACT OF THE DISSERTATION

The Role of Gene Transcription and Inflammatory Cytokines in Bone Fracture Repair

by

Brandon Coates

Doctor of Philosophy in Biomedical Engineering

Washington University in St. Louis, 2020

Professor Matthew Silva, Chair

In most instances, the skeleton has a remarkable capacity for repair following injury. However, in 5 to 10% of patients, fractures fail to properly heal resulting in non-union. A need exists for a more comprehensive understanding of the complex biology of fracture repair, which involves the coordinated work of many cell types including osteoblasts, osteoclasts, and immune cells. Depending on the extent of injury, fractures will heal through either intramembranous bone formation, involving the direct formation of bone callus, or endochondral bone formation, featuring a cartilage intermediary prior to bone callus formation. Both processes begin with inflammation, which sets the stage for a successful repair cascade. However, the production of inflammatory cytokines and recruitment of immune cells in the early stages of fracture repair, and the implications for these processes on effective fracture repair remain incompletely understood.

For the first aim of the dissertation, we examined gene expression in response to injury across a broad range of time points for both intramembranous and endochondral bone formation. We used RNA sequencing to observe gene expression and immunohistochemistry to observe select protein expression throughout the early repair process. While some degree of overlap

existed, we observed divergent gene expression between intramembranous and endochondral bone formation, with each possessing a distinct transcriptome contributing to repair. An inflammatory reaction was present for both bone formation types, however endochondral repair had expression of inflammatory genes and recruitment of immune cells that were orders of magnitude greater than observed in intramembranous repair. Intramembranous repair was more enriched for genes associated with osteoblasts and bone formation and was uniquely enriched for PI3K-Akt signaling. This is likely reflective of the more simplified nature of bone formation in intramembranous repair – which does not require production of a cartilage intermediary callus. We also observed a dramatic downregulation of voltage gated ion channels in endochondral repair, which was not present in intramembranous repair.

For the second aim of this dissertation, we tested the involvement of *interleukin-6* (*IL-6*) in fracture repair. *IL-6* is a component of the inflammatory reaction to skeletal injury and has high upregulation in early callus tissue. We used an *IL-6* global knockout mouse (IL-6 KO) with two models of skeletal injury, full fracture and stress fracture, which heal through endochondral and intramembranous bone formation respectively. Full fracture repair was not altered in IL-6 KO mice. However, repair of stress fracture was enhanced in IL-6 KO mice, which had larger calluses and more bone formation than control animals. IL-6 KO did not alter osteoclast numbers or recruitment of the innate immune system in stress fracture callus. IL-6 KO mice had slight reductions in inflammatory signaling and higher expression of the bone anabolic protein *Wnt1* after injury. Furthermore, IL-6 KO animals displayed an increased ability to form woven bone when challenged with a non-injurious model of loading induced bone formation. Thus IL-6 KO directly affects the bone building potential of osteoblasts, allowing for the increased formation of bone.

For the third aim of this dissertation, we examined the CXC family of chemokines in skeletal repair through deletion of *CXC family receptor 2* (*Cxcr2*). Several members of the CXC chemokine family are among the most highly upregulated genes following skeletal injury. Despite this, their impact of fracture repair has not been reported. We used a global knockout mouse for *Cxcr2* (Cxcr2 KO) to study bone formation after full and stress fracture. The ability of Cxcr2 KO mice to form bone was unchanged following full fracture. However, after stress fracture Cxcr2 KO mice had a diminished capacity for repair, producing smaller calluses with less bone formation than control animals. Cxcr2 KO mice had blunted recruitment of neutrophils, the earliest responding immune cell to injury, within stress fracture callus. Thus, we concluded that the blunted immune response in Cxcr2 KO mice leads to the reduced capacity for bone formation.

This dissertation work provides insight into the transcriptional profile and inflammatory response of fracture repair following skeletal injury. We are hopeful that this work will benefit the planning of future research on fracture repair biology and provide insight for potential fracture therapeutics to aid in repair and prevent nonunion.

Chapter 1: Overview of Fracture Repair and Inflammation

1.1 The Skeleton and Bone Cells

Bone is a dynamic tissue that is continually remodeling to repair and replace old and damaged matrix. The main cell populations in bone include osteoblasts, osteoclasts, and osteocytes (Figure 1.1). Osteoblasts are bone cells from the mesenchymal lineage whose main role is the production of bone matrix [1]. Osteoclasts are multinucleated cells from the myeloid lineage which use enzymes to digest bone matrix [1]. Osteocytes are terminally differentiated osteoblasts which reside in the bone matrix and orchestrate the activities of osteoblasts and osteoclasts [2]. Bone remodeling is a coordinating activity which begins with osteoclasts removing damaged and old matrix and osteoblasts laying down replacement matrix [3]. Bone quality and quantity are both determined by the remodeling process, the proper balance of which helps protect the skeleton from the risk of fracture.

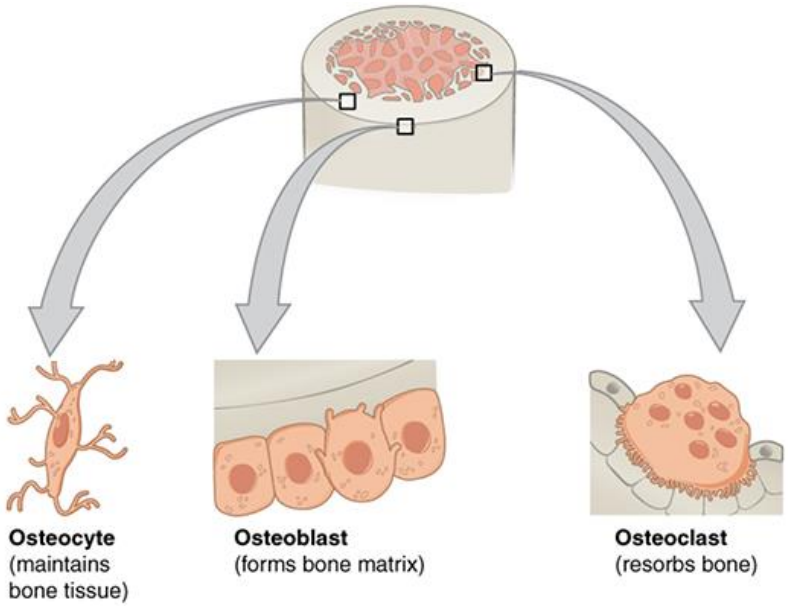

Figure 1.1: Overview of Bone Cells and Their Roles in Skeletal Remodeling. Osteoblasts reside on the bone surface and form new bone matrix. Osteoclasts also reside on the bone surface and digest and remove bone matrix. Osteocytes reside within the bone matrix and direct the activities of the osteoblasts and osteoclasts. Bone remodeling is a tightly coupled process involving all three of these cell types and must be balanced to maintain proper bone quality and quantity. Figure adapted from [4].

The skeleton consists of two distinct kinds of bone, cancellous and cortical (Figure 1.2). Cancellous bone, which resides primarily at the ends of long bones and within the vertebra, is spongy in design and is composed of small trabecular struts and rods. Cortical bone, which constitutes most of the length of long bones, is densely packed and organized bone. The cortical bone has two surfaces, the internal surface which faces the medullary space is covered by the endosteum, a thin fibrous layer. The periosteum covers the external surface of the bone and also serves as a reserve of osteoprogenitor cells which aid in skeletal maintenance and response to injury [4].

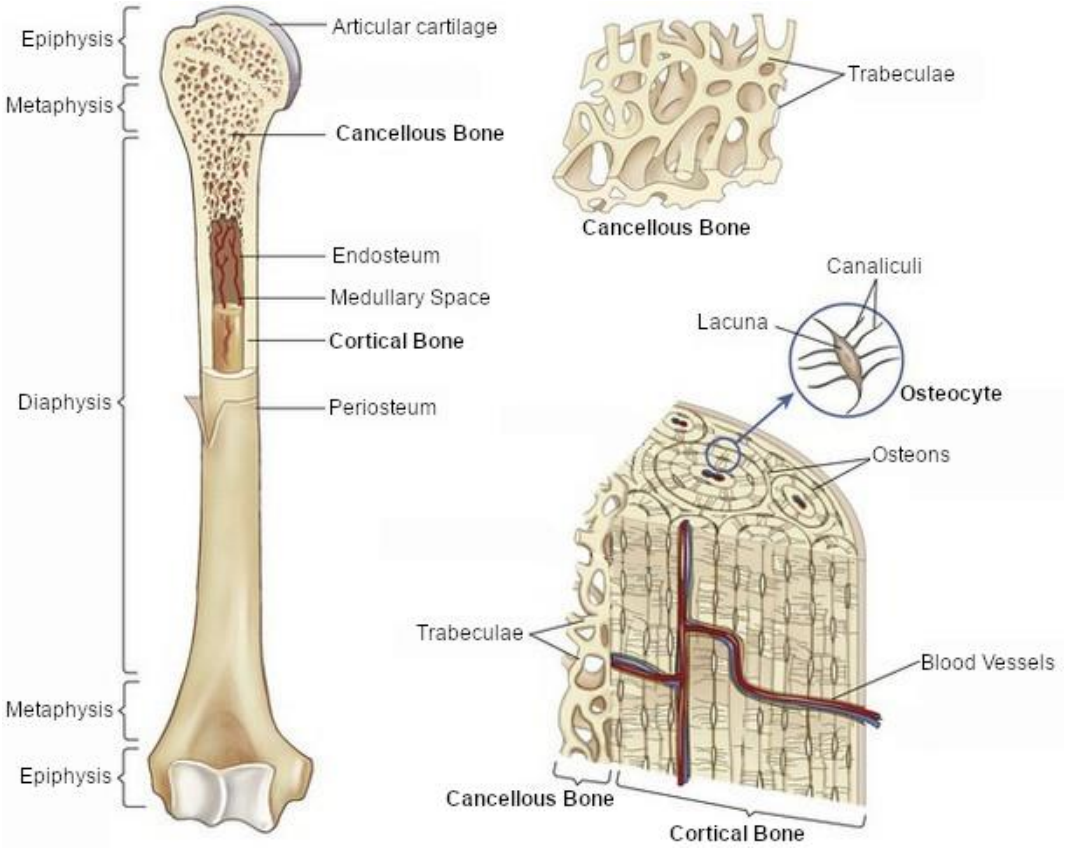

Figure 1.2: Overview of Skeletal Anatomy. The long bones of the skeleton are comprised of cancellous bone and cortical bone. Cancellous bone is the porous bone comprised of small strut like trabeculae and is primary located at the ends of the bone in the epiphysis and metaphysis regions. Cortical bone is densely packed bone which constitutes the middle portion of the long bones. Figure adapted from [6].

1.2 Overview of the Fracture Repair Process

Microdamage in bone tissue can occur through mechanical loading resulting from normal activity. This damage is typically repaired through skeletal remodeling. However, in events such as trauma or overuse, where damage formation outpaces remodeling, skeletal fractures will develop.

Bone has a remarkable capacity for regeneration, which can occur through two different mechanisms – endochondral ossification or intramembranous ossification (Figure 1.3). Endochondral ossification is believed to recapitulate the developmental process of long bone formation and features an initial inflammatory reaction, formation of a cartilage based intermediary soft callus, transition from the soft callus to a boney hard callus, and finally remodeling of the hard callus back to the original morphology of the pre-injury bone (Figure 1.3 A) [5]. On the other hand, intramembranous ossification is thought to recapitulate the development of the skull and craniofacial bones and features an inflammatory reaction, direct formation of a bone hard callus without a cartilage intermediary, and finally resolution of regeneration by remodeling of the callus back to the original morphology of bone (Figure 1.3 B) [6].

Two mechanisms help determine whether intramembranous or endochondral ossification occur following injury [7]. The first consideration is stability of the injury site. Injuries with greater stability will heal through intramembranous ossification. However, injuries with less mechanical stability heal through endochondral ossification. The second consideration (which also contributes to mechanical stability) is the amount of displacement generated by the injury. If the bone suffers no displacement, or undergoes surgical reduction to restore original anatomy, it

will be predisposed to intramembranous ossification [6]. However, if injury results in displacement between bone fragments, then endochondral bone formation is the most likely healing method.

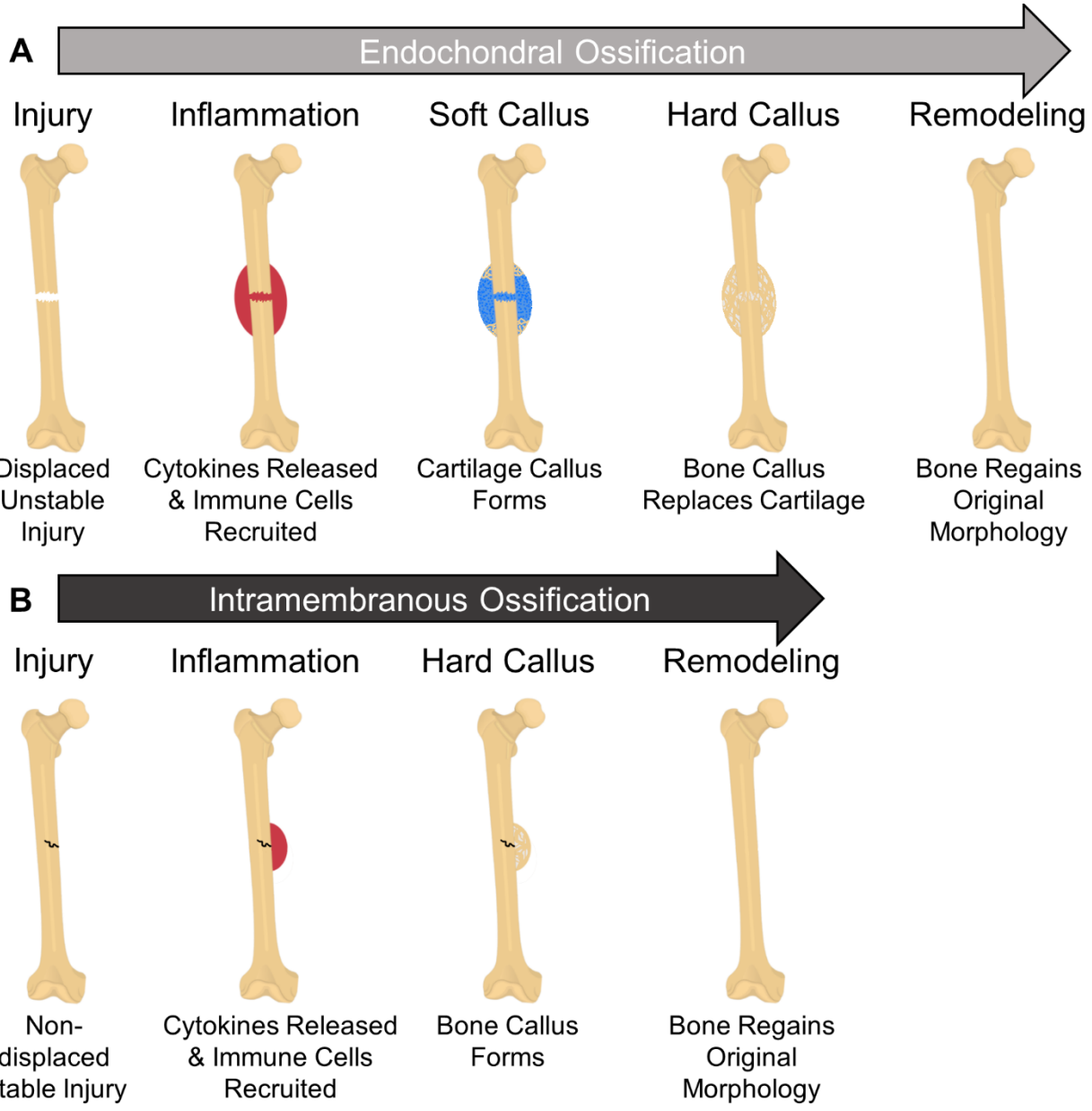

Figure 1.3: Endochondral and Intramembranous Ossification. Endochondral ossification (A) is the response to injuries causing displacement of the bone ends and mechanical instability. Endochondral repair begins with inflammation, soft callus formation, hard callus formation, and concludes with remodeling. Intramembranous ossification (B) is the response to injuries that cause little displacement of bone ends and are mechanically stable. Intramembranous repair begins with inflammation, followed by direct formation of a hard callus, and concludes with remodeling.

1.3 The Inflammatory Phase of Fracture Repair

Inflammation is the first response of the skeleton to damage and begins immediately following injury. During the inflammatory phase, the release of cytokines govern the earliest repair processes, including the recruitment of various types of immune cells which play a vital role in early fracture repair. Despite its importance in triggering the cascade of crucial healing events, this inflammatory response remains incompletely understood.

The inflammatory reaction involves a series of processes beginning with formation of a hematoma [8]. Immune cells are recruited to the injury site beginning immediately after injury. The first immune cells to arrive are neutrophils which dominate the earliest response [9]. Following neutrophils, monocytes and macrophages begin to arrive to the injured area [9]. Together, these cells help remove the fibrous matrix of the hematoma and any necrotic cells damaged from the injury [8]. The next phase of recruitment includes cells of the adaptive immune system and progenitors of osteoblasts and osteoclasts. Finally, the inflammatory reaction is resolved as the repair process moves into anabolic phases of callus formation [10].

This inflammatory phase sets the stage for a successful repair cascade and must be tightly controlled both in extent and time course. An imbalanced inflammatory reaction will lead to sub-optimal healing [10,11]. An inflammatory reaction which is too great can be detrimental to healing. This has been shown clinically in reports of hyper-inflammation in patients with polytrauma [12,13], obesity [14], or diabetes [15,16]. Conversely, an inflammatory reaction which is insufficiently strong will also lead to sub-optimal repair. This has been reported clinically in patients with HIV [17] and those treated with nonsteroidal anti-inflammatory drugs [18–20].

Therefore, a high clinical importance exists for a thorough understanding of the inflammatory phase of fracture healing and how it facilitates a successful repair cascade.

Recruitment of immune cells to the site of fracture plays an important role in the inflammatory phase of repair. Neutrophils are the first responding immune cells to skeletal injury and their absence results in sub-optimal repair [21]. Following neutrophils are monocytes and macrophages. Various subsets of macrophages play distinct roles in fracture repair. Depletion of bone resident macrophages reduced callus formation and bone deposition in a tibia fracture model [22]. M1 type macrophages help promote mineralization via oncostatin M production in a tibia injury model [23]. Finally, increasing the level of M2 macrophages in the fracture callus enhanced bone formation in a femur osteotomy model [24]. These innate immune cells help to activate the adaptive immune system, which also plays a role in fracture repair through by production and suppression of various cytokines [25–27].

Facilitating this inflammatory stage are a mix of cytokines and chemokines which are released in response to skeletal injury. Some of the most upregulated genes following skeletal injury include inflammatory cytokines such as interleukin-6 (IL-6), interleukin-1 (IL-1), prostaglandin-2 (Ptgs2), and members of the CXC family of chemokines (Cxcl1, Cxcl2, Cxcl3, & Cxcl5) [28,29]. The role that some of these factors play in fracture repair has been well documented. For example, Ptgs2 (aka Cox-2) has been shown to be a vital component of repair, with Cox-2 null mice having failed healing [30,31]. IL-1 has also been well studied in fracture, and likely plays important roles in hematoma development and osteoblast proliferation [32,33]. The roles that IL-6 and CXC family chemokines play in fracture repair are less understood.

The role of IL-6 in fracture repair has been reported to delay repair [34,35]. In particular, Yang et al describe that IL-6 null mice had reduced mineral content and increased cartilage content in fracture callus two weeks after a femur osteotomy [34]. These differences were not detected at six weeks post injury. Similarly, Wallace et al report IL-6 null mice to have reduced biomechanics of fracture callus two weeks after tibia fracture [35]. These differences were also absent by six weeks post-injury. In total, these reports indicate that knockout of IL-6 delays repair of full fractures. However, neither of these studies investigated changes in the inflammatory phase in the context of IL-6 knockout. Furthermore, both of these studies used models which primarily repair through endochondral ossification, leaving the impact of IL-6 knockout on intramembranous repair unstudied.

How the CXC family of chemokines contribute to fracture repair has not been thoroughly explored. A study of CXC receptor two (Cxcr2) null mice suggest a role for this family in bone development and skeletal repair [36]. Bischoff et al. report Cxcr2 null mice had smaller body weights and body length. MicroCT analysis revealed reduced trabecular and cortical bone density revealing a potential role for Cxcr2 in skeletal development. These investigators used a cranial defect model to probe how Cxcr2 knockout impacts skeletal repair. They report a reduced capacity for bone formation in knockout mice suggesting a putative role for Cxcr2 in skeletal repair.

1.4 Non-Union Fractures and Clinical Implications

Skeletal fractures embody a substantial clinical problem. About 16 million fractures occur annually in the U.S. – equating to a fractured bone every 2 seconds [37]. Most of these injuries will heal without major complications. However, an estimated 5 to 10% of fractures will result in non-union [38]. Non-unions are fractures that never successfully repair and are unable to regain the mechanical stability of intact bone. They are defined as the cessation of the repair process without a bridging of the fracture gap [39]. Non-unions require additional interventions by clinicians and are often treated through complicated surgical procedures [40]. Many comorbidities are associated with non-unions, including general risk factors such as old age, poor diet, and cigarette smoking, and local risk factors such as fracture type, infection, and polytrauma [41]. However, the precise pathogenesis of non-unions remains elusive and could be a failure of any of the several key phases of repair.

The medical treatment of fractures and non-unions represent a sizeable economic burden on the healthcare system of the U.S. The direct treatment of fractures is estimated to cost $40 billion in the U.S. each year [42]. Non-unions typically cost more than twice as much to effectively treat as union fractures [40]. It is estimated that 60 million work days are lost annually due to fracture – an amount more than double what is lost to heart disease and stroke combined [42]. Beyond the economics, fractures have an incredibly detrimental effect on overall health. This is especially true in elderly patients. Following an osteoporotic fracture, patients have increased morbidity, mortality, and subsequent fracture risks [43].

Therefore, a clinical need exists for a better understanding of the complex biology of fracture repair. Preclinical evaluations which provide insight into post-injury bone formation could be very valuable and may better inform clinical decisions and interventions for fractures and non-unions.

1.5 Animal Models of Fracture Repair

In order to study the complex biological processes involved in fracture repair, animal models are commonly used. In particular, murine models of fracture are useful due to the widespread use of transgenic animals which provide the ability to study the involvement of specific genes and cell types in fracture repair.

Our research group commonly uses two different skeletal injury models in order to study bone formation (Figure 1.4). In order to examine endochondral ossification, we use a murine femur full fracture model [28,44]. This model is defined by a transverse, fully displaced crack across the mid-diaphysis of the femur initiated through overt overloading of the bone by 3-pt bending. This injury proceeds through the various phases of endochondral repair, including inflammation, soft callus, hard callus, and remodeling.

To study intramembranous ossification, we use a murine ulna stress fracture model. This model is defined by an oblique, non-displaced crack within the diaphysis of the ulna. Cyclic loading is used to initiate the crack through fatigue. This injury proceeds through the various phases of intramembranous repair.

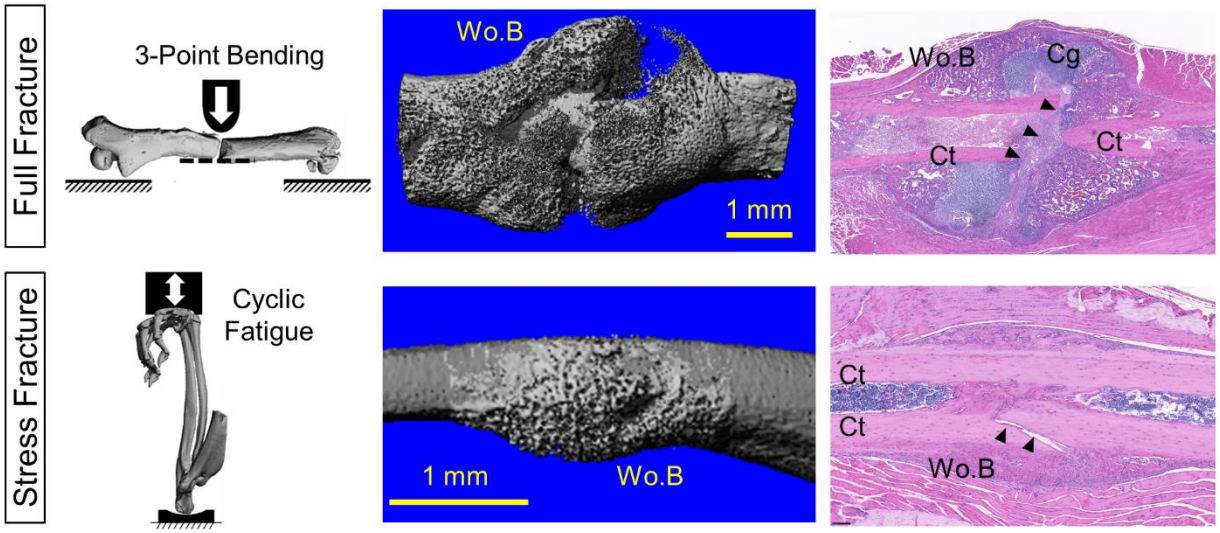

Figure 1.4: Skeletal Injury Models. Full fractures were created using 3-point bending. MicroCT reconstruction 14 days after fracture depicts woven bone (Wo.B) formation in the callus surrounding injury site. Longitudinal histology image of day 14 full fracture callus, stained with hematoxylin and eosin shows original cortical bone (Ct), woven bone and cartilage (Cg) in the callus surrounding the original crack (▲). Stress fractures were created using cyclic fatigue of the mouse ulna. MicroCT reconstruction depicts woven bone formation surrounding crack at day 7. Longitudinal histology of day 7 stress fracture callus shows woven bone formation in callus around original crack (▲).

1.6 Goals of the Dissertation

The treatment of skeletal fractures and non-unions represent an important clinical challenge. A need exists for more basic science research which will help detail the complex biology of fracture repair. This dissertation will seek to 1) Describe gene expression across several time points for two types of skeletal repair and 2) investigate how interleukin-6 and CXC family chemokines contribute to osteogenesis as components of the inflammatory phase of fracture repair. By better understanding how gene expression is altered during intramembranous and endochondral ossification, we hope to document the important genes and signaling pathways which are critical to each repair modality and provide inspiration for more detailed examination of these models. Through exploration of IL-6 and the CXC family, we hope to better understand the inflammatory phase of fracture repair and how it contributes to successful repair.

Chapter 2: A Forelimb Fatigue Model to Study Damage and Repair in Ovariectomized Rabbits

2.1 Abstract

Microdamage accumulates in bone matrix from normal activity and is repaired through bone remodeling. Conditions such as osteoporosis and treatment with antiresorptives, such as bisphosphonates, can influence this remodeling process. In order to study microdamage accrual and repair in the context of osteoporosis and Haversian bone microstructure, we set out to modify the rabbit forelimb fatigue model. New Zealand white rabbits received either ovariectomy (OVX) or sham surgeries and were used for forelimb fatigue loading. OVX was confirmed to induce increased intracortical and periosteal bone labeling as seen in dynamic histomorphometry of the ulna, although bone mass was not affected. OVX and sham animals were compared in non-survival fatigue loading for monotonic and cyclic loading parameters and were found to have similar mechanical characteristics. Two levels of fatigue loading were then used on OVX rabbit forelimbs to examine if dose dependent microdamage accrual could be achieved. However, neither group showed increased damage burden as compared to non-loaded controls. Survival fatigue loading was able to demonstrate increased intracortical remodeling and periosteal lamellar bone formation in loaded limbs, although we did not observe basic multicellular units or microdamage-targeted remodeling. In summary, we adapted the rabbit forelimb fatigue model to accommodate OVX animals. However, loading parameters that could induce repeatable microdamage burden were not identified. Thus, while increased intracortical

remodeling and periosteal bone formation were induced by our fatigue loading regimen, we did not establish conditions to allow future study of the interactions between microdamage accrual and repair.

2.2 Introduction

During activities such as walking, running, and jumping, the skeleton withstands mechanical loads and slowly accumulates microdamage within the bone matrix [45]. This microdamage is eventually remodeled by osteoclasts and osteoblasts [46,47]. However, if microdamage accrual is too rapid, or repair is too slow, microdamage can coalesce into macrodamage, such as stress fractures and insufficiency fractures [48–50]. This balance can be additionally complicated by osteoporosis, a disorder characterized by low bone mass afflicting upwards of 200 million people worldwide [51]. Post-menopausal osteoporosis increases resorption of bone matrix, thus altering a critical component of microdamage repair [52]. The most common treatment for osteoporosis, bisphosphonate drugs, also alters the critical balance of bone remodeling by limiting resorption. This can paradoxically increase risk for rare complications such as atypical femoral fracture [53–56]. The interaction between osteoporosis, damage accumulation, and remodeling suppression that contribute to atypical femur fractures is not well understood. Animal models to study the balance between microdamage accrual and repair, and how osteoporosis and bisphosphonates may alter this balance, could help address this issue.

To date, the study of microdamage accrual and repair has primarily been conducted using small rodent models [57–61]. However, we propose a rabbit model could be advantageous due to

the presence of Haversian bone structures in rabbit cortical bone which more closely resemble human bone morphology than mouse or rat [62,63]. These osteon bone structures are important contributors of both where and how microdamage can accumulate and be repaired, and therefore could be important components of a clinically relevant model [64,65]. Other desirable characteristics of rabbits include their responsiveness to ovariectomy (OVX), an inducible model for osteoporosis [66–68], and to common osteoporosis treatments, such as bisphosphonates [67–69]. Using a rabbit model could provide the capability to study microdamage repair in osteonal, osteoporotic, and bisphosphonate treated bone.

Preceding work from our group developed the rabbit axial forelimb compression model as a tool for creating fatigue macrodamage/stress fracture [70]. While useful for the study of stress fracture healing (injury response), this model needs further adaptation to be of use in the study of pre-injury microdamage accrual and repair. Therefore, we set out to modify this model for sub-fracture fatigue, in order to study microdamage accumulation and remodeling.

The goals of this work were to further develop a rabbit forelimb fatigue model which could incorporate osteoporotic animals, induce repeatable and controllable amounts of microdamage with sub-fracture fatigue loading, and to describe the intracortical repair response following loading.

2.3 Methods

2.3.1 Animals

Working within an IACUC approved protocol, a total of 43 female New Zealand White rabbits (Covance) were used. Ovariectomy (OVX) or sham procedures were performed by Covance on 6 month old rabbits. Animals were then shipped to Washington University and aged 4 months to allow osteoporotic effects to develop. Animals were single housed on a 12:12 light/dark schedule. At 10 months age, rabbits were used for experiments; average weight was 4.1 kg (± 0.4 kg) at time of experiments. OVX was confirmed at time of sacrifice through reduction in uterine weight and absence of ovaries by visual inspection (Figure 2.1).

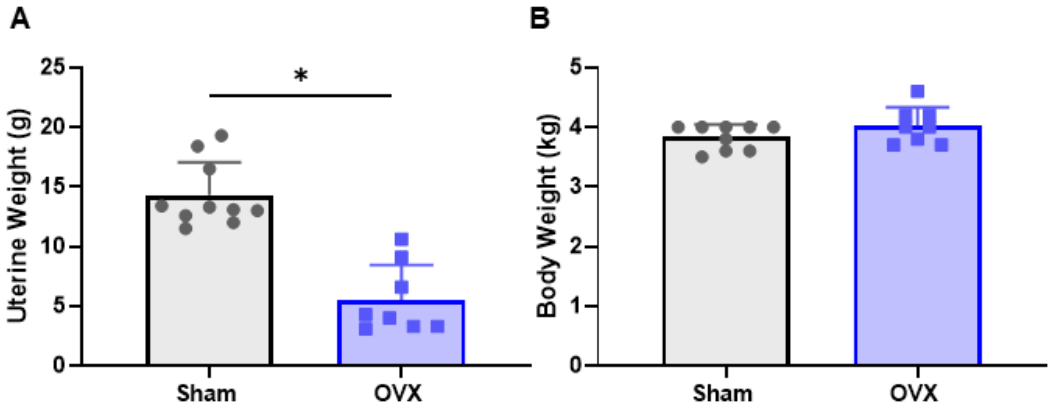

Figure 2.1: Confirmation of OVX by uterine weight. The uterus of each rabbit was dissected at time of sacrifice and weighed. **(A)** Reduced weight in the OVX group was confirmation of successful OVX induced estrogen withdrawal. **(B)** Body weight for the rabbits were consistent across groups regardless of surgical group. Asterisk (*) denotes $p < 0.05$, n = 8-10/group.

2.3.2 Forelimb Compression Model

All loading procedures were performed in vivo. Rabbits were administered anesthesia (isoflurane) and were intubated and ventilated throughout the session. The forelimbs were secured in a custom loading fixture at the olecranon and carpus on a material testing machine (Instron Dynamight) as previously described [70]. After application of a 10 N pre-load, monotonic or cyclic loading was applied through an actuator and forces were measured using a load cell. For non-survival loading, animals were euthanized (sodium pentobarbital overdose, 150mg/kg i.v.) immediately following loading. For survival loading, animals were administered buprenorphine (0.05 mg/kg, s.c.) for analgesia and were returned to normal cage activity until sacrifice.

2.3.3 Experiment 1: Biomechanical Assessment

Eighteen rabbits (8 OVX, 10 Sham) were used to determine the effects of OVX on the rabbit forelimb (Figure 2.2 A). For each rabbit, a non-survival bout of bilateral loading was performed. One forelimb underwent monotonic loading and the other was subsequently used for cyclic loading. For monotonic loading, a displacement ramp (0.5 mm/s) was applied until complete fracture of the forelimb. Stiffness was calculated as the slope of the force-displacement curve, ultimate force was the highest force reached during the test, and work to fracture was calculated as the area under the force displacement curve (Figure 2.3 A).

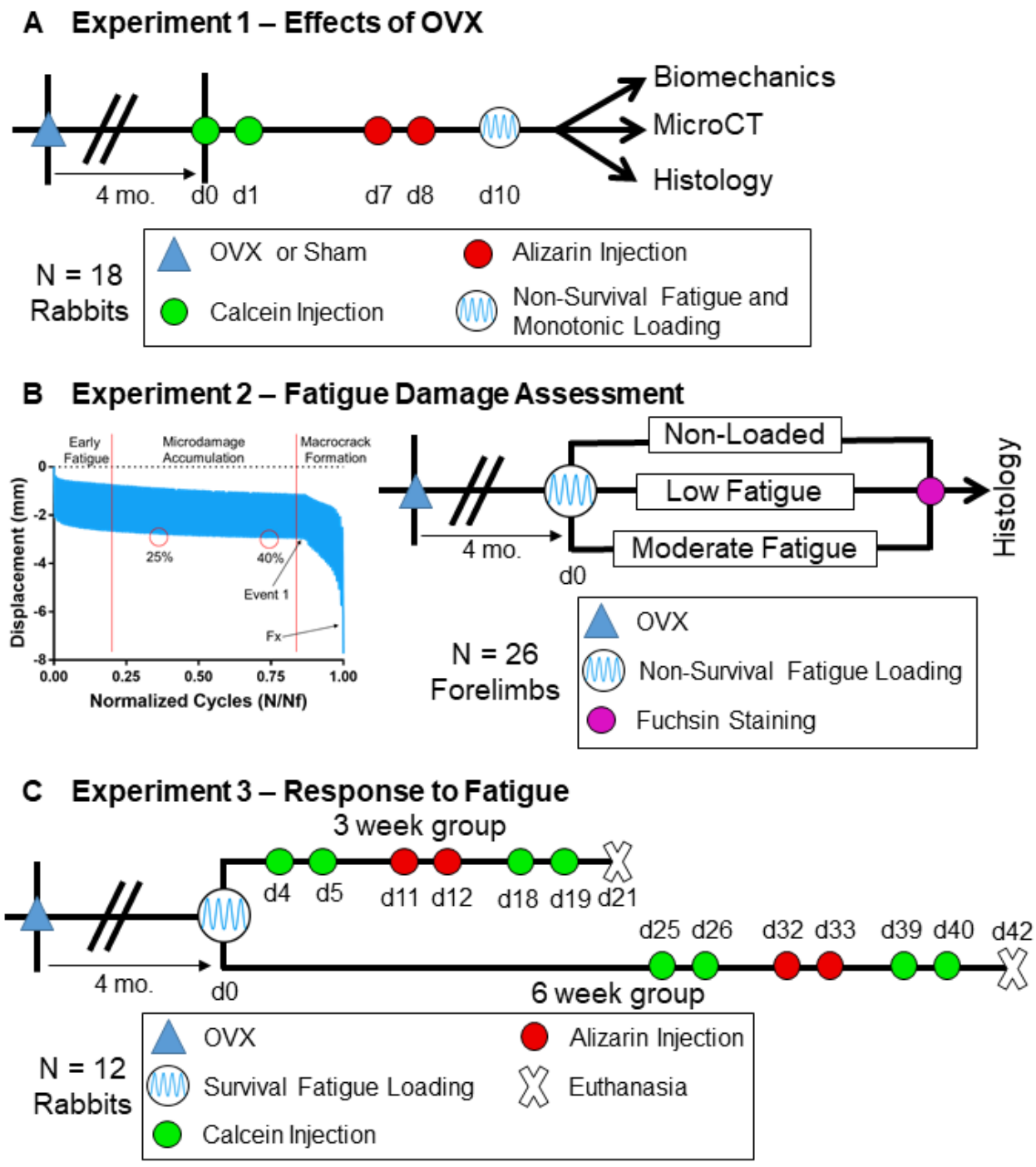

Figure 2.2: Experimental designs and timelines. For all studies, 6 month old female New Zealand white (NZW) rabbits underwent either ovariectomy (OVX) or sham operation and were aged an additional 4 months before beginning the experiment. **(A)** For Experiment 1, non-survival monotonic and fatigue loading was performed to ascertain forelimb mechanics in OVX and sham animals. Bone structure and bone formation were assessed by microCT and dynamic histomorphometry, respectively. **(B)** For Experiment 2, non-survival fatigue loading of either "low" or "moderate" amounts was used to study microdamage accumulation in OVX bone. **(C)** For Experiment 3, survival fatigue loading was used to study the response of the skeleton to moderate fatigue loading.

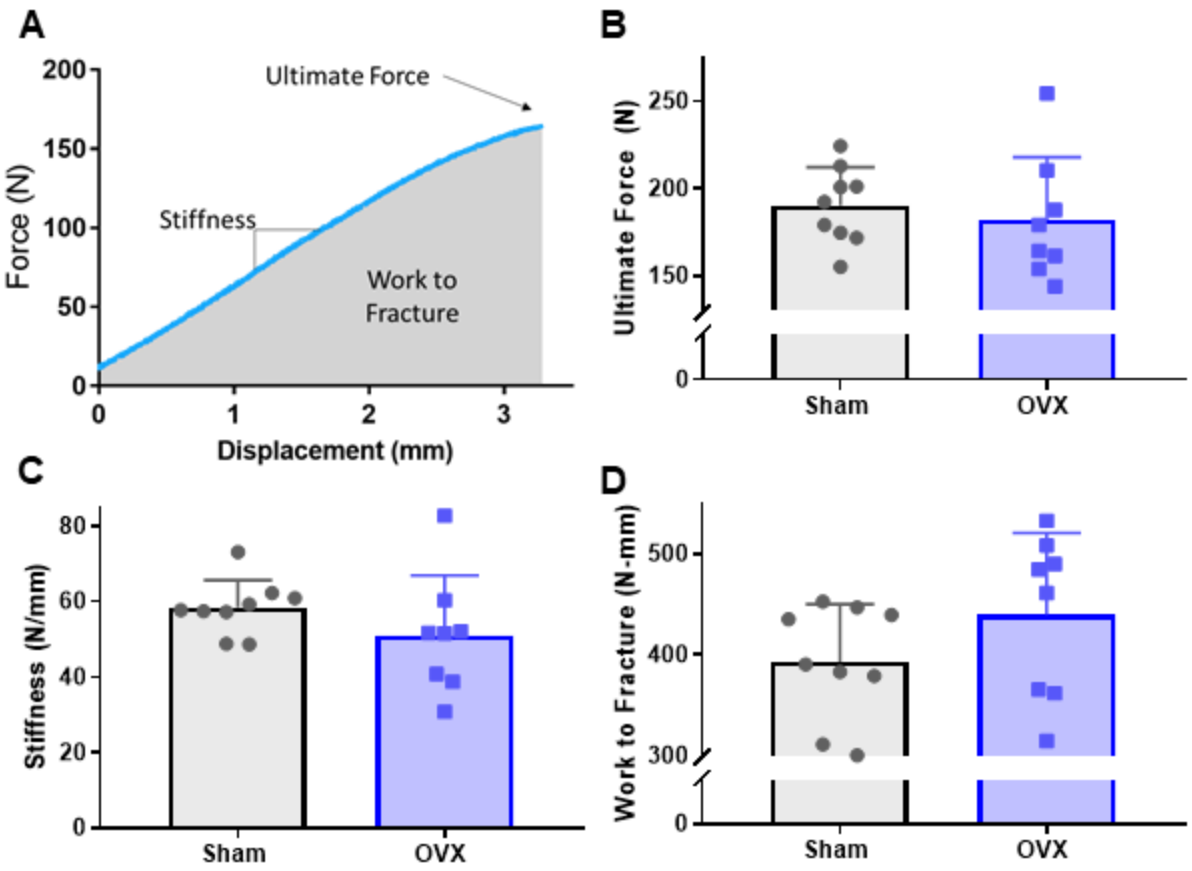

Figure 2.3: Experiment 1 - Biomechanics of the rabbit forelimb under monotonic loading. (A) A typical monotonic loading curve illustrating how stiffness, ultimate force, and work to fracture are obtained from the force-displacement curve. Values for ultimate force **(B)**, stiffness **(C)**, and work to fracture **(D)** did not differ between sham and OVX groups. n = 8-10/group.

Cyclic loading was then performed until complete fracture by a force controlled haversine wave (2 Hz) at 75% of the ultimate force from monotonic loading. Baseline stiffness ($K_{baseline}$) and baseline displacement ($D_{baseline}$) were calculated at the tenth cycle, event 1 displacement (D_{E1}) was calculated at the inflection point of the displacement-time plot, and failure stiffness (K_{fail}) and failure displacement (D_{fail}) were calculated at the last full cycle before fracture (Figure 2.4 A). Stiffness measurements were peak-to-peak displacement divided by applied force. Displacement to event 1 was the distance between D_{E1} and $D_{baseline}$, displacement to fracture was the distance between D_{fail} and $D_{baseline}$, and normalized fracture stiffness was the ratio of K_{fail} to $K_{baseline}$.

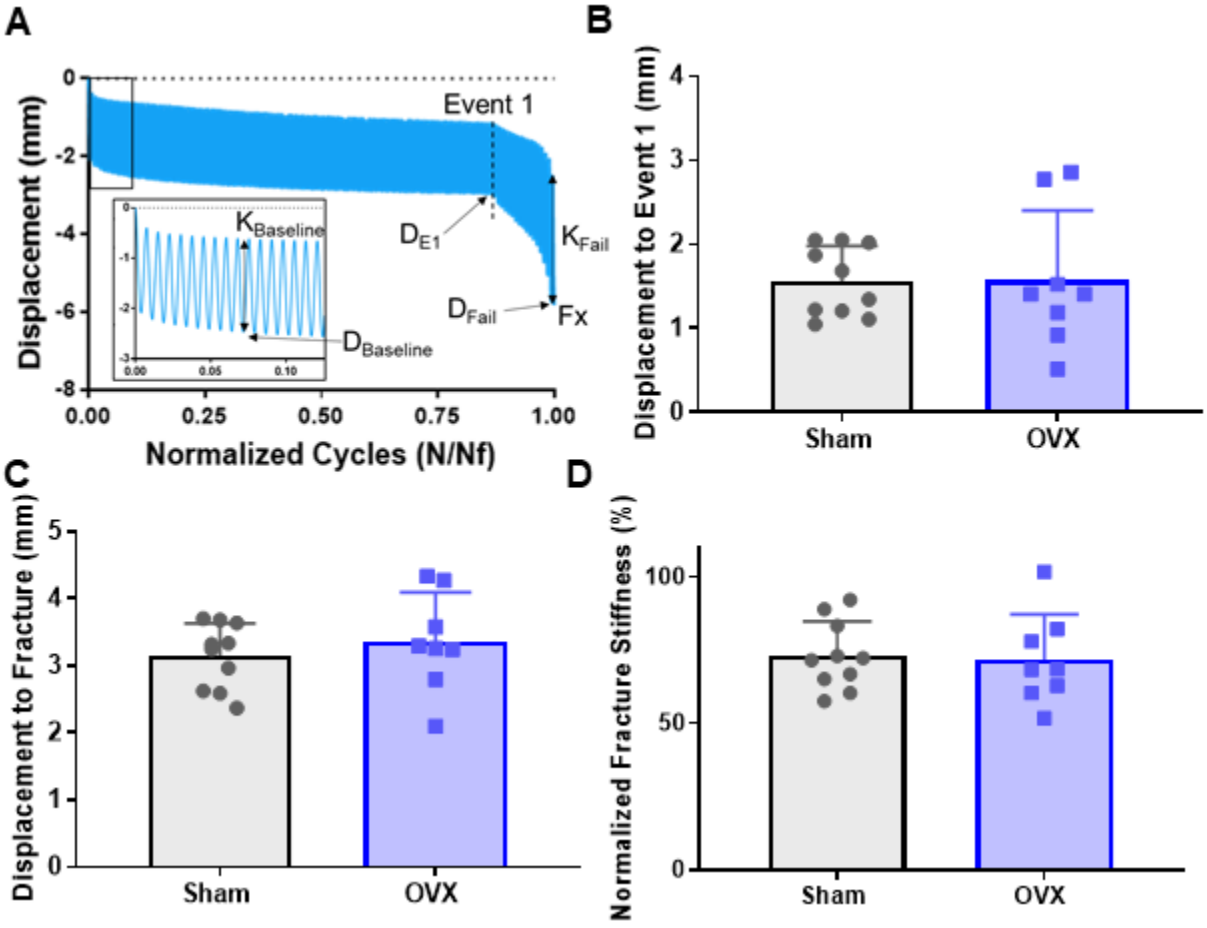

Figure 2.4: Experiment 1 - Biomechanics of the rabbit forelimb under cyclic loading. (A) A typical cyclic loading curve illustrating how baseline stiffness ($K_{baseline}$), baseline displacement ($D_{baseline}$), event 1 displacement (D_{E1}), failure stiffness (K_{Fail}), and failure displacement (D_{Fail}) are obtained from the displacement-cycle curve. Values for displacement to Event 1 **(B)**, displacement to fracture **(C),** and normalized fracture stiffness **(D)** did not differ between sham and OVX groups. n = 8-10/group.

2.3.4 Experiment 1: MicroCT Analysis

Following non-survival loading, forelimbs of OVX and sham-operated rabbits were scanned at a region away from the damaged region using microCT (Scanco VivaCT). Dissected ulnas were embedded in 3% agarose and imaged at 75 kVp, 300 ms integration time, and voxel size of 17.5 μm. Analysis of the cortical bone was performed on 125 slices (2.2 mm) in the ulnar diaphysis 30 mm distal to the olecranon, and analysis of the cancellous bone was performed on 125 slices in the proximal ulna beginning distal to the growth plate.

2.3.5 Experiment 1: Dynamic Histomorphometry

To assess baseline remodeling in OVX and Sham rabbits, calcein injections (10 mg/kg, i.v.) were delivered at day 0 and day 1, alizarin injections (25 mg/kg, i.v.) were administered on day 7 and day 8, and rabbits were euthanized on day 10 (Figure 2.2A). Following microCT scans, a 10 mm segment of each ulna was cut from the ulna diaphysis beginning at 35% of the ulna length from the olecranon, again selecting an area of cortical bone outside of the fractured region. Ulnar samples were then embedded in methyl methacrylate and 100 μm sections were cut from the ulna mid-diaphysis using a saw-microtome (Leica SP1600). Sections were polished using sandpaper to a final thickness of 30-40 μm and imaged as a series of 20X magnification images to capture the entire ulna (Olympus IX51). Individual images were then compiled into a single merged image (Microsoft Image Composite Editor) and analyzed (Bioquant 2016) for bone formation parameters [71].

2.3.6 Experiment 2: Sub-Fracture Fatigue Loading and Fuchsin Staining

Microdamage produced by sub-fracture fatigue loading was assessed (Figure 2.2 B). Forelimbs were cyclically loaded at 2 Hz to 130 N, which was 75% of the average ultimate force from experiment 1. We wanted to select levels of fatigue which were advanced enough to create microdamage, but before the threshold for macrocrack, or stress fracture, formation (event 1, Figure 2.4 A) [70]. Therefore, we selected two stopping displacements to test levels of fatigue for microdamage formation. The average displacement to fracture for rabbits was 3.24 mm (Figure 3C) and the average displacement to "event 1" was 1.57 mm. Therefore, displacements of 25% (0.81 mm) and 40% (1.30 mm) of the displacement to fracture were chosen (Figure 2.2 B). The 25% displacement was termed "low fatigue" and the 40% displacement was termed "moderate fatigue".

Eleven OVX rabbits (n = 22 forelimbs) underwent non-survival, bilateral loading and each forelimb was randomly assigned to the non-loaded, low-fatigue, or moderate-fatigue group (n = 6-8/group; Figure 2.2 B). Following sacrifice, forelimbs were processed for en bloc fuchsin staining on 25 mm segments of ulna cut to center around the average fracture location from experiment 1 (59% of normalized length). Ulnar samples were infiltrated with fuchsin through sequential 24-hour baths in 1% fuchsin solutions in 80% ethanol, 90% ethanol, and 100% ethanol [72]. Stained bones were then embedded in plastic and histology slices were cut and imaged (as above, Section 2.3.5). Diffuse damage and linear microcracks, two distinct kinds of microdamage, were quantified for one section from each ulna.

2.3.7 Experiment 3: Survival Fatigue Loading

Twelve OVX rabbits were used for survival, unilateral fatigue loading to a moderate fatigue level (1.30 mm). Right forelimbs were loaded and left forelimbs were used as non-loaded controls. Rabbits were randomly assigned to either a 3 or 6 week survival group (Figure 2.2 C). For the 3 week group, calcein was administered on consecutive days beginning on day 4 and day 18 and alizarin was administered on consecutive days beginning on day 11. Rabbits were sacrificed on day 21 after loading and bones were processed for plastic (n = 3) or paraffin (n = 3) embedded histology. For the 6 week group, calcein was administered on consecutive days beginning on day 25 and day 40 and alizarin was administered on consecutive days starting on day 32. Rabbits were sacrificed on day 42 after loading and forelimbs were processed for plastic (n = 3) or paraffin (n = 3) embedded histology. Plastic embedded histology was processed for dynamic histomorphometry to observe loading induced bone formation and microdamage induced intracortical remodeling. Ulnas for paraffin histology were decalcified by 14 days of 14% EDTA treatment prior to embedding. Thin sections were stained with hematoxylin and eosin and were imaged using a Nanozoomer slide scanner (Hamamatsu) at 20X magnification.

2.3.8 Statistics

Data is represented throughout as mean with error bars of one standard deviation. All statistical tests were performed using Prism software (GraphPad Prism 8.1.1). Due to non-normal distributions in data, all comparisons between sham and OVX were performed with unpaired non-parametric Mann-Whitney tests. In order to compare between non-loaded, low fatigue, and moderate fatigue groups for levels of microdamage Kruskal-Wallis tests with multiple

comparisons were performed. Bone remodeling parameters in survival fatigue model were analyzed with 2-way repeated measure ANOVA in order to account for paired nature of results and multiple time points. Significance was considered to be $p < 0.05$ for all tests.

2.4 Results

2.4.1 The biomechanics of the forelimb are unchanged by OVX

Forelimbs from sham and OVX rabbits did not have significant differences in biomechanics under either monotonic or fatigue loading (Figures 2.3 & 2.4). Ultimate force and stiffness were not different between OVX and Sham (Figure 2.3 B & C). Work to fracture had a slight, but non-significant increase following OVX ($p = 0.184$; Figure 2.3 D). Similarly, there were no differences between groups with cyclic loading in displacement to event 1 (Figure 2.4 B), displacement to fracture (Figure 2.4 C), and normalized fracture stiffness (Figure 2.4 D). The average number of cycles to fracture was 9,405 ± 8,385 cycles for sham and 8,243 ± 8,245 cycles for OVX. The average location of fracture was at 59% of the normalized length of the ulna.

2.4.2 No changes in cortical or cancellous bone are observed by microCT following OVX

MicroCT revealed no difference between OVX and sham rabbits in cortical bone parameters such as bone area, total area, medullary area, cortical thickness or tissue mineral density (Figure 2.5 A). Likewise, no differences were detected in cancellous bone parameters such as bone volume fraction, trabecular thickness, trabecular number, trabecular separation, and volumetric bone mineral density (Figure 2.5 B).

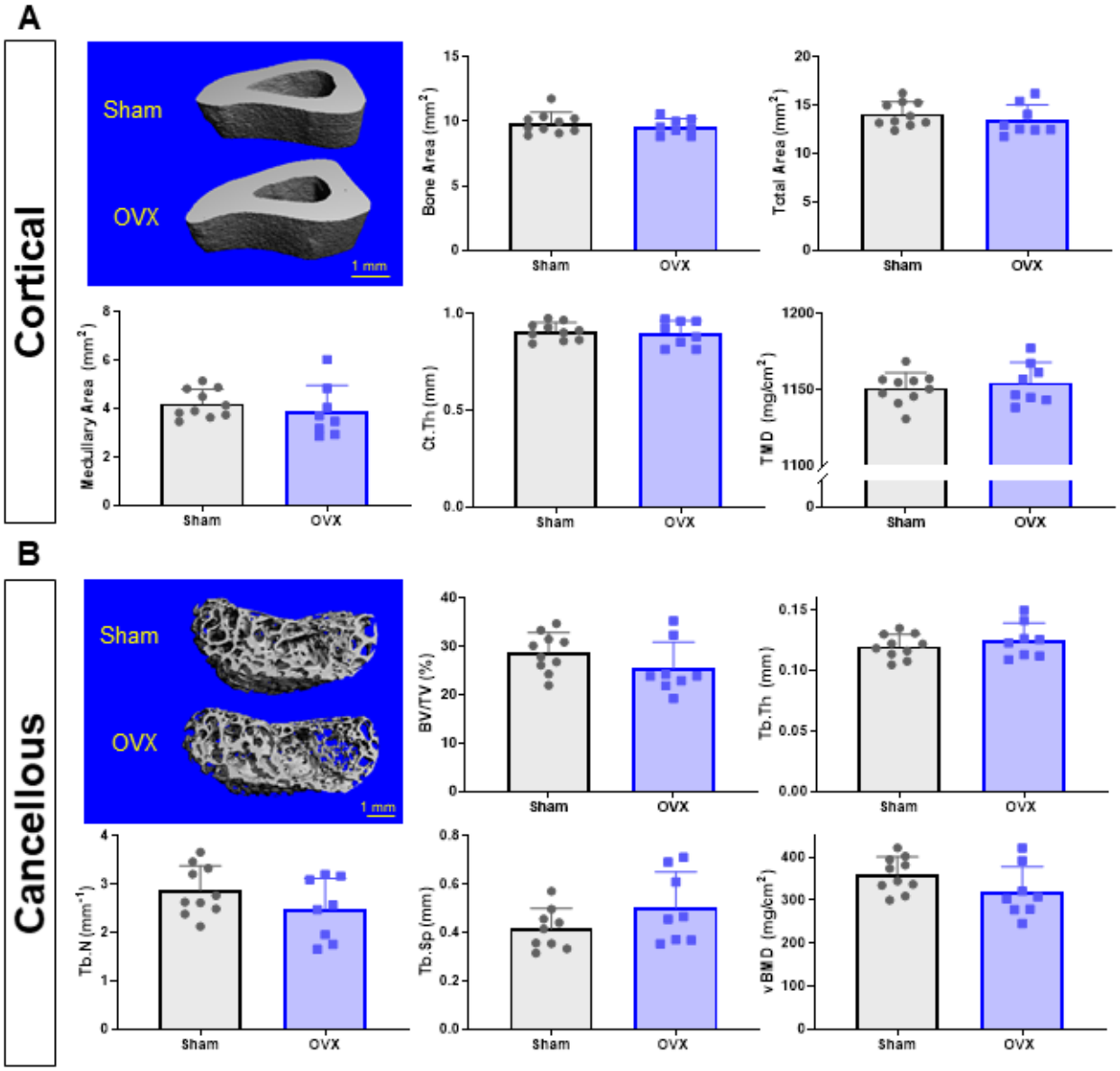

Figure 2.5: Experiment 1 - MicroCT evaluation of the cortical and cancellous compartments of the ulna. **(A)** A 2.2 mm segment of the ulnar diaphysis was analyzed to obtain properties of the cortical bone. Parameters including bone area, total area, medullary area, cortical thickness (Ct.Th), and tissue mineral density (TMD) did not differ between groups. **(B)** A 2.2 mm segment of the proximal ulna was analyzed to obtain cancellous bone properties. Parameters such as bone volume/total volume (BV/TV), trabecular thickness (Tb.Th), trabecular number (Tb.N), trabecular separation (Tb.Sp), and volumetric bone mineral density (vBMD) did not differ between groups. n = 8-10/group.

2.4.3 Increased remodeling was observed in the ulna following OVX

Using dynamic histomorphometry we observed more calcein and alizarin labeling in the ulna of OVX rabbits than sham rabbits (Figure 2.6 A & B). There were significant increases in labeled osteons (Figure 2.6 C), and periosteal mineralizing surface, mineral apposition rate, and bone formation rate (Figure 2.6 D-F). No difference was seen in endocortical parameters (Table 2.1).

Table 2.1: Dynamic histomorphometry outcomes for baseline skeleton.

	Intracortical	Periosteal			Endocortical		
	Lb.On (#/section)	MS/BS (%)	MAR (μm/d)	BFR ($\mu m^3/\mu m^2/d$)	MS/BS (%)	MAR (μm/d)	BFR ($\mu m^3/\mu m^2/d$)
Sham (n=10)	0.50 ± 0.71	5.87 ± 3.51	0.31 ± 0.99	0.03 ± 0.08	21.12 ± 13.85	1.40 ± 1.37	0.38 ± 0.45
OVX (n=8)	4.42 ± 5.71	27.57 ± 17.79	1.60 ± 0.87	0.54 ± 0.47	21.95 ± 7.90	2.22 ± 0.94	0.49 ± 0.23
	p = 0.006	p = 0.019	p = 0.001	p = 0.001	p = 0.999	p = 0.156	p = 0.410

Values are displayed as mean ± standard deviation

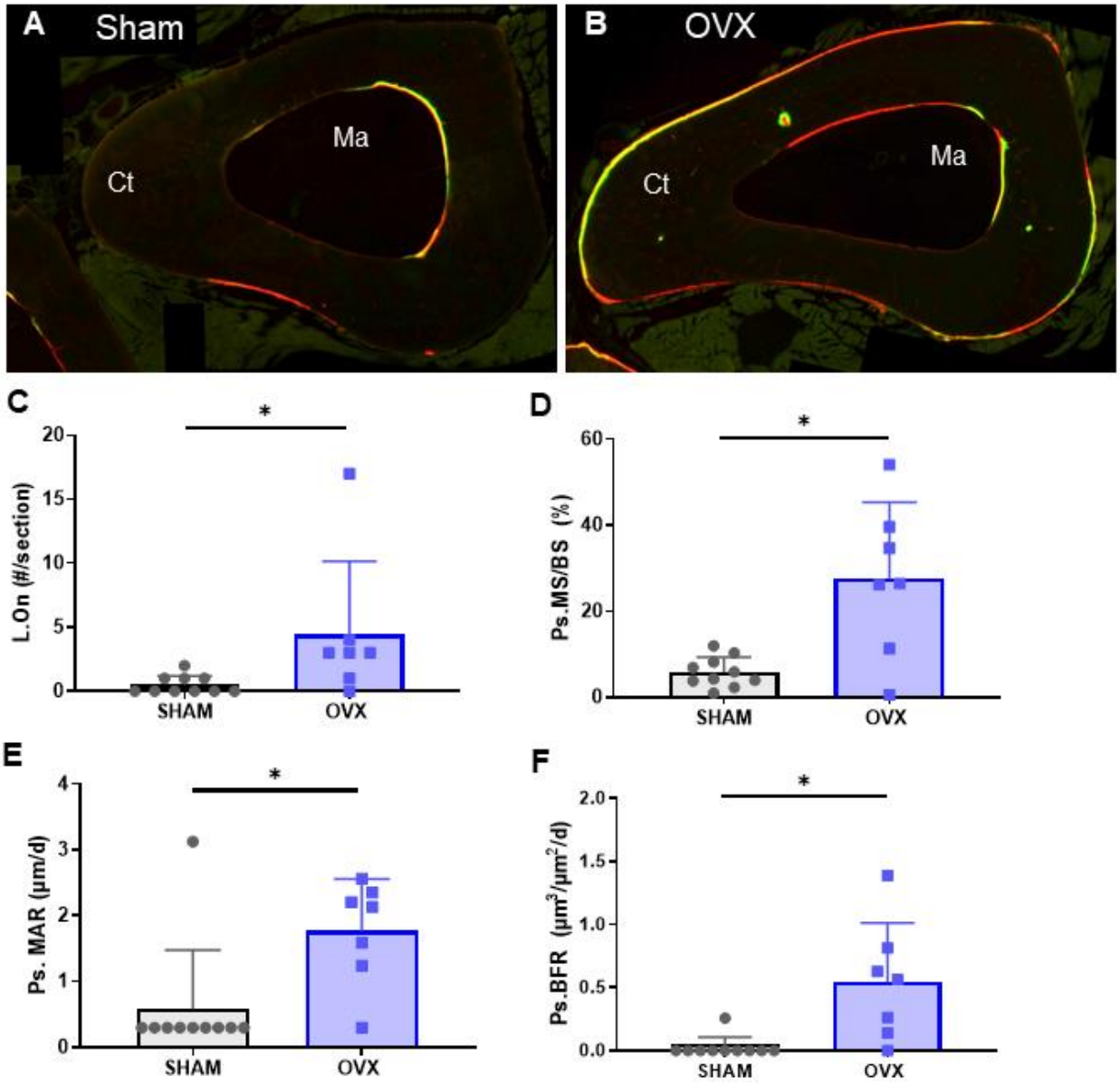

Figure 2.6: Experiment 1 - Dynamic histomorphometry of baseline remodeling in the rabbit ulna. Calcein and alizarin red fluorochromes were used to visualize locations of mineralization. An ulnar transverse section of **(A)** a sham operated animal and **(B)** an OVX animal show typical pattern of fluorochrome labels. **(C)** The amount of labeled osteons (L.On) increases for the OVX group. **(D)** The amount of periosteal (Ps.) mineralizing surface (MS/BS), mineral apposition rate (MAR) and bone formation rate (BFR) were also increased in the OVX group as compared to sham. **(E)** No difference was observed for endocortial parameters between groups (Table 2.1). Asterisk (*) denotes $p < 0.05$. n = 8-10/group.

2.4.4 Reliable creation of microdamage with sub-fracture fatigue loading was not achieved

The average number of loading cycles was 317 ± 434 cycles for low fatigue and 2,168 ± 2,542 cycles for moderate fatigue. En bloc fuchsin staining was used to visualize microdamage following no loading, low, or moderate fatigue (Figure 2.2 B). Fuchsin staining revealed microdamage was present in each group (Figure 2.7 A). However, no increase in diffuse damage (Figure 2.7 B) or linear microcracks (Figure 2.7 C) was observed with either low or moderate fatigue loading compared to control. Furthermore, stress fractures developed in two of the twelve loaded limbs, one each in the low and moderate fatigue group (Figure 2.8).

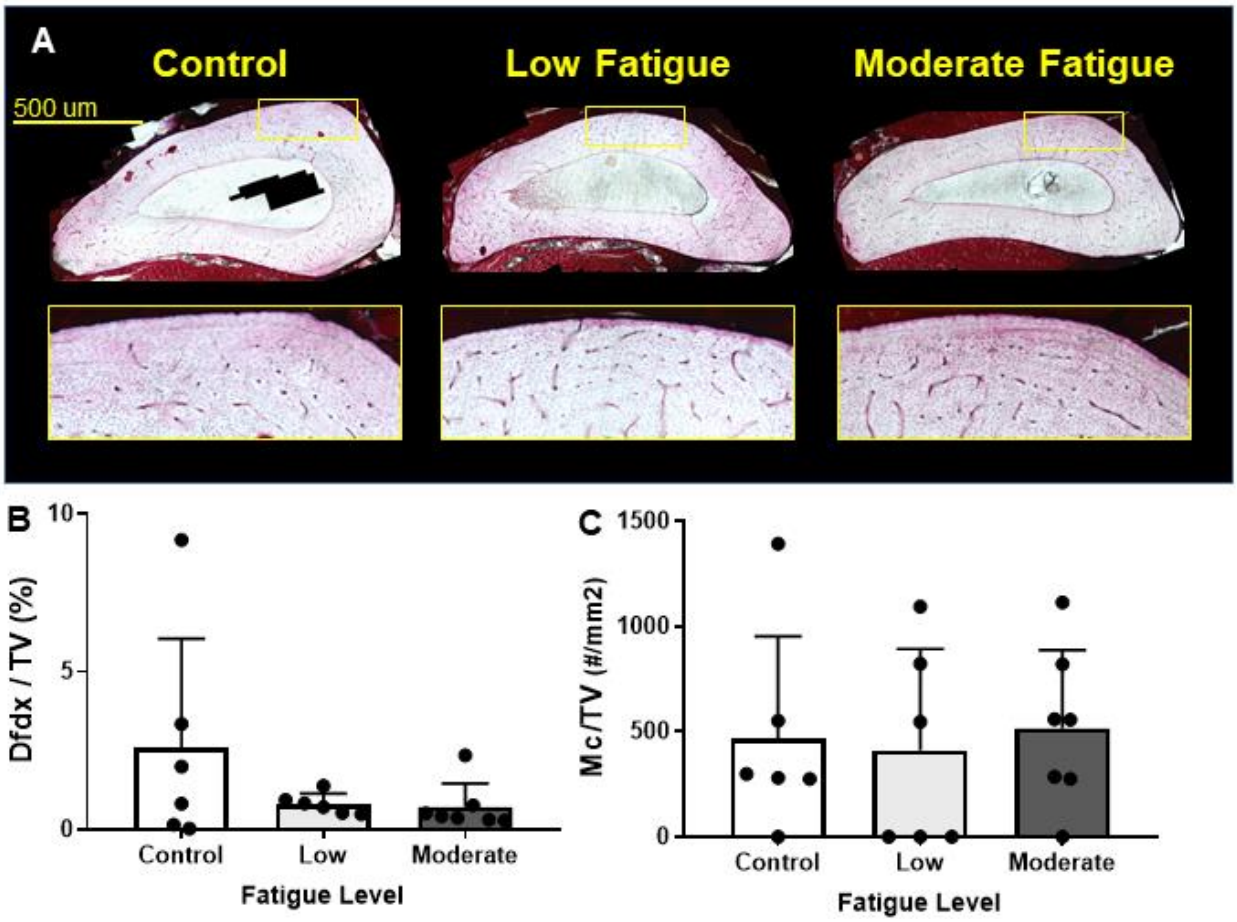

Figure 2.7: Experiment 2 - Analysis of microdamage after sub-fracture fatigue loading. Rabbit forelimbs were loaded as part of Experiment 2 design (Figure 1B). **(A)** Representative images of each group following fuchsin staining with insert showing magnified view of peak compressive region of the ulnar cortex. **(B)** Diffuse damage normalized to total volume (Dfdx/TV) and **(C)** linear microcracks normalized to total volume (Mc/TV) were not different between groups. n = 6-7/group.

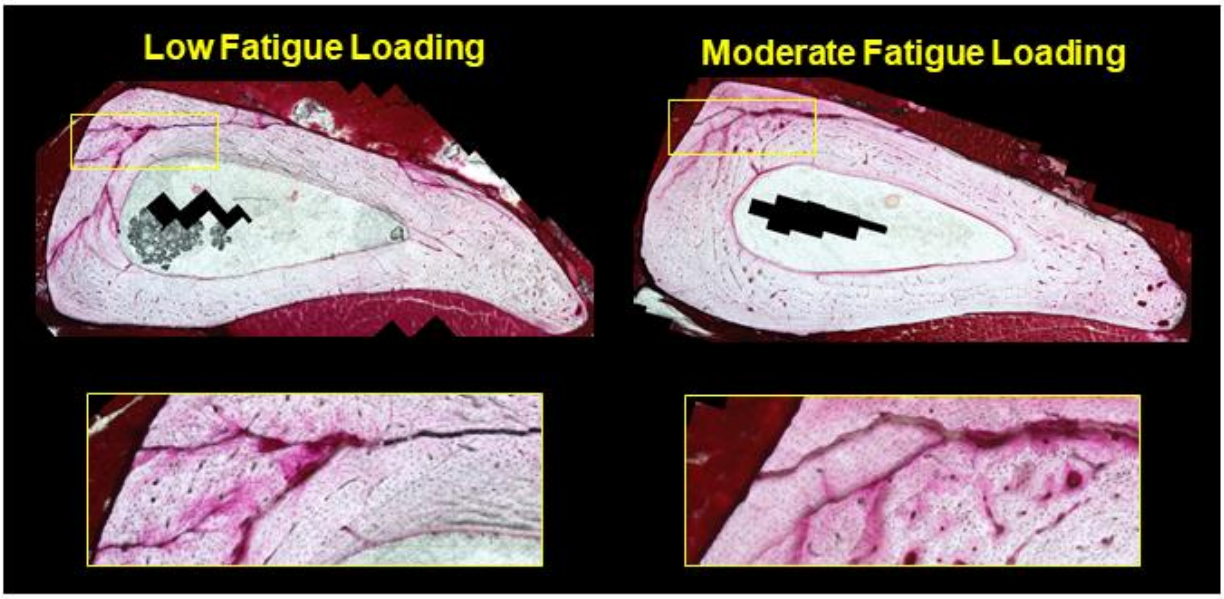

Figure 2.8: Experiment 2 - Macrocrack formation following low and moderate fatigue. Two stress fractures developed in ulna during fatigue loading. A stress fracture was observed by fuchsin staining in each of the low and moderate fatigue groups. The goal of this fatigue regime was to stop prior to macrodamage formation, which was not achieved in these two specimens.

2.4.5 Fatigue loading resulted in increased intracortical remodeling and periosteal bone formation

The average number of cycles for the survival fatigue loading was 1,509 ± 1,364 cycles. Following survival fatigue loading, an increased amount of fluorochrome labeling can be observed at 3 weeks and 6 weeks after loading when compared to non-loaded limbs (Figure 2.9 A). Repeated measures 2-way ANOVA showed a significant fatigue loading effect on intracortical remodeling ($p = 0.036$), periosteal mineralizing surface ($p = 0.031$), mineral apposition rate ($p = 0.044$) and bone formation rate ($p = 0.014$), and a significant time effect on periosteal bone formation rate ($p = 0.042$) (Figure 2.9 B-E). Multiple comparisons were then used to test significance between individual groups. Fatigue loading did not significantly increase intracortical remodeling in the first 3 weeks, but in the 6 week group there was an increase in labeled osteons (Figure 2.9 B). Fatigue loading also initiated a robust formation of periosteal lamellar bone as shown by increases in mineralizing surface (Figure 2.9 C), mineral apposition rate (Figure 2.9 D), and bone formation rate (Figure 2.9 E). The increased bone formation was strongest in the 3-week group but persisted in the 6-week group. Analysis of H&E stained histology did not reveal any basic multicellular units or areas of matrix remodeling within the cortical bone of loaded ulna (Figure 2.10).

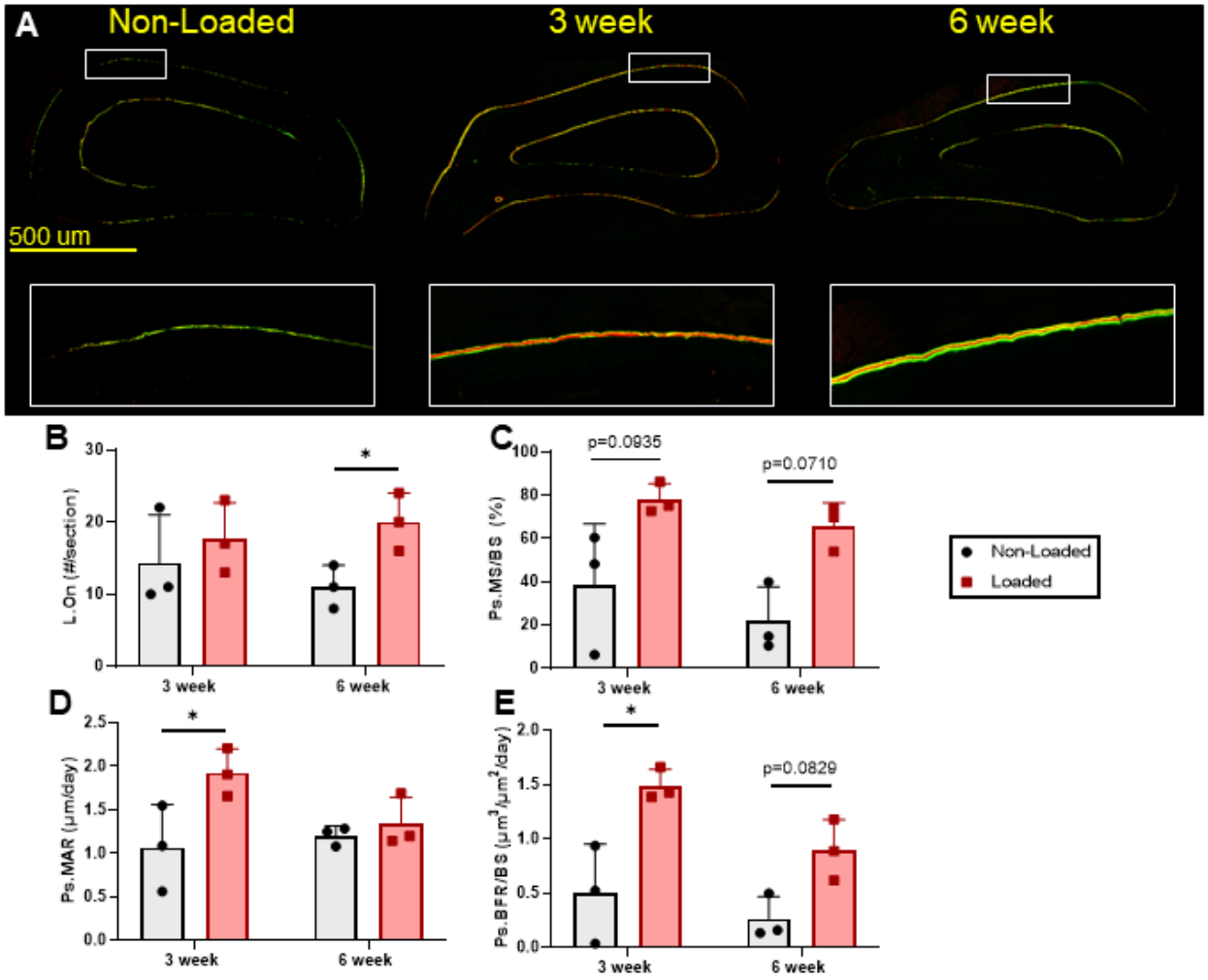

Figure 2.9: Experiment 3 - Response to survival sub-fracture fatigue loading. Rabbit forelimbs were loaded as part of Experiment 3 (Figure 1C). **(A)** Representative images of calcein and alizarin staining in ulna cross section for non-loaded, 3 week, and 6 week groups with insert showing magnified view of periosteum near the site of peak strain. **(B)** Labeled osteons (L.On) were significantly increased 6 weeks following loading. **(C)** Periosteal mineralizing surface (Ps.MS/BS) had non-significant increases at both 3 weeks and 6 weeks. **(D)** Periosteal mineral apposition rate (Ps.MAR) was significantly higher in the 3 week group, but not the 6 week group. **(E)** Periosteal bone formation rate (Ps.BRF/BS) was significantly higher in the 3 week group and trending higher in the 6 week group. Asterisk (*) denotes $p < 0.05$. n = 3/group.

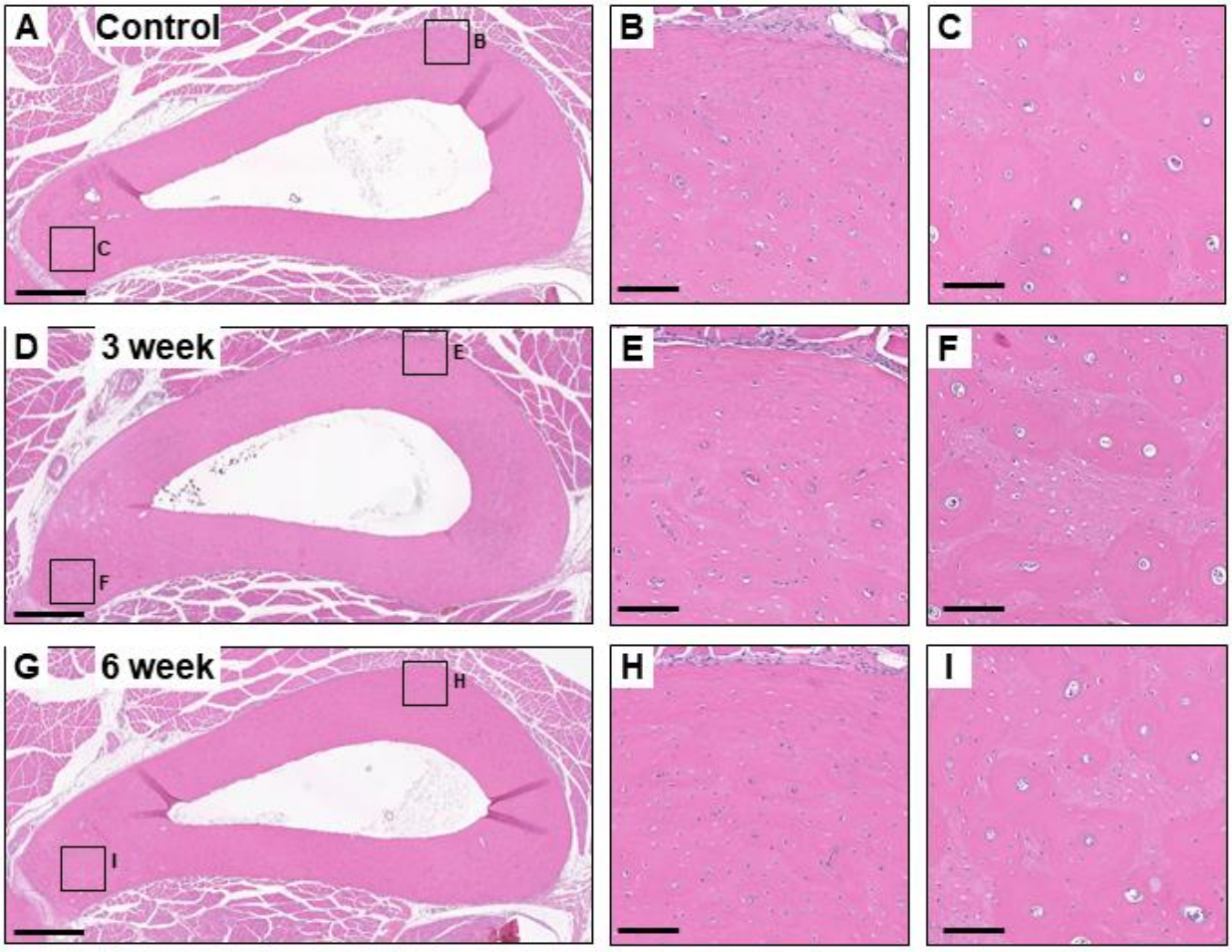

Figure 2.10: Experiment 3 - Histology of survival fatigue loaded ulna. Histology of ulna from survival loading rabbits were stained with hematoxylin and eosin. A full cross section of a non-loaded control ulna is shown (A), and regions of peak mechanical strain (B) and large amounts of osteons (C) are shown at higher magnification. Similar images are shown for the 3 week group (D-F) and the 6 week group (G-I). No evidence of increased intracortical remodeling is seen in the loaded limbs. Furthermore, the areas we expected to be most impacted by loading (B, E, & H) did not feature many osteons, while regions of the ulna not expected to be targeted by this loading model featured many osteons (C, F, & I). Scale bars were 500 μm in A, D, & G, and 100 μm in B,C, E, F, H, & I. n = 3/group.

2.5 Discussion

Herein, the rabbit forelimb fatigue model was modified to create sub-fracture damage in osteoporotic rabbits. The goals of this work were to adapt the model for use in OVX rabbits, to define loading parameters to achieve consistent microdamage creation, and to visualize an intracortical repair process following fatigue.

OVX has been used to induce osteoporosis in rabbits in several studies, and is associated with reduced BMD in the femur and lumbar spine [66–68]. However, the impact of OVX on the ulna, the bone of interest in this fatigue model, has not been reported. MicroCT showed no difference in the cortical bone parameters of the ulna (Figure 2.5). Similarly, we did not find significant differences in cancellous parameters between OVX and sham groups. The trends we observe are consistent with previous reports of the rabbit OVX model. Pennypacker et al. [66] reported a 9.8 % to 12.8% reduction in BMD of the lumbar spine following OVX, whereas we observe a non-significant difference of 12% in the cancellous compartment of the ulna. The same study reported that after OVX, cortical bone parameters of the femur diaphysis such as TMD and cortical area remained unchanged, consistent with our data of the ulna diaphysis. Thus, the changes we observed in the microCT data of OVX rabbits are marginal, but are comparable to previous reports. Post-hoc power analysis reveals that our analysis was underpowered to detect small effects, and that sample sizes would need to be more than doubled to n = 26 to adequately detect differences of 12%.

We used dynamic histomorphometry to observe baseline remodeling in OVX ulna (Figure 2.6). Compared to the sham group, OVX ulnas had increased levels of osteonal remodeling and periosteal labeling, both of which are established features of OVX in non-rodent models [66,73].

This result was consistent with Pennypacker et al. [66], who reported intracortical remodeling increasing from 0 to 4.5 labeled osteons per section in rabbit OVX femur, while our data show an increase from 0.5 to 4.4 labeled osteons per section in OVX ulna . Furthermore, Pennypacker and colleagues reported a 5.1 fold increase in periosteal mineralizing surface in OVX femur, which corresponds to our 4.7 fold increase in OVX ulna. We conclude that OVX successfully induced an osteoporotic-like state within the skeleton of these rabbits, albeit with limited effects on bone mass.

We achieved the goal of adapting the forelimb fatigue model for use with OVX rabbits, mainly because OVX had little effect on loading behavior. Comparison of the biomechanics of OVX rabbits to sham-operated animals shows similar behavior, which is consistent with microCT revealing no difference between OVX and sham cortical bone. Parameters such as ultimate force and fatigue displacement to fracture showed equal variability in sham and OVX, allowing for the selection of a loading force and stopping displacement parameters for sub-failure loading that were applied to all OVX animals used in subsequent experiments.

We sought to use sub-fracture fatigue loading to induce microdamage accumulation in the cortical bone of the ulna. To do this, stopping displacements were selected to target enough fatigue for microdamage creation, but stop short of macrocrack initiation (Figure 2.2 B) [70]. However, no differences in microdamage burden were identified by fuchsin staining (Figure 6). This was in contrast to reports that have used similar loading regimes to successfully induce microdamage accumulation in rat ulna [59,60,69]. Furthermore, two fatigue loaded limbs developed inadvertent macrocracks (Figure 2.8). This represents a challenge of targeting sub-fracture fatigue in rabbit forelimbs, which display large variability in the displacement to event 1

(Figure 2.4 B). Thus, our second goal of creating consistent microdamage was not achieved with these loading parameters.

Survival loading was used to visualize the repair response of OVX rabbits to sub-fracture fatigue. We observed an increase in intracortical labeling at 6 weeks, but not at 3 weeks (Figure 2.9 B). This suggests that the fatigue regime generated sufficient stimulus to induce an intracortical remodeling response, even in the absence of observable increases in microdamage burden (Figure 2.7). Despite the presence of intracortical labeling in dynamic histomorphometry, we did not observe signs of remodeling in H&E stained histology sections (Figure 2.10). Therefore, our third goal of observing an intracortical repair response to loading was only partially accomplished.

Periosteal bone formation was increased at both 3 and 6 weeks post-fatigue. This indicates induction of a remarkably persistent and robust lamellar loading response from a single bout of loading, and could be an interesting avenue of future study. Therefore, beyond its usefulness in sub-fracture fatigue, this model may be suitable for the study of loading-induced bone formation similar to the approach developed by Baumann and colleagues [74].

Several caveats for this work should be noted. Firstly, the non-survival sub-fracture fatigue characterization experiment (#2) and the survival experiment (#3) were performed concurrently. This hampered our ability to completely explore the range of fatigue levels before moving into survival experiments, and thus we did not obtain the increased microdamage burden we anticipated. Any future studies would need to identify a fatigue protocol which can more reliably generate microdamage. In our experience with cyclic loading of the rabbit forelimb, there is a very narrow window between non-damaging loading that stimulates lamellar bone formation,

and damaging loading that creates macrodamage/stress fracture. Secondly, it should be noted that these experiments, especially the survival loading, have limited sample size due the expense and time of working with rabbits. Finally, our goal was to create a model of fatigue loading in osteonal bone. But we observed that the areas of the rabbit ulna most affected by axial compression do not contain many osteons (Figure 2.10) [70].

2.6 Conclusions

We set out to modify the rabbit forelimb stress fracture model to produce sub-fracture microdamage accumulation and stimulate intracortical repair in osteoporotic and osteonal bone. We succeeded in adapting the use of this model to OVX animals and were also able to observe increased intracortical remodeling following loading. However, we were ultimately unsuccessful in producing reliable levels of sub-fracture microdamage, and thus the utility of this model to study interactions between microdamage accrual and repair is not yet established. In our experience with cyclic loading of the rabbit forelimb, there is a very narrow window between non-damaging loading that stimulates lamellar bone formation, and damaging loading that creates macrodamage/stress fracture.

Chapter 3: Transcriptional Profiling of Intramembranous and Endochondral Ossification after Fracture in Mice

3.1 Abstract:

Bone fracture repair represents an important clinical challenge with nearly 1 million non-union fractures occurring annually in the U.S. Gene expression differs between non-union and healthy repair, suggesting there is a pattern of gene expression that is indicative of optimal repair. Despite this, the gene expression profile of fracture repair remains incompletely understood. In this work, we used RNA-seq of two well-established murine fracture models to describe gene expression of intramembranous and endochondral bone formation. We used top differentially expressed genes, enriched gene ontology terms and pathways, callus cellular phenotyping, and histology to describe and contrast these bone formation processes across time. Intramembranous repair, as modeled by ulnar stress fracture, and endochondral repair, as modeled by femur full fracture, exhibited vastly different transcriptional profiles throughout repair. Stress fracture healing had enriched differentially expressed genes associated with bone repair and osteoblasts, highlighting the strong osteogenic repair process of this model. Interestingly, the PI3K-Akt signaling pathway was one of only a few pathways uniquely enriched in stress fracture repair. Full fracture repair involved a higher level of inflammatory and immune cell related genes than did stress fracture repair. Full fracture repair also differed from stress fracture in a robust downregulation of ion channel genes following injury, the role of

which in fracture repair is unclear. This study offers a broad description of gene expression in intramembranous and endochondral ossification across several time points throughout repair and suggests several potentially intriguing genes, pathways, and cells whose role in fracture repair requires further study.

3.2 Introduction

Skeletal fractures are an important clinical problem. About 16 million fractures occur annually in the U.S. – roughly one every two seconds [37]. Over the next decade, the national economic burden of fractures is estimated at $25 billion. Bones have a strong capacity for self-repair and, with proper intervention, most fractures will heal without major complications. Importantly though, about 5 to 10% of fracture patients will not heal adequately – suffering from either delayed- or non-union healing [38]. Delayed and non-union fractures are painful, costly, and require additional surgical interventions. Although many comorbidities are associated with nonunion, their molecular pathogenesis is unclear, thus representing an important target for research [15].

Bones fracture in several ways, depending on the mechanical cause of injury. Two broad categories, stress fractures and full fractures, are the focus of this work. Stress fractures are defined by a crack which is partially propagated, non-displaced, and unicortical [75,76]. Stress fractures are caused by repetitive overuse that leads to bone fatigue damage [77,78]. Alternatively, full fractures occur by complete propagation of one or more cracks across the bone cortices, resulting in a displaced fracture [79]. Full fractures are typically caused by a sudden

overload of the bone, as experienced in trauma. These different injuries trigger distinct repair cascades.

Stress fractures heal by intramembranous ossification, the direct formation of a bone callus without a cartilaginous intermediary [6]. Full fracture heals primarily through endochondral ossification, which features an intermediary cartilaginous callus [5] that is then replaced by bone, with some intramembranous ossification occurring at the stable margins of the fracture callus. The stability of the injury site and the displacement caused by the injury determine which bone formation mechanism occurs [7]. Intramembranous ossification is favored by stable injuries with little displacement and endochondral ossification is preferential when injuries are unstable and displaced. The distinct processes for intramembranous and endochondral bone formation are well documented – and transcriptomic analysis of each has individually been reported. Several studies have used microarray technology to assay gene expression in models of endochondral ossification in mouse [80–82], rats [83], and humans [84], and additional work has been performed using RNA-seq in mouse [85]. These works describe the complex transcriptional response following full fracture, which involves, inflammatory, angiogenic, chondrogenic, and osteogenic processes. There are few reports of gene expression in intramembranous ossification, with one report using microarray to study stress fracture healing in rat [29], which described strong expression of inflammatory, angiogenic, and osteogenic genes.

While these studies were illuminating, a more direct comparison of the gene expression profiles of intramembranous and endochondral ossification might provide additional insight. For example, while both processes involve inflammation, the relative scale of the inflammatory response is likely to be less after stress fracture than full fracture. Furthermore, sampling from

several time points following injury will provide information on how gene transcription changes throughout repair. A comparison of intramembranous and endochondral ossification spanning several time points across the repair window, using contemporary RNA-seq analysis, would address these knowledge gaps and shed light on similarities and differences between these two processes. Studies have shown that transcriptional differences exist between successful and non-union bone fracture repair [84] as well as young mice and slowly healing geriatric mice [80]. However, gene expression of poor healing is difficult to utilize if normal healing is incompletely understood. Therefore, a more comprehensive understanding of the transcription of endochondral and intramembranous ossification could better inform the treatment of delayed- and non-union fractures.

The goal of this work is to provide a detailed description of the temporal transcriptional response occurring in the fracture repair processes of intramembranous and endochondral ossification. We used two well-established murine fracture models and RNA sequencing to assay gene expression at five time points following stress fracture and full fracture. We hypothesized that endochondral repair would feature a greater number of differentially expressed genes than intramembranous repair, and that many of the genes unique to full fracture would be related to inflammation and chondrogenesis. Furthermore, we hypothesized that this analysis would reveal novel transcriptional differences between these two healing modalities.

3.3 Materials and Methods

3.3.1 Mice

Within an IACUC approved protocol, a total of 97 female C57BL/6J wild-type mice (Jackson Labs) were obtained at 9 weeks old and were aged to 12 weeks old for experimental use. We chose a single sex to limit the scope of the study, and selected females because women have higher rates of fracture [86,87]. Mice were kept on a 12:12 light/dark cycle and were fed chow ad libitum. A group of 47 mice were subjected to unilateral ulnar stress fracture and were randomly assigned to post-fracture time points of 4 hours, 1, 3, 5, or 7 days for either RNA extraction (N = 25) or histological processing (N = 22) (Figure 3.1 A). Additionally, a set of 50 mice were subjected to unilateral full femur fracture and were randomly assigned to post-fracture time points of 4 hours, 1, 3, 7, or 14 days for either RNA extraction (N = 35) or histology processing (N = 15) (Figure 3.1 A). We selected time points based on historical data to survey the various important phases of the early fracture repair response (i.e. inflammation, angiogenesis, chondrogenesis, and early osteogenesis). Differences in the later time points reflect the relatively longer time to peak osteogenesis in full versus stress fracture repair. All animals were healthy at time of injury and body weight was consistent between groups (mean body weight = 20.8 ± 1.3 g). Mice were euthanized by CO_2 asphyxia at the assigned post-injury time point.

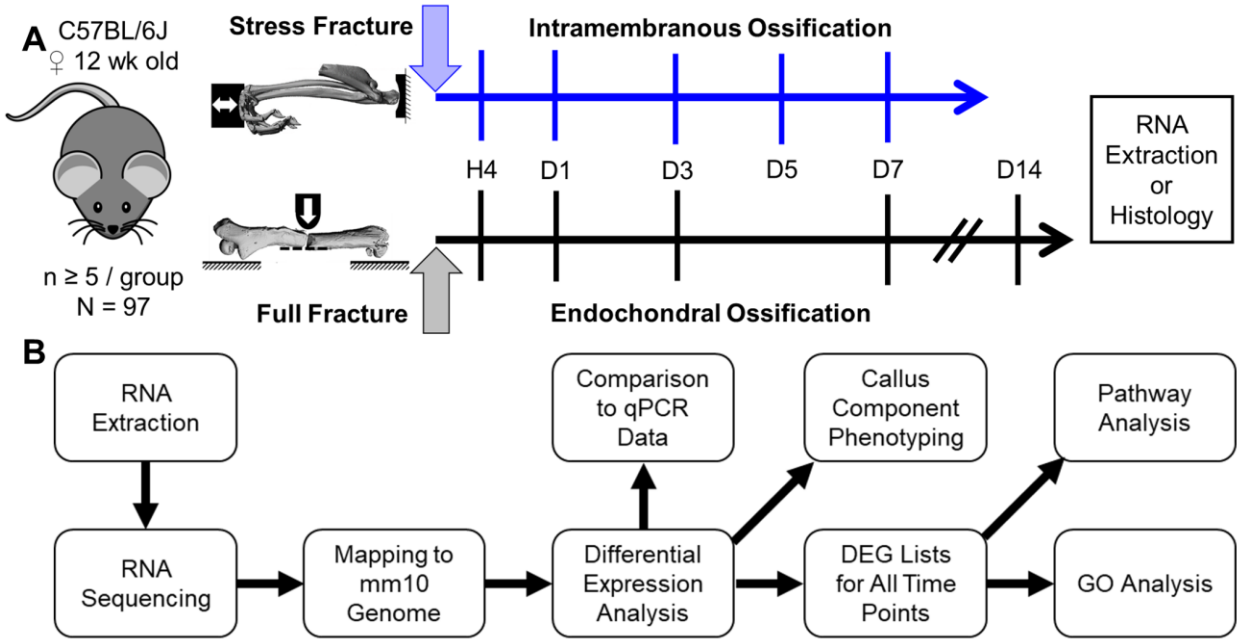

Figure 3.1: Experimental overview of fracture models, time points, and RNA-seq pipeline. (A) 97 female C57BL/6J mice were injured with stress or full fracture, sacrificed at 4 hours, 1, 3, 5, 7, or 14 days post-injury, and processed for RNA-seq or histology. **(B)** RNA-seq analysis began with RNA extraction from pulverized bone tissue. RNA was sequenced and reads were mapped to mm10 genome. Differential expression analysis was performed to create lists of differentially expressed genes (DEGs) for each time point. Comparison to previously generated qPCR data of stress and full fracture callus was used to validate RNA-seq data. Callus component analysis using transcriptional profiling of callus cells was performed at each time point. Pathway analysis and GO annotation were performed on the DEG lists of each time point.

3.3.2 Stress Fracture

We used ulnar stress fractures to study intramembranous ossification. The murine forelimb fatigue model used to create stress fractures was described in detail in previous reports [88,89]. Briefly, mice were anesthetized with 1-3% isoflurane and the right forelimb was positioned between two fixtures on a material testing machine (Instron Dynamite). Calibration mice were loaded with a monotonic displacement ramp to determine ultimate force of the forelimb and with cyclic compression to determine fracture displacement. Experimental mice

were loaded using force-controlled cyclic compression to a peak of 3.0 N (75% of mean ultimate force, 2 Hz) applied to the forelimb until an increase in total displacement of 0.5 mm (50% of mean fracture displacement) was achieved. The average number of cycles applied was 5,383 (range: 105 – 18,627). Time zero for the stress fracture was considered to be the time of the final loading cycle, as the crack growth mostly occurs in the last few cycles of loading. The left ulna served as a non-injured contralateral control. Following loading, the mouse was administered buprenorphine (0.1 mg/kg, s.c.) for analgesia and returned to the cage with unrestricted activity until time of sacrifice. Mice returned to subjectively normal activity levels within minutes of being returned to their cage.

3.3.3 Full Fracture

We used femur full fractures to study endochondral ossification. The femur fracture procedure was described in detail in previous reports [44]. In brief, mice were anesthetized with 1-3% isoflurane, and slow release buprenorphine (1 mg/kg, s.c.) was administered for pain management. The right femur was exposed through a small incision and notched with a scalpel to pre-dispose the mid-diaphysis to fracture. The right hind limb was then secured in a three-point bending fixture on a material testing machine (Instron Dynamite) and a monotonic displacement ramp (30 mm/s) was applied to produce a transverse fracture in the mid-diaphysis of the femur. A 24G pin was inserted into the intramedullary space to provide mechanical stability and the incision was closed. Fracture location and pin placement were confirmed by X-ray radiography (Faxitron UltraFocus). Mice were then returned to unrestricted cage activity and reached relatively normal activity levels within a few hours of the procedure. Generation of

fractures had good reproducibility with consistent tissue damage, actuator displacement, stability of the fracture, and lack of comminution. The left femur served as a non-fractured contralateral control. Radiographs were again taken at time of sacrifice to reconfirm intramedullary pin placement. Mice were excluded from analysis if fracture occurred outside the mid-diaphysis (n = 5) or if the stabilization pin had slipped from the intramedullary space by time of sacrifice (n = 1).

3.3.4 RNA extraction and sequencing

For stress fracture, a 5 mm section of the ulna was removed surrounding the injury site. Soft tissue was removed, the sample was flash frozen in liquid nitrogen, and stored at -80 °C until RNA extraction. The left ulna was similarly processed to serve as a control. For full fracture, a 7 mm section of the femur was removed surrounding the injury site. Soft tissue was removed and bone marrow was spun out using a centrifuge. The sample was flash frozen in liquid nitrogen and stored at -80 °C until RNA extraction. The left femur was similarly processed to serve as a control.

Frozen bone samples were pulverized (Braun Mikrodismembrator), dissolved into TRIzol (Invitrogen), and stored at -80 °C. Later, the TRIzol-sample solution was thawed and processed using an RNA clean-up and concentration kit (Norgen Biotek) (Figure 1B). RNA concentration was measured (Thermo Scientific Nanodrop ONE) and quality was evaluated (Agilent Technologies Bioanalyzer 2100). Only samples with RINs > 6.5, representing acceptable quality, were used in sequencing; samples not meeting this criterion were excluded (n = 4).

A total of 70 samples were subjected to RNA-seq (Figure 3.1 B). For each fracture type, there were 25 fracture samples (n = 5/time point) and 10 control samples (n = 2/time point). Total RNA was depleted of rRNA (Illumina, Ribo-Zero rRNA Removal Kit) and RNA-seq (Illumina HiSeq 3000) was performed at 1x50 bp on 1 μg of RNA by the Washington University Genome Technology Access Center. The RNA-seq reads were aligned to the mm10 mouse genome (STAR version 2.4.2a). Gene counts were derived from the number of uniquely aligned unambiguous reads (Subread:featureCount, version 1.4.6) and annotated (GENCODE v9). Only non-redundant uniquely aligned reads were used to estimate the expression level of genes. All gene-level transcript counts were then normalized for library size (R/Bioconductor DEseq2). Lowly expressed genes (CPM<1) in all the samples at any time points were filtered out, and resulted in 17,240 genes for down-stream analysis. To check for outlier samples a correlation analysis was performed (cutoff of $r > 0.85$). In stress fracture, three samples (one each from control, day 1, and day 7) were flagged as outliers and removed from further analysis. In full fracture, all samples passed this inspection. Differential expression analysis was performed separately for each injury mode and each time point as a comparison of injured samples vs. pooled control samples, with a threshold for differentially expressed genes (DEGs) set as fold-change (FC, Injured/Control) > 2 and Benjamini-Hochberg adjusted p-value < 0.05. Additional characterization was performed by a principle component analysis on stress fracture and full fracture samples separately. For each sample, the reads per kilobase of transcript per million mapped reads (RPKM) values for all 17,240 genes in the data set were used as inputs.

3.3.5 Validation of RNA-Seq data

In order to validate RNA-seq gene expression, we made comparisons to qPCR data previously generated in our lab using similar fracture models on control mice of similar age, size, and background. Fold change (FC) values for full fracture at days 7 and 14 post-injury, and stress fracture at days 1, 3, and 7 post-injury were correlated to FC values previously reported for 49 transcripts resulting in 94 comparisons as some transcripts were in multiple time points (Table 3.1) [44,88,89]. Additionally, we performed qPCR for select genes on remaining RNA from full fracture samples. Collagen Type 1a1 (*Col1a1*), Aggrecan (*Acan*), and Potassium Voltage-Gated Channel Subfamily J Member 5 (*Kcnj5*) were chosen in order to sample genes from various processes with differing expression profiles. cDNA was produced (Biorad iScript) from 500 ng of RNA for all full fracture samples from days 1, 3, 7 and 14 and corresponding contralateral femurs. qRT-PCR was performed (Applied Biosystems StepOnePlus) using primers (IDT PrimeTime) for *Col1a1* (Mm.PT.58.7562513), *Acan* (Mm.PT.58.23585796), and *Kcnj5* (Mm.PT.58.6016350) and reference genes TATA Binding Protein (*Tbp,* Mm.PT.58.42394711) and Importin 8 (*Ipo8,* Mm.PT.39a.22214844). Expression was normalized to reference genes and fold changes were determined by ΔΔCT method comparing to contralateral limb.

Table 3.1: Genes used in comparison of qPCR data to RNAseq data.

Gene ID	Injury	Time point	Source
Gli1	Full Fracture	D7, D14	Liu et al.
Ptch1	Full Fracture	D7, D14	Liu et al.
Ihh	Full Fracture	D7, D14	Liu et al.
Dhh	Full Fracture	D7, D14	Liu et al.
Ibsp	Full Fracture	D7, D14	Liu et al.
Bglap	Full Fracture	D7, D14	Liu et al.
Sp7	Full Fracture	D7, D14	Liu et al.
Col1a1	Full Fracture	D7, D14	Liu et al.
Acan	Full Fracture	D7, D14	Liu et al.
Sox9	Full Fracture	D7, D14	Liu et al.
Col2a1	Full Fracture	D7, D14	Liu et al.
Fgf2	Full Fracture	D7, D14	Liu et al.
Tek	Full Fracture	D7, D14	Liu et al.
Vegfa	Full Fracture	D7, D14	Liu et al.
Hmox1	Full Fracture	D7, D14	Liu et al.
Nos2	Full Fracture	D7, D14	Liu et al.
Ang	Full Fracture	D7, D14	Liu et al.
Ang2	Full Fracture	D7, D14	Liu et al.
Tie1	Full Fracture	D7, D14	Liu et al.
Ptn	Full Fracture	D7, D14	Liu et al.
Acan	Full Fracture	D7	McBride et al.
Bmp2	Full Fracture	D7	McBride et al.
Bmp3	Full Fracture	D7	McBride et al.
Bmp4	Full Fracture	D7	McBride et al.
Bmp7	Full Fracture	D7	McBride et al.
Ibsp	Full Fracture	D7	McBride et al.
Chrd	Full Fracture	D7	McBride et al.
Col1a1	Full Fracture	D7	McBride et al.
Col2a1	Full Fracture	D7	McBride et al.
Grem1	Full Fracture	D7	McBride et al.
Nog	Full Fracture	D7	McBride et al.
Sp7	Full Fracture	D7	McBride et al.
Sox9	Full Fracture	D7	McBride et al.
Vegfa	Full Fracture	D7	McBride et al.
Bmp2	Stress Fracture	D1, D3, D7	Martinez et al.
Ibsp	Stress Fracture	D1, D3, D7	Martinez et al.
Sp7	Stress Fracture	D1, D3, D7	Martinez et al.
Vegfa	Stress Fracture	D1, D3, D7	Martinez et al.
Hif1a	Stress Fracture	D1, D3, D7	Martinez et al.
Col1a1	Stress Fracture	D1, D3, D7	Martinez et al.
Col2a1	Stress Fracture	D1, D3, D7	Martinez et al.
Fgfr1	Stress Fracture	D1, D3, D7	Martinez et al.
Fgfr2	Stress Fracture	D1, D3, D7	Martinez et al.
Fgfr3	Stress Fracture	D1, D3, D7	Martinez et al.
Fgf1	Stress Fracture	D1, D3, D7	Martinez et al.
Fgf2	Stress Fracture	D1, D3, D7	Martinez et al.
Fgf9	Stress Fracture	D1, D3, D7	Martinez et al.
Fgf16	Stress Fracture	D1, D3, D7	Martinez et al.
Fgf18	Stress Fracture	D1, D3, D7	Martinez et al.

3.3.6 Gene Ontology and Pathway Analyses

For gene ontology analysis, each of the ten DEG lists (2 injury types x 5 time points) was input into the Database for Annotation, Visualization and Integrated Discovery (DAVID) system as a gene list [90,91]. Annotations were limited to *Mus musculus*. Biological process gene ontology (GO) terms and enriched pathways from the Kyoto Encyclopedia of Genes and Genomes (KEGG) database were obtained for each list and filtered to remove non-significant terms (Bonferroni $p < 0.05$).

3.3.7 Callus Component Phenotyping

To identify various populations of cells in the callus following stress or full fracture, we followed an approach described by Angelova et al. in the immunophenotyping of tumor biopsies [92]. Briefly, they used RNA-seq of bulk tumor biopsies and compared the gene expression against curated lists comprised of genes specific to certain immune cell types. By comparing the gene expression of curated lists, a census of immune cells residing in the tumor can be inferred. In a similar manner, we used RNA-seq of fracture callus tissue, in combination with curated gene lists, to infer the cellular populations present at various stages of stress and full fracture repair. Gene lists were compiled from literature reviews for neutrophils, macrophages, monocytes, T cells, and B cells [92]; as well as osteoblasts [93,94], osteoclasts [95–99], endothelial cells [100,101], and chondrocytes [102–105] (Table 3.2) . We then examined the fold change of these genes across time following stress and full fracture as an estimate of the abundance of each cell type within the callus.

Table 3.2: Genes used in callus component phenotyping

Cell Type	Gene List	References
Neutrophil	*Abtb1, Ampd2, Camp, Fpr1, Fpr2, Maea, Prok2, Sec14l1, Slc25A37, Tnsfs14, Treml4, Xpo6*	Angelova et al.
Macrophage	*Aif1, Cd163, Cd300lb, Cnr1, Cnr2, Cpm, Csf3r, Eng, Igf1, Il34, L1cam, Lilra5, Lrp1, Ms4a7, Trem1, Treml1*	Angelova et al.
Monocyte	*Actr3, Anxa5, Arpc2, Atp6v1b2, Basp1, Cd300lf, Dazap2, Eif4a1, Eif4g2, Emp3, Gabarap, Hif1a, Litaf, Ncoa4, Olr1, Rab1a, Rhoa, Sat1, Sdcbp, Srgn, Tek, Tmbim6, Ube2d3*	Angelova et al.
T Cells	*Batf, Btla, Ccl11, Ccl3, Ccl5, Ccl7, Ccr1, Ccr3, Cd247, Cd28, Cd3d, Cd3e, Cd3g, Cd69, Cd8a, Cxcr4, Cxcr5, Cxcr6, Flt3, Fosl1, Grap2, Hrh2, Il10, Il12rb1, Il12rb2, Il18r1, Il18rap, Il1b, Il21r, Il27, Il2ra, Il6, Il7, Ilrf4, Irf8, Itgal, Itk, Jak2, Jak3, Lair1, Lat, Lax1, Lck, Lcp2, Ms4a4a, Nfatc1, Nfkb2, P2ry14, Pik3cd, Pou2f2, Prf1, Runx3, Spi1, Stat1, Stat4, Tnf, Ubash3b,*	Angelova et al.
B Cells	*Akna, Arhgap25, Cd180, Cd2, Cd276, Cd37, Cd38, Clec9a, Fam65b, Gimap4, Map4k1, Pax5, Traf3ip3*	Angelova et al.
Osteoblasts	*Sp7, Bglap, Col1a1, Col1a2, Alpl, Sparc, Ibsp, Dmp1, Maged1, Pard6g, Kdelr3, Rcn3, Col5a1, Fkbp10, Tmem119, Gja1*	Calabrese et al., Rodan & Noda
Osteoclasts	*Ocstamp, Ctsk, Calcr, Spi1, Tnfrsf11a, Csf1, Src, Mmp9, Oscar, Tnfsf11, Efna2, Tyrobp*	Barrow et al., Irie et al., Jiang et al., Yang et al., Zaidi et al.
Endothelial Cells	*Kdr, Cdh5, Erg, Tek, Pecam1, Acta2, Cspg4, Ptprc, Vegfa, Angpt2, Hif1a, Flt1*	Rivera et al., Sabbah et al.
Chondrocytes	*Col2a1, Col10a1, Comp, Eln, Acan, Fn1, Mgp, Sox9, Egr1, Hes1, Tgif1, Prg4, Ihh, Shox2*	Dehne et al., Xu et al., Yu et al., Lin et al.

3.3.8 Histology

Following sacrifice, injured limbs from stress fracture (n = 22) and full fracture (n = 15) were harvested and placed in 10% neutral buffered formalin for 24 hrs. Tissue was decalcified for 14 days using 14% EDTA, embedded in paraffin, and longitudinal cuts were made for histological observation and immunohistochemistry (IHC) processing. Histological sections of each time point were stained with hematoxylin and eosin (H&E) to show the progression of healing in each fracture type at each time point in the study (Figure 3.2).

Antibodies for Gr-1 (Bio-Rad MCA2387T, 1:500 dilution), F4/80 (Bio-Rad, MCA497RT 1:500 dilution), and CD45 (BD Pharmingen 550539, 1:500 dilution) were used with an ImmPRESS Reagent Anti-Rat IgG (VectaShield MP-7404) kit to stain for infiltration of neutrophils, macrophages, and leukocytes, respectively. An antibody for p-Akt T308 (Cell Signaling #2965) was used with a goat anti-rabbit/HRP secondary antibody (Dako P0448) in order to stain for activation of the PI3K-Akt signaling pathway. Sections were counterstained with hematoxylin (Modified Mayer's, Electron Microscopy Services). Following staining, slides were imaged using a Nanozoomer slide scanner (Hamamatsu) at 20X magnification.

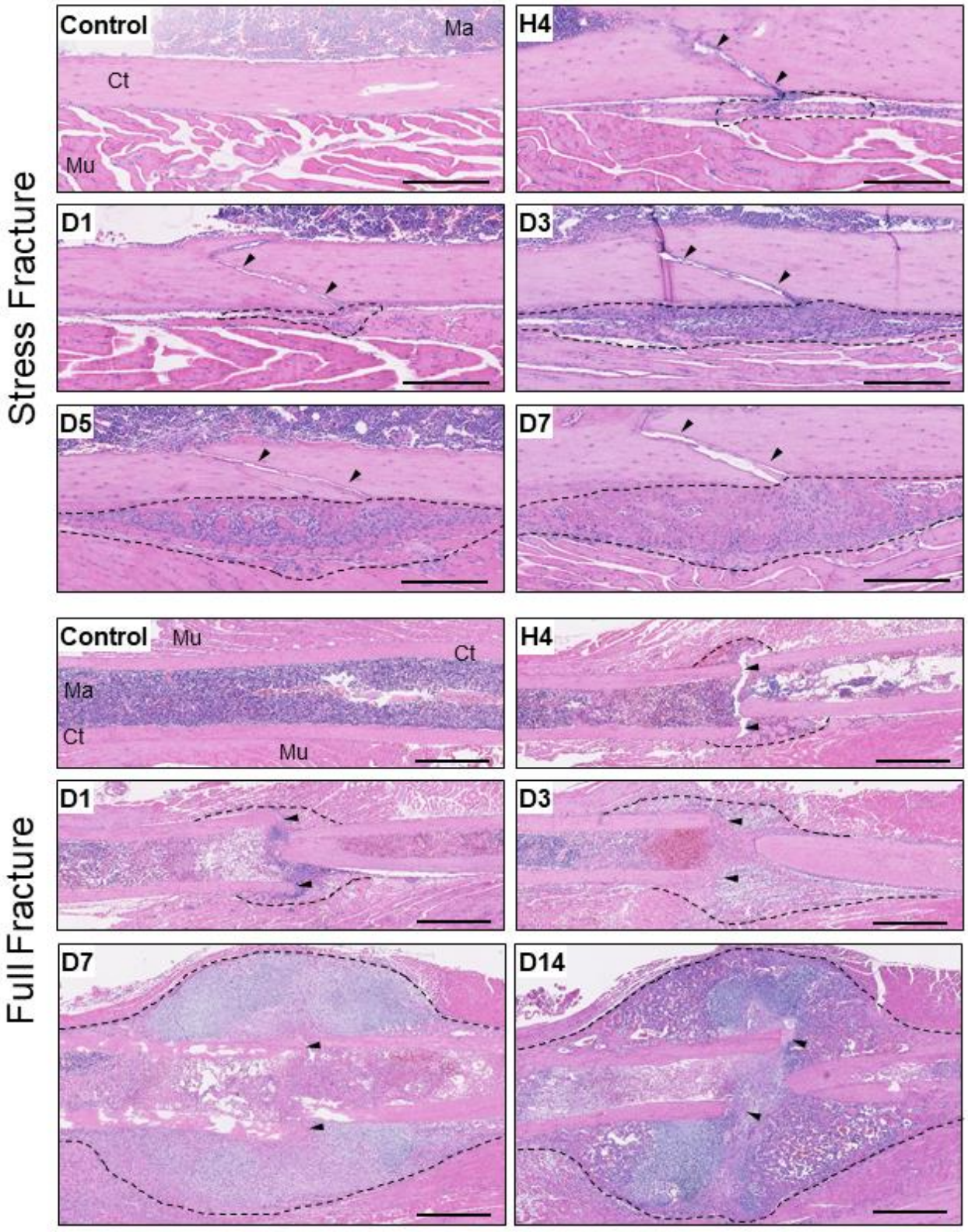

Figure 3.2: Progression of healing of stress fracture and full fracture over time. H&E staining of paraffin sections of stress fracture or full fracture callus. Scale bars represent 250 μm for stress fracture images and 1 mm for full fracture images. Ct = Cortical Bone, Ma = Marrow, Mu = Muscle, ▲ = stress fracture or full fracture line, dotted line = callus.

3.4 Results

3.4.1 RNA-seq Data Correlates to Previous Fracture Gene Expression Data

Plots of principle components 1, 2, and 3 for all samples in stress fracture (Figure 3.3 A) and full fracture (Figure 3.3 B) were compiled. Samples clustered by time point and adjacent time points were closest together on the plots. Additionally, gene expression values from RNA-seq and previously published qPCR data were strongly correlated ($r = 0.75$) and clustered around the identity line (Figure 3.3 C). Fold changes from qPCR performed on remaining RNA from full fracture samples also closely corresponded to those from the RNA-seq analysis (Figure 3.3 C). These data supported the accuracy of RNA-seq to describe post-fracture transcriptional changes, affirmed the integrity of these samples, and confirmed the validity of pooling controls and samples within time points.

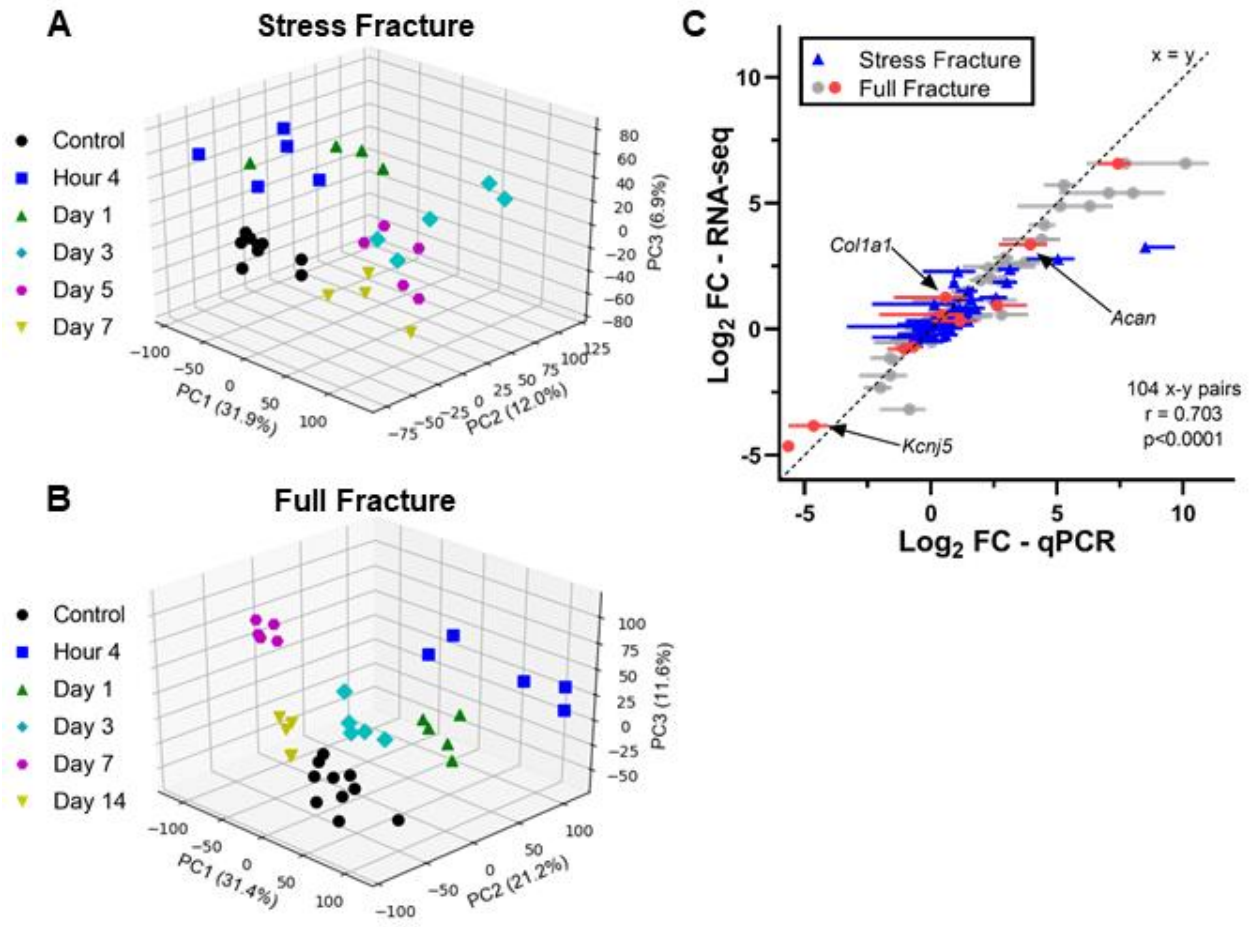

Figure 3.3: Validation of RNA-seq data. Principle component analysis (PCA) of all samples in stress fracture **(A)** and full fracture **(B)**. Samples within time points cluster together and time point clusters were grouped closely with adjacent time points. **(C)** Correlation of RNA-seq data with analogous qPCR data from previous published reports of stress fracture (blue triangle) and full fracture (grey circle) and concurrent qPCR of full fracture samples (red circle). Log2 fold change (injured vs. control) from RNA-seq was plotted versus log2FC from qPCR (+/- standard deviation). Data is plotted from multiple time points for each injury. A linear regression confirmed strong correlation between RNA-seq and qPCR data. Genes from published reports are detailed in Table 3.1. Select genes from concurrent qPCR are labeled with arrows.

3.4.2 Dramatic Transcription Changes during Fracture Repair

Overall, there were approximately 17,240 genes with high enough expression to be included in DEG analysis. Of these, 7,383 were differentially expressed genes (DEGs) in at least one time point and fracture type. Stress fracture repair had few early responding genes with only 87 DEGs at 4 hours and 124 DEGs at day 1 following injury (Figure 3.4 A). This number increased to 1,099 DEGs by day 3 and peaked with 1,434 DEGs at 5 days post-injury. From 5 to 7 days post injury, the number of DEGs declined. On the other hand, full fracture resulted in many early changes in gene expression, with over 2,000 DEGs at 4 hours post-injury (Figure 3.4 B). The number of DEGs remained high across all time points and peaked at 4,474 DEGs at 7 days post-injury. After full fracture, more genes were downregulated than upregulated across all time points. In contrast, more genes were upregulated at all stress fracture repair time points.

Gene expression varied greatly across time, with few genes differentially expressed across all time points. The largest DEG subsets were those unique to only one time point or those shared by consecutive time points – especially the later ones (Figures 3.4 C & D). For example, in stress fracture the largest DEG subset is the one shared between days 3, 5, and 7 post-fracture (571 DEGs). The numbers of DEGs shared between any two time points further highlights that the greatest number of shared DEGs occurs between adjacent time points (Figure 3.5).

Across all time points, 1,469 DEGs were shared between stress fracture and full fracture, while 5,497 DEGs were unique to full fracture, and 210 were unique to stress fracture repair (Figure 3.6 A). A similar trend was observed for each time point comparison, with the largest number of DEGs unique to full fracture, a smaller subset shared between the two injuries, and the fewest DEGs unique to stress fracture. Each subgroup was analyzed for enriched GO terms and pathways (Figure 3.6 B).

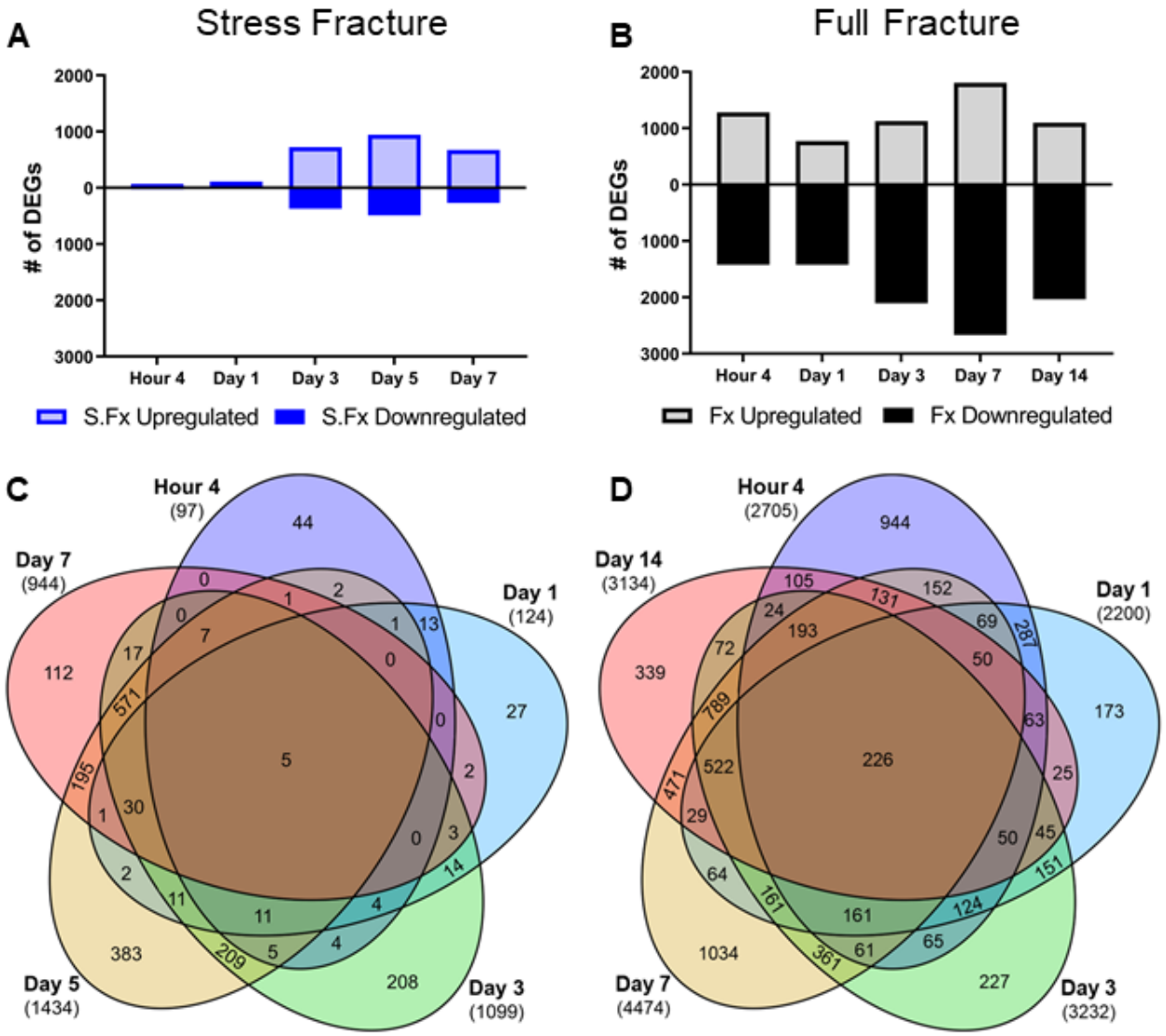

Figure 3.4: DEG trends across time. Total number of DEGs at each time point are shown for stress fracture **(A)** and full fracture **(B)**. Following stress fracture (S.Fx), few DEGs occurred early, but DEGs reached robust levels at later time points and peaked at day 5. Following full fracture (Fx), DEGs were immediately expressed at high levels that persisted through our experimental window, and peaked at day 7. Comparisons of the overlap of DEGs at each time point for stress fracture **(C)** and full fracture **(D)** are shown in 5-way Venn diagrams. Total number of DEGs at each time point are shown in parentheses. The largest lists were those unique to one time point or shared between adjacent time points.

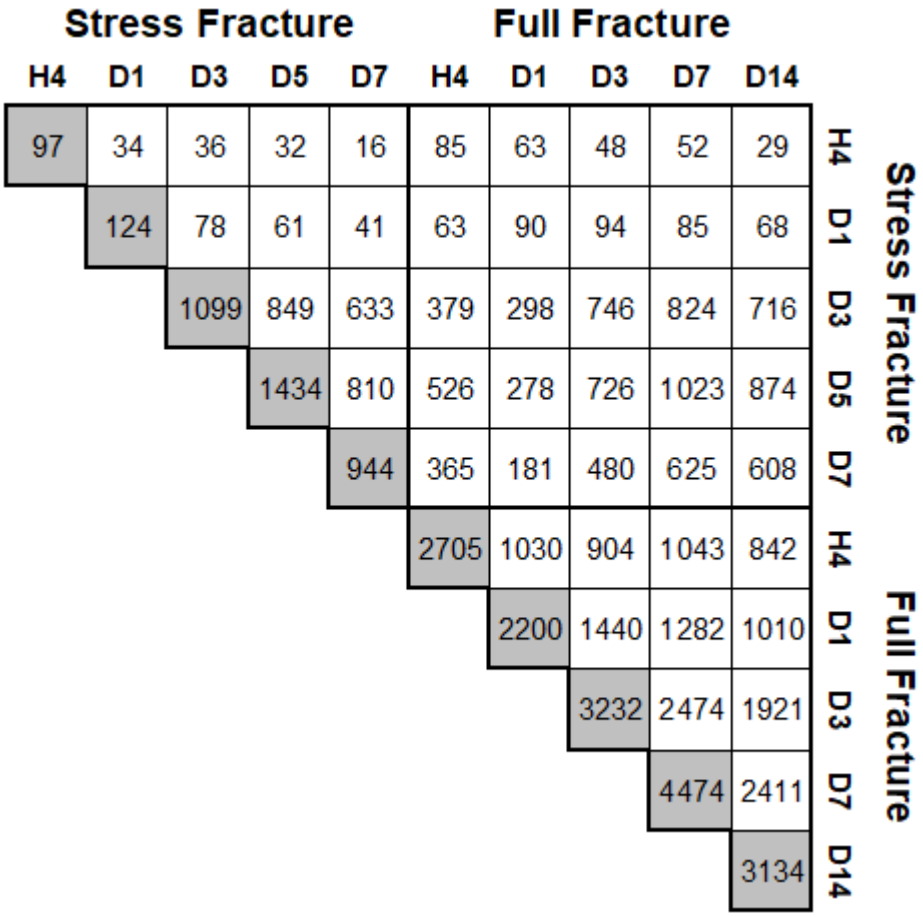

Figure 3.5: DEG overlap between time points. Number of differentially expressed genes (DEGs) shared between time points. Grey boxes show the total number of DEGs in each individual time point, while white boxes show number of shared DEGs between the two time points.

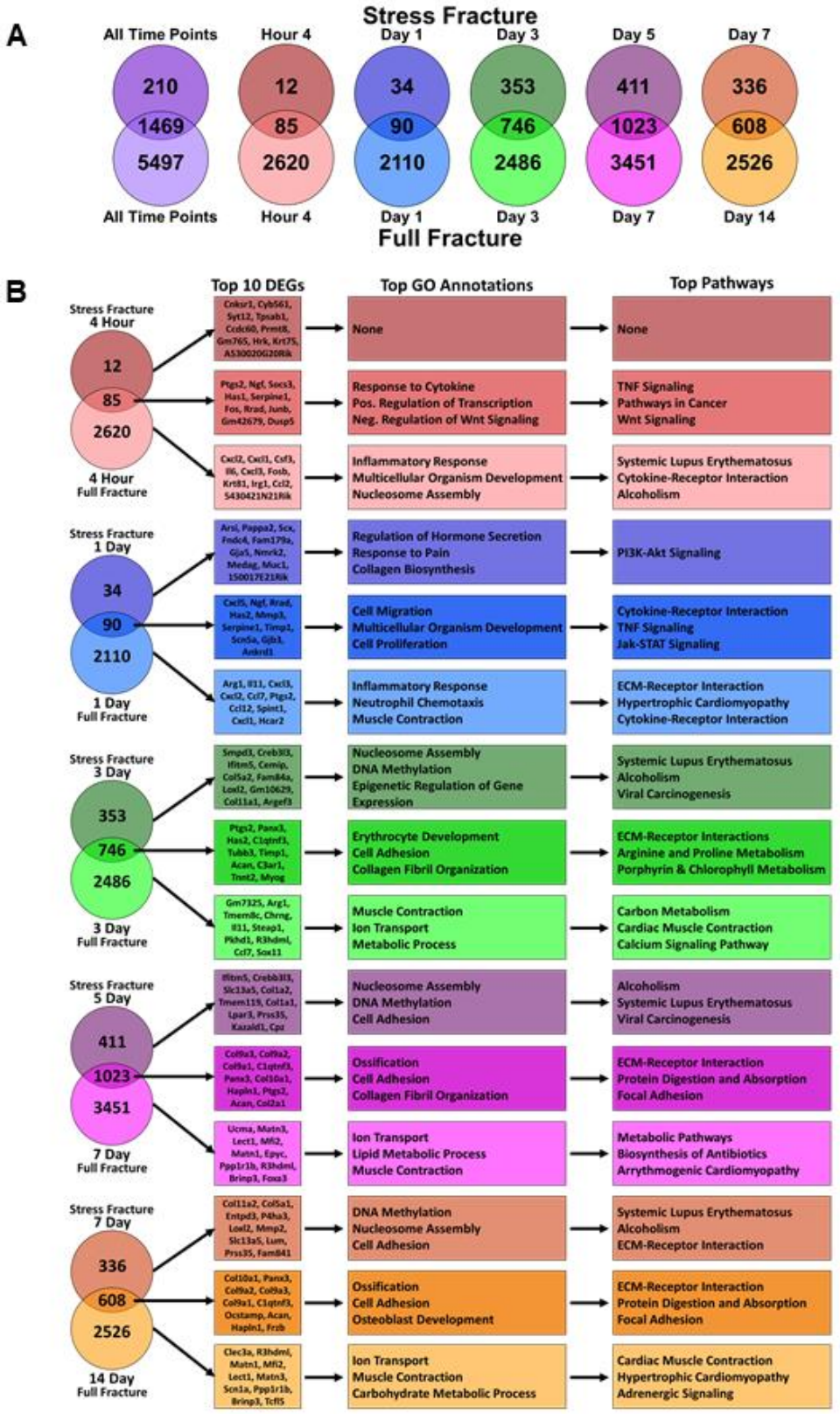

Figure 3.6: Comparison of DEGs between fracture types. Comparisons across injury type at various time points reveal lists of DEGs which are shared between the two injuries or unique to one repair process. **(A)** The number of genes shared between injuries at corresponding time points. **(B)** The top genes, GO terms, and pathways for each of these lists.

3.4.3 Stronger Expression Changes in Full Fracture Repair

The top ten up- and downregulated DEGs at every time point were compiled (Table 3.3). In stress fracture, genes involved in inflammation and matrix degradation were upregulated at early time points. Among these were Prostaglandin-Endoperoxide Synthase 2 (*Ptgs2*), Suppressor of Cytokine Signaling 3 (*Socs3*), and metalloproteinases *Mmp3, Adamts4,* and *Timp1*. Ras Related Glycolysis Inhibitor and Calcium Channel Regulator (*Rrad*) was among the top upregulated genes at H4 and D1 post-stress fracture. *Rrad* is involved in bone homeostasis and knockout of *Rrad* leads to osteopenia [106]. Pannexin 3 (*Panx3*) and C1q and TNF Related 3 (*C1qtnf3*) are the top most upregulated DEGs at days 3, 5, and 7 post-stress fracture. Both *Panx3* and *C1qtnf3* are expressed in osteoblasts [107]. *Panx3* is a putative Runx2 target [108] and is important in osteoblast differentiation and regulation of the Wnt/β-catenin pathway [109]. In the context of bone, *C1qtnf3* is less understood, but may also influence osteoblast differentiation [110,111]. The greatest FC values occurred at D5, which is also the time point with the largest number of DEGs. Interestingly, genes associated with chondrogenesis (*Col9a1/2/3, Col2a1, Acan*) are highly upregulated despite the relatively small amount of cartilage tissue in the stress fracture callus [112]. However, these may not necessarily be due to chondrocytes, as osteoblasts also express these transcripts[107]. Appearing among the early downregulated genes are Dickkopf WNT Signaling Pathway Inhibitor 1 (*Dkk1*) and Sclerostin (*Sost*) – both known inhibitors of bone formation [113,114].

In full fracture, inflammatory genes exhibited the largest fold changes at the early time points. Among these were the C-X-C Motif Chemokine Ligands 1, 2, 3 and 5 (*Cxcl1*, *Cxcl2*, *Cxcl3*, and *Cxcl5*), which are attractants of immune cells and endothelial cells [36,115,116], as

well as *IL-6*, *IL-11*, and *Ptgs2*, all important chemokines in bone repair [31,34,35,117,118]. Arginase 1 (*Arg1*), an essential metabolite in collagen synthesis and wound repair, was also highly upregulated at several time points [119]. Like stress fracture, the largest FC values occurred at the penultimate time point (day 7), when there was a large upregulation of chondrocyte related genes (*Col9a1/2/3, Col10a1, Matn1/2*); the peak fold changes in chondrocyte related genes were an order of magnitude greater in full fracture than stress fracture (e.g., *Col9a1*: FC = 440, D7 full fracture vs. FC = 35, D5 stress fracture). Among the most downregulated genes in full fracture repair are those related to myosin (*Myl2*, *Myl3*, *Myh7*, and *Mylk4*) and genes from the immunoglobin superfamily (*Ly6g6f*, *G6b*, and *Gp6*).

Table 3.3: Top up- and down-regulated DEGs for each injury and time point.

	Stress Fracture									
	Hour 4		Day 1		Day 3		Day 5		Day 7	
	Gene	FC	Gene	FC	Gene	FC	Gene	FC	Gene	FC
Up-regulated	Rrad	4.8	Timp1	6.7	C1qtnf3	24.8	Panx3	88.2	Panx3	24.2
	Ptgs2	4.7	Rrad	6.7	Panx3	20.7	C1qtnf3	75.0	C1qtnf3	20.9
	Socs3	4.7	Mmp3	5.2	Ptgs2	17.3	Col9a3	65.3	Car12	19.3
	Wnt1	4.2	Has2	5.1	Hapln4	13.3	Col9a2	62.8	Col10a1	14.0
	Ngf	4.1	Scn5a	4.9	Cthrc1	12.8	Col9a1	35.2	Col9a2	13.1
	Tnfrsf12a	3.6	Socs3	4.5	Tubb3	11.9	Hapln1	35.0	Col2a1	9.5
	Adamts4	3.6	Pdpn	4.4	Timp1	11.5	Ptgs2	34.7	Cthrc1	9.5
	Gm42679	3.5	Card14	4.4	Car12	11.4	Col2a1	34.3	Col9a3	9.4
	Has1	3.4	Myog	4.3	Acan	9.7	Car12	27.3	Myh8	8.9
	Serpine1	3.1	Adamts4	4.1	Fkbp11	8.7	Acan	24.0	Bcan	8.5
Down-regulated	Gng8	-2.5	Nell2	-2.4	Redrum	-3.8	Cd8b1	-5.2	Ighv9-3	-3.6
	Krt75	-2.4	A930018M24Rik	-2.3	Hist3h2ba	-3.7	Phyhip	-3.6	Phyhip	-3.3
	Dkk1	-2.4	Prss55	-2.3	F930017D23Rik	-3.7	Acmsd	-3.4	Hbb-bs	-3.2
	Dlx6os1	-2.4	Klhl33	-2.3	Inmt	-3.6	Gm42870	-3.4	Ms4a1	-3.2
	A530020G20Rik	-2.3	Ces1d	-2.2	A730036I17Rik	-3.6	Terc	-3.4	Fcmr	-3.1
	Gprasp2	-2.3	Sost	-2.2	Rhag	-3.6	Odf3l2	-3.4	Hbb-bt	-3.1
	Hrk	-2.3	Mylk4	-2.2	Klhl14	-3.6	Redrum	-3.3	RP23-171B16.2	-3.0
	Megf6	-2.3	Klf15	-2.1	Sowaha	-3.6	Rhag	-3.3	Alas2	-3.0
	Wscd2	-2.2	Asb15	-2.0	Hbb-bs	-3.5	2810030D12Rik	-3.3	Iglc2	-3.0
	Kcnk3	-2.2	Abca6	-2.0	Hbq1b	-3.5	Hemgn	-3.3	Cacna1i	-3.0

	Full Fracture									
	Hour 4		Day 1		Day 3		Day 7		Day 14	
	Gene	FC	Gene	FC	Gene	FC	Gene	FC	Gene	FC
Up-regulated	Cxcl2	328.2	Arg1	234.3	Gm7325	73.7	Col9a1	440.5	Col10a1	97.0
	Cxcl1	276.9	Il11	188.9	Arg1	59.0	Ucma	437.9	Clec3a	54.0
	Csf3	275.0	Cxcl3	172.2	Tmem8c	56.0	Matn3	434.3	Panx3	47.0
	Il6	183.8	Cxcl2	81.4	Chrng	47.6	Lect1	415.2	3110079O15Rik	43.1
	Cxcl3	167.8	Ccl7	63.1	Il11	47.3	Clec3a	392.6	R3hdml	39.8
	Fosb	77.5	Ptgs2	49.1	Steap1	43.3	Col9a3	375.2	Col9a1	32.4
	Krt81	68.7	Ccl2	46.9	Pkhd1	38.5	Col10a1	328.1	Matn1	27.3
	Irg1	57.4	Spint1	32.1	Has2	35.9	Mfi2	320.7	Col9a2	27.0
	Ptgs2	55.5	Cxcl1	29.9	Ptgs2	35.6	Matn1	316.3	Mfi2	25.7
	Ccl2	51.6	Cxcl5	24.1	R3hdml	29.9	Col9a2	279.9	Lect1	24.8
Down-regulated	9430073C21Rik	-13.3	Cyp2e1	-30.0	Myl3	-44.0	Gp6	-43.1	Cyp2e1	-24.9
	Pck1	-10.4	Lrrc52	-19.3	Myl2	-40.8	Gm43291	-42.3	Ly6g6f	-23.9
	Gm28653	-9.9	Timp4	-13.5	Myh7	-31.8	Ly6g6f	-39.6	Gp6	-21.5
	Adrb3	-9.6	Aqp4	-13.3	Gm37527	-28.4	Ppbp	-37.6	G6b	-20.8
	Sln	-9.2	Col6a6	-12.5	Rp1	-25.4	Slamf1	-36.9	Mpl	-20.2
	Zic3	-8.1	Mylk4	-12.3	BC048679	-24.4	G6b	-36.8	Serpina3b	-19.5
	Dlx6os1	-8.1	A530016L24Rik	-12.2	Lrrc52	-24.2	Treml1	-35.1	Gm34302	-18.9
	Gm10629	-7.9	Lgi1	-11.9	Sowaha	-23.6	Tubb1	-33.0	Gp9	-18.8
	A930016O22Rik	-7.7	Pck1	-11.1	Perm1	-22.7	Gm42870	-33.0	Ppbp	-17.7
	A530016L24Rik	-7.7	Ces1d	-11.1	F930017D23Rik	-22.3	Gp9	-32.5	Treml1	-17.0

3.4.4 GO Term Analysis

115 GO terms were significantly enriched in at least one time point and fracture type (Figure 3.7 A). Of these, 17 GO terms were shared between both injuries, while 16 terms were unique to stress fracture and 82 were unique to full fracture (Figure 3.7 B). Enriched GO terms were compared across time points and injury type (Figure 3.7 C). Early time points showed no GO terms that were unique to stress fracture. In contrast, at day 3 through day 7 several terms related to osteogenesis were unique to stress fracture repair, such as "*collagen fibril organization*", "*osteoblast differentiation*", "*bone development*", "*bone mineralization*", and "*negative regulation of Wnt signaling*".

GO terms shared between stress and full fracture were few at early time points and included "*response to cytokine*" and "*positive regulation of transcription from Polr promoter"* at 4 hours, and "*positive regulation of cell migration*" at day 1 post injury. Later time points had shared terms such as "*angiogenesis*", "*extracellular matrix organization*", "*ossification*", and "*cartilage development*".

Terms unique to full fracture repair included those related to inflammation ("*inflammatory response*", "*chemokine-mediated signaling pathway*", "*cellular response to IL-1*", and "*innate immune response*"), metabolism ("*oxidation-reduction process*", "*glucose metabolic process*", and "*response to hypoxia*"), and ion transport ("*potassium ion transmembrane transport*", "*cellular calcium ion homeostasis*", and "*ion transport*").

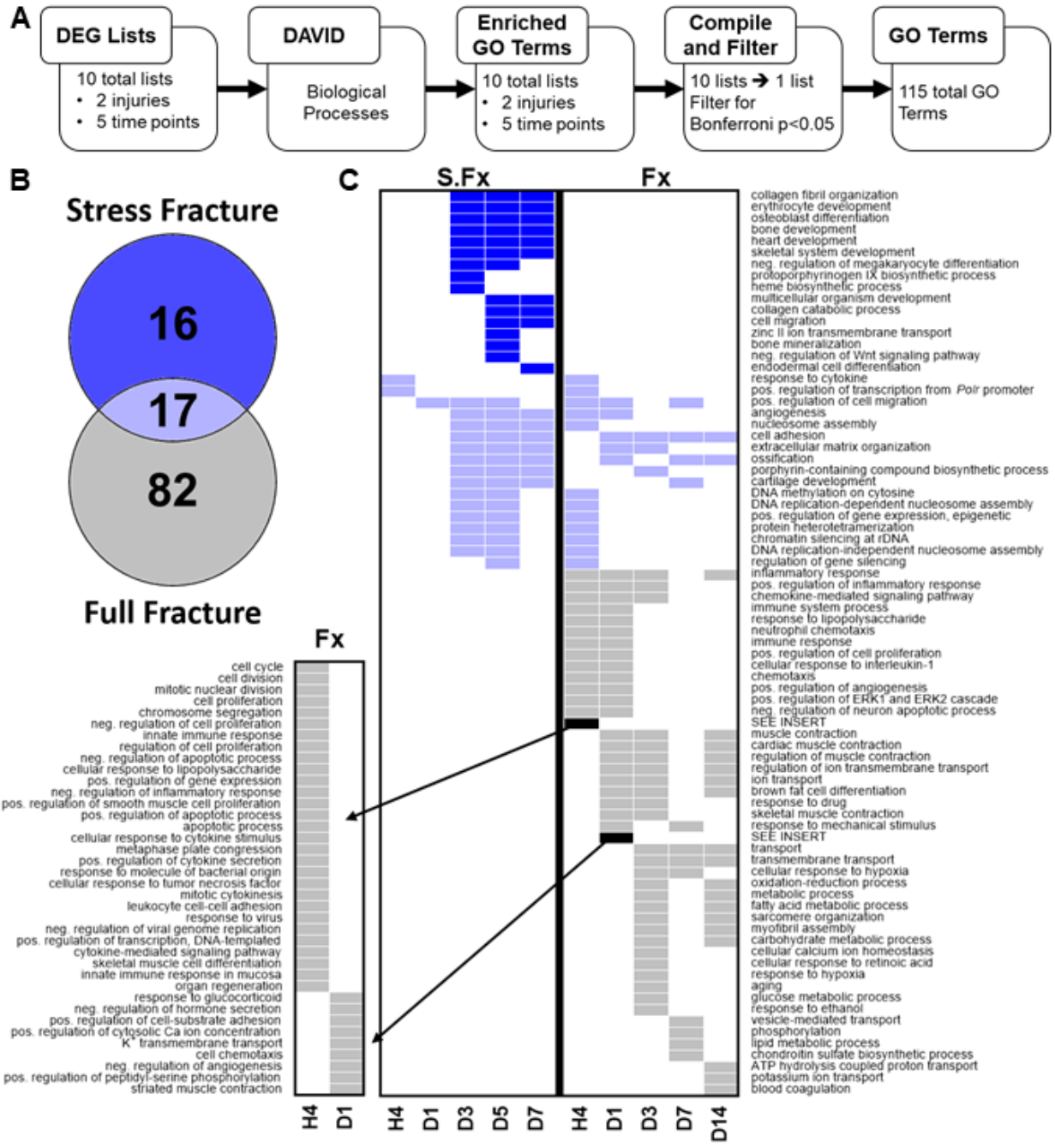

Figure 3.7: Gene ontology analysis of DEGs. (A) Pipeline for gene ontology (GO) term analysis. **(B)** Comparison of the 115 GO terms uniquely enriched in stress fracture (dark blue), enriched in both injuries (light blue), or uniquely enriched in full fracture repair (grey). **(C)** Graphical list of all 115 enriched GO terms across all injuries and time points. Colors on chart match location of term from panel B. Go terms uniquely enriched in early full fracture time points were broken out into the smaller sub-panel for figure compactness (Black arrows). Blank spaces indicate GO term was not statistically enriched at time point or injury. H4 – 4 hour, D1 – day 1, D3 – day 3, D5 – day 5, D7 – day 7, D14 – day 14. S.Fx - stress fracture, Fx- full fracture

3.4.5 Pathway Analysis

60 pathways were significantly enriched in at least one time point and fracture type (Figure 3.8 A). Of these pathways, 12 were enriched in both stress and full fracture, while 3 were uniquely enriched in stress fracture, and 45 were uniquely enriched in full fracture (Figure 3.8 B). Of the three pathways unique to stress fracture, only the "*PI3K-Akt signaling pathway*" was enriched at multiple time points (Figure 3.8 C). Pathways that were shared between stress and full fracture repair include those related to the immune system and diseases ("*TNF signaling*", "*cytokine-cytokine receptor signaling*", "*systemic lupus erythematosus*", and "*malaria*") as well as pathways like "*ECM-receptor interactions*", "*focal adhesions*", and "*arginine and proline metabolism*". Pathways uniquely enriched in full fracture repair include those related to immune processes ("*Rheumatoid arthritis*", "*NFκB signaling*", "*toll-like receptor signaling*"), metabolism ("*glycolysis/gluconeogenesis*", "*insulin resistance*", "*galactose metabolism*") and cardiac muscle ("*hypertrophic cardiomyopathy*", "*cardiac muscle contraction*", "*calcium signaling*").

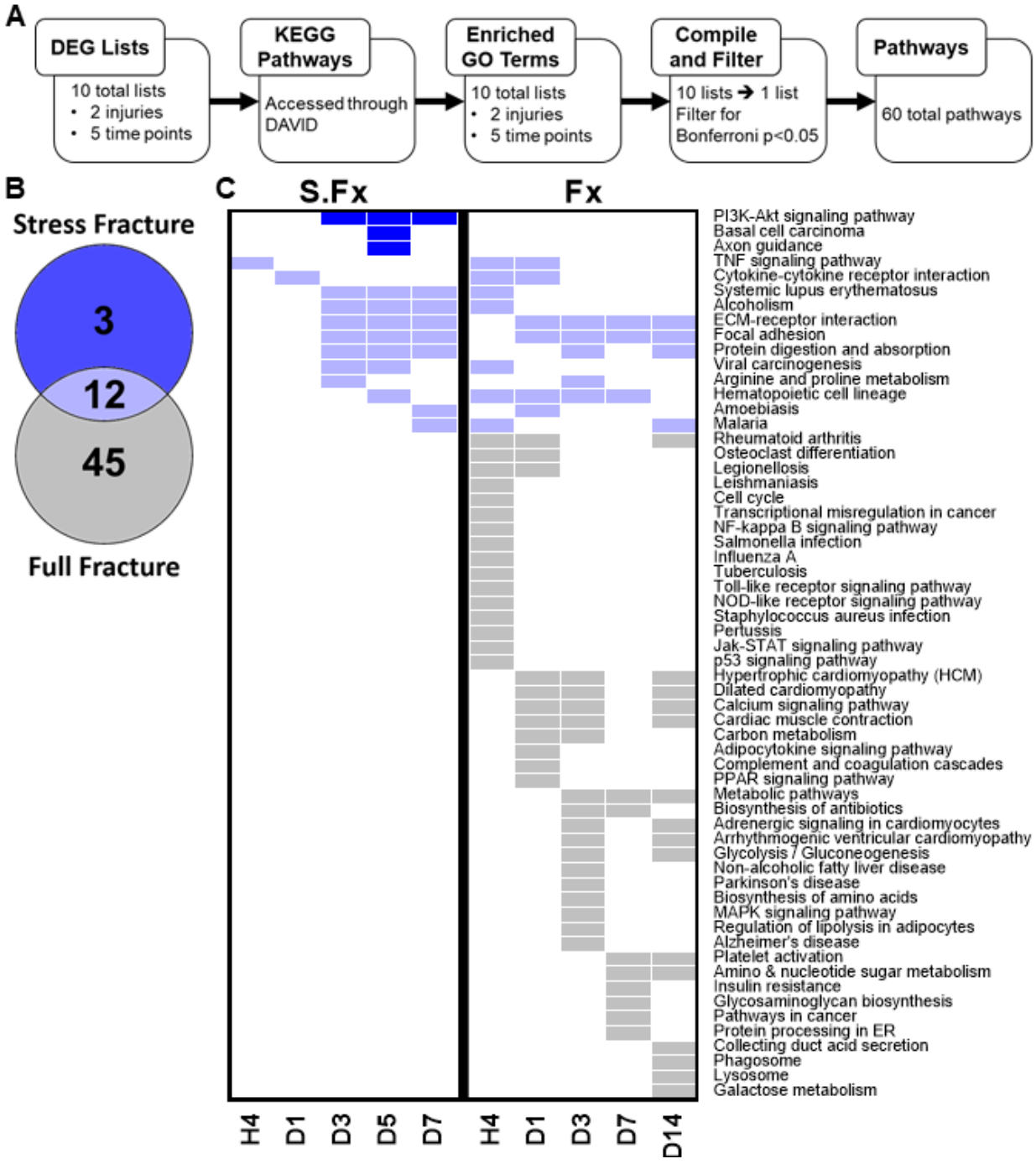

Figure 3.8: Pathway analysis of DEGs. (A) Pipeline for pathway analysis. **(B)** Comparison of pathways enriched in stress and full fracture repair. **(C)** Graphical list of all 60 enriched pathways across injuries and time points. Colors on chart match location of pathway on panel B. Blank spaces indicate no significance of pathway at that time point/fracture condition. H4 – 4 hour, D1 – day 1, D3 – day 3, D5 – day 5, D7 – day 7, D14 – day 14. S.Fx - stress fracture, Fx- full fracture

3.4.6 Callus Component Phenotyping

To estimate the abundance of cell types within fracture callus throughout repair, the fold change of genes on curated lists (Table 3.2) were compiled for each time point and fracture type (Figure 3.9). Neutrophil related genes were strongly upregulated at early time points (hour 4, day 1) following full fracture (Figure 3.9 A), and slightly increased after stress fracture (hour 4). At later time points, most neutrophil-related genes were downregulated (days 5, 7, and 14). Macrophage related genes displayed a mix of up- and downregulation within time points and thus no clear pattern was evident (Figure 3.9 B). Monocyte related genes were upregulated at multiple time points in both stress and full fracture, most strongly at early time points (hour 4 and day 1) after full fracture (Figure 3.9 C). T cell associated genes were upregulated early post stress fracture (hour 4) and full fracture (hour 4 and day 1), but suppressed at later time points (days 5, 7, and 14) (Figure 3.9 D). B cell related genes were mostly suppressed after stress fracture (days 1 - 7) and full fracture (days 3 - 14) (Figure 3.9 E). Osteoblast related genes were strongly expressed after stress fracture (days 3, 5, and 7) and to a slightly lesser extent following full fracture (days 3, 7, and 14) (Figure 3.9 F); these genes were down early (hour 4) post-full fracture. Osteoclast related genes did not show strong signal either up or down except for slight upregulation at the final time point of each injury (Figure 3.9 G). Endothelial cell related genes showed modest increases by later time points in both models (Figure 3.9 H). Chondrocyte related genes showed upregulation in both models at later time points (days 5, 7, and 14) (Figure 3.9 I).

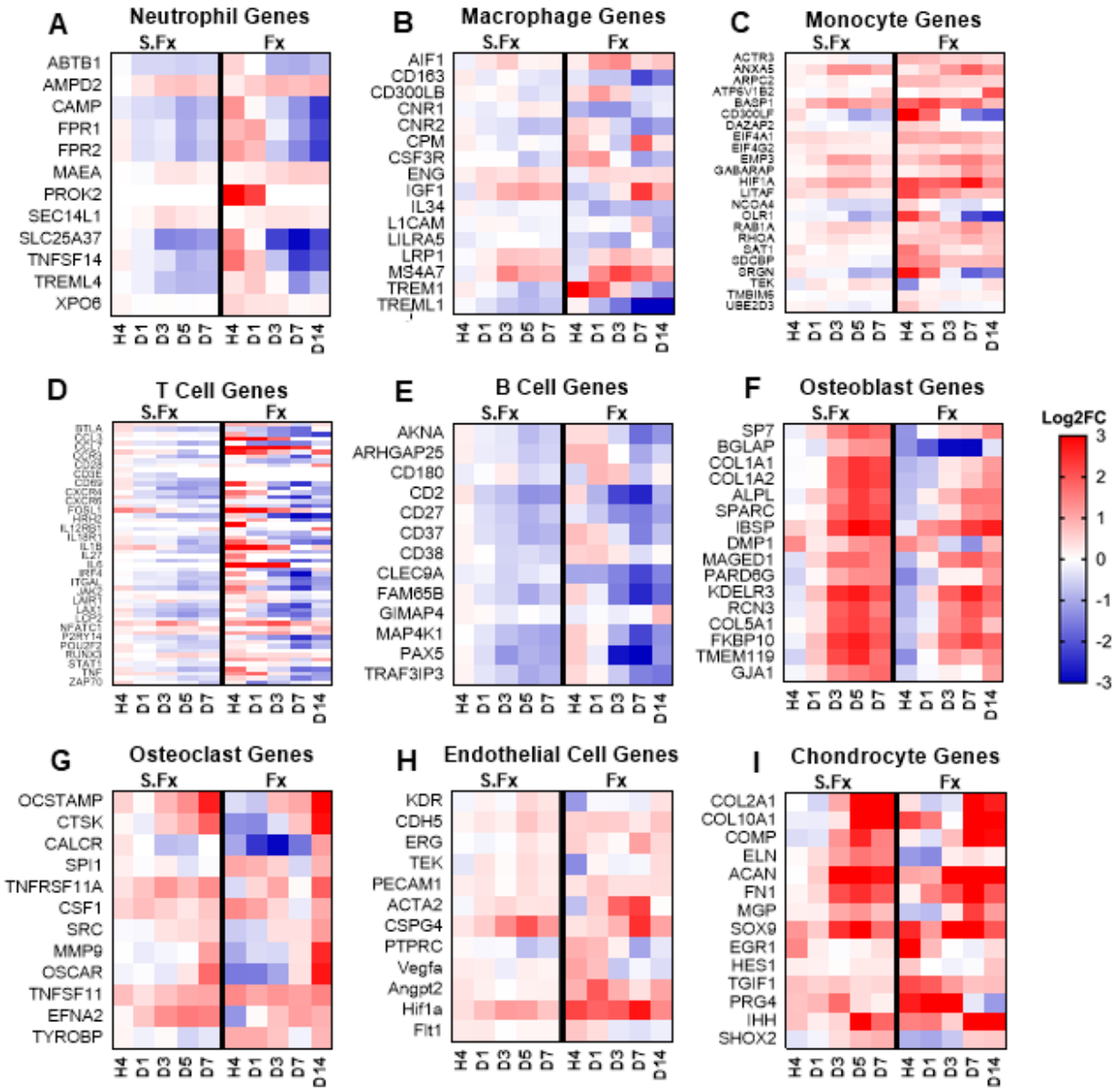

Figure 3.9: Callus component phenotyping heat maps. Heat maps (log2 fold change) were generated for each time point and injury of curated genes lists associated with **(A)** Neutrophils, **(B)** Macrophages, **(C)** Monocytes, **(D)** T Cells, **(E)** B Cells, **(F)** Osteoblasts, **(G)** Osteoclasts, **(H)** Endothelial Cells, and **(I)** Chondrocytes. Gene lists were generated using literature sources in Table 3.2.

3.4.7 IHC of fracture callus

Antibodies for Gr-1, F4/80, and CD45 were used to stain fracture callus to assess the presence of immune cells. Gr-1, a marker of neutrophils, was abundantly expressed in marrow in the contralateral control, but not in cortical bone, endosteum, or periosteum. At early post-injury time points (hour 4 - day 3) Gr-1 expressing cells were adjacent to the injury site in both stress and full fracture (Figure 3.10). This signal was diminished at later time points (days 5, 7 and 14) - consistent with the callus component phenotyping analysis and suggesting a reduced role for neutrophils after the early injury response. Staining for F4/80, a marker for macrophages, showed strong signal in the bone marrow of control ulna and femur, but not in cortical bone, endosteum, or periosteum. Stress fracture repair did not lead to robust F4/80 staining at any time point, with only modest local staining at hour 4 post-injury; this is consistent with the lack of a strong macrophage signal from callus component phenotyping analysis. By contrast, in full fracture, F4/80 staining was present in callus at all time points with the most robust staining at D3 post-injury. CD45, a general marker of leukocytes, was most abundant at 1 and 3 days post stress fracture. In full fracture, CD45 showed robust staining at early time points (hour 4 – day 3) and was reduced by day 7 and 14. In summary, neutrophils abound in early callus of both stress and full fracture while macrophages appear to be more abundant in full fracture callus than stress fracture.

To confirm that PI3K-Akt signaling was active in stress fracture repair, we performed IHC staining for p-Akt T308. Little staining for p-Akt was present in contralateral bone or at day 1 after injury (Figure 3.11). By days 3, 5, and 7 after injury, staining was observed in stress fracture callus, especially in areas within newly formed bone near the crack.

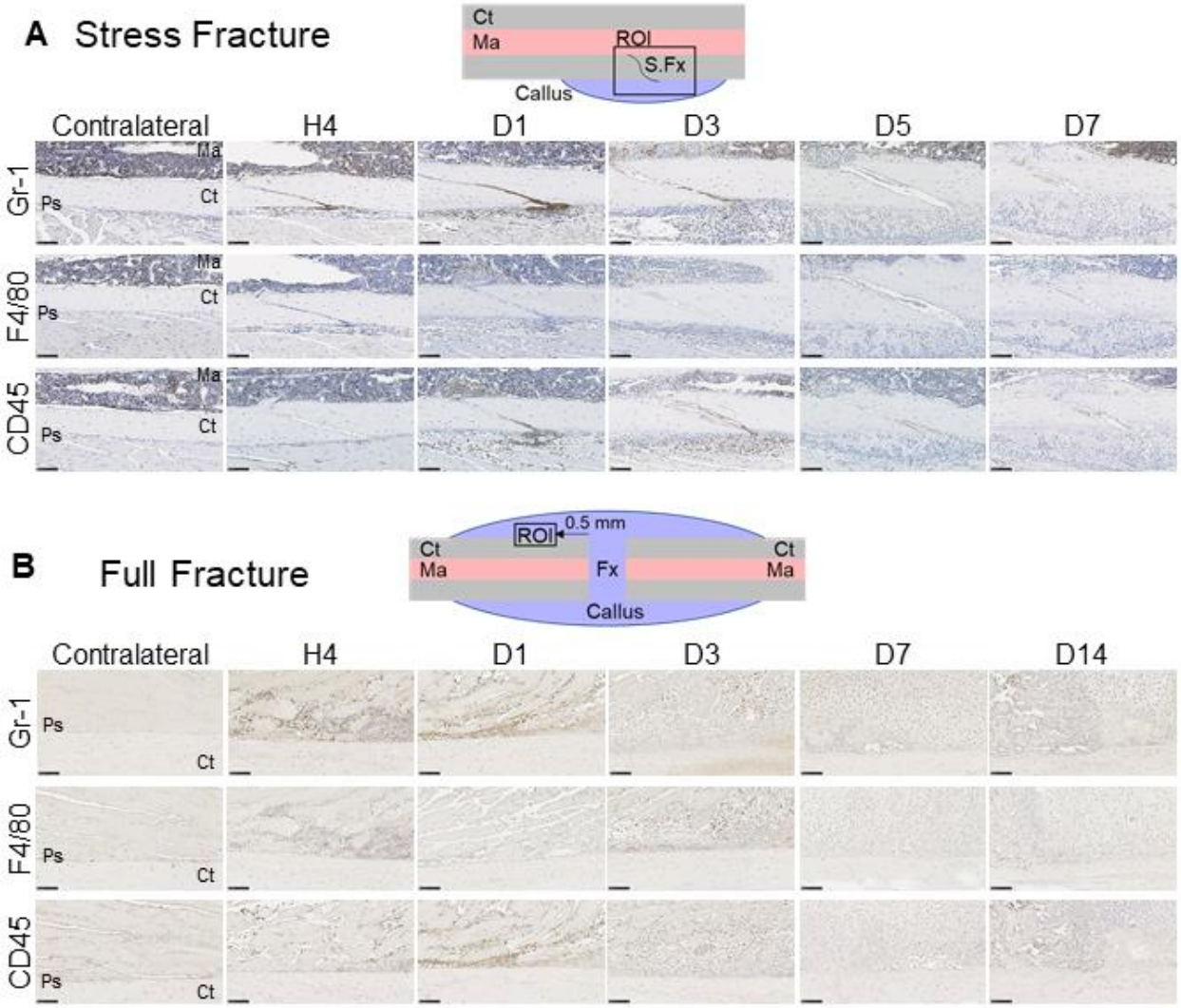

Figure 3.10: Immune cell infiltration in fracture callus. Immunohistochemistry with antibodies for Gr-1, F4/80, and CD45 was used to stain for neutrophils, macrophages, and leukocytes, respectively. Cartoon depictions of the fracture callus show Region of interest (ROI) (Black box) in reference to **(A)** stress fracture (S.Fx) or **(B)** full fracture (Fx) location. All images are 20X magnifications and black scale bars are 100 μm. Ct = Cortical Bone, Ma = Marrow, Ps = Periosteum

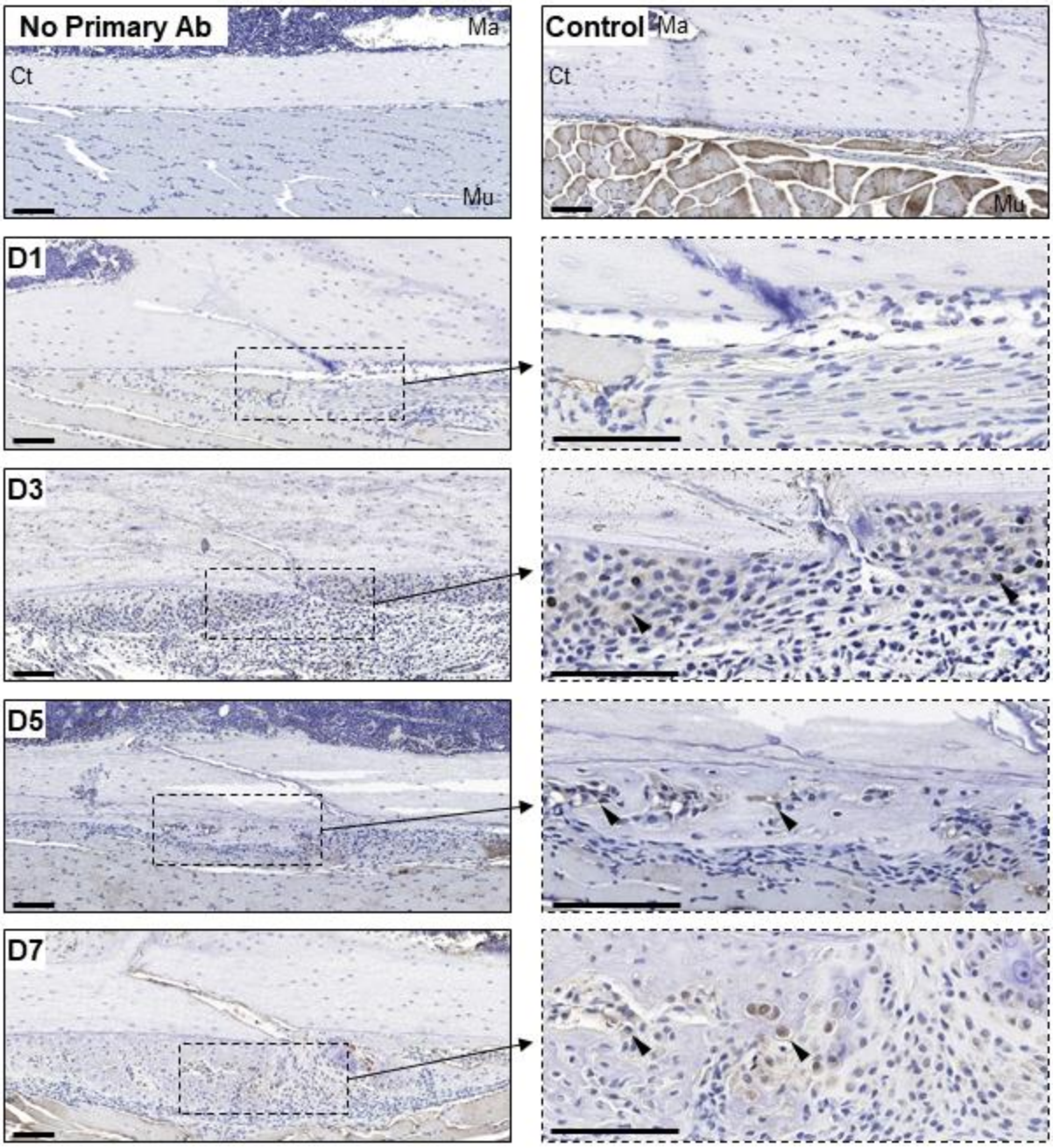

Figure 3.11: Activation of PI3K-Akt signaling in stress fracture callus. IHC staining for p-Akt T308 was performed on paraffin embedded histology slides of stress fracture callus. In contralateral control ulna no staining is evident in bone tissue, but staining is observed in adjacent muscle tissue. Little staining is observed at day 1 after stress fracture. Staining can be observed within the fracture callus at days 3, 5, and 7 post stress fracture. Arrows are used to mark examples of positive stained cells. Scale bars are 100 μm in length.

3.5 Discussion

Our work describes and compares gene transcription in intramembranous and endochondral ossification using RNA-seq during stress fracture and full fracture repair, respectively. Several reports have examined gene expression of endochondral [80–84] or intramembranous repair [29]. However, our study is unique in making direct comparisons between the gene expression in these two different repair processes. Furthermore, we took a wider breadth than previous work by tracking gene expression over several time points for each model. Through analysis of top DEGs, and enriched GO terms and pathways for each fracture modality, we described how these expression patterns differed and progressed through time. We also employed callus cellular phenotyping techniques to estimate cell types within callus throughout repair. Finally, we used IHC to confirm the presence of some immune cell types in callus and surrounding tissues.

Although some DEGs were shared between stress fracture and full fracture repair, each of these models show a high level of distinct DEGs. This suggests that some fundamental processes are necessary for bone repair regardless of injury type – but that endochondral and intramembranous bone formation also have many distinct processes not shared between these models. We observed gradual gene expression changes following stress fracture, with few DEGs at early time points (Figure 3.4 A). However, by day 3 a robust number of DEGs were present at levels that persisted through our final time point (day 7). Contrastingly, we observed immediate and drastic changes in gene expression following full fracture, with thousands of DEGs at early time points, which was sustained at high levels throughout observed time points (Figure 3.4 B). This higher differential expression following full fracture is likely due to the more extensive

injury of full fracture, as well as the greater variety of cells involved in endochondral ossification as compared to intramembranous ossification.

A key difference in gene expression between stress and full fracture arises from the larger inflammatory reaction in full fracture injury. This is highlighted by GO terms and pathways uniquely enriched during full fracture repair such as "*inflammatory response*", "*immune response*", "*cellular response to interleukin-1*", "*NFκB signaling*" and "*Toll-like receptor signaling*". These results are indicative of a highly inflamed bone microenvironment following fracture, matching literature reports of the components and importance of the inflammatory phase of fracture repair [5,120]. Specifically, IL-1 [33,121] and NFκB [120] have already been studied in endochondral fracture repair and thus validate our highly enriched pathway analysis for these terms. However, our pathway analysis showed enriched genes associated with toll-like receptors, which haven't previously been studied during endochondral fracture. These receptors, based on other reports, could be involved in monocyte recruitment, osteoblast differentiation, and tissue repair – however, the specific role they play in fracture repair needs to be further explored [122,123].

Stress fracture repair also features inflammation, with GO terms and pathways such as "*response to cytokine*", "*TNF signaling pathway*", and "*Cytokine-cytokine receptor interaction*" shared between both injuries. This pattern of inflammation differs from that in microarray results of rat stress fracture reported by McKenzie et al, wherein IL-1, toll-like receptors, and NFκB were more prominently featured among DEGs [29]. Ptgs2 (aka Cox-2), a critical mediator of inflammation, was one of the most upregulated genes at several time points following stress fracture and full fracture (Table 3.3), and is a known contributor to successful healing [30,124]. Although it is certainly involved in stress fracture repair, the inflammatory reaction appears to be

less extensive than after full fracture, both in terms of the numbers of relevant DEGS and their fold change.

The higher inflammation seen in the GO term and pathway analysis is also observed in callus cellular phenotyping and IHC analysis of fracture callus. Full fracture has a larger upregulation of immune-cell related genes as well as greater staining for Gr-1, F4/80, and CD45 than stress fracture (Figure 3.9 & 3.10). Recruitment of neutrophils, macrophages, and leukocytes to the site of injury at early time points is robust in our dataset. This is indicative of a healthy repair process, as these cells are important components of fracture repair [21,24,125]. Furthermore, IHC evidence of immune cell recruitment corroborates that the inflammatory signal in the RNA-seq data is functionally present in fracture repair at the cellular level. In addition, the callus phenotyping data showed an upregulation of T cell markers at early time points (hour 4 and day 1) following full fracture and to a lesser extent stress fracture. This is consistent with a report of T cell infiltration at early time points after full fracture [9]. But, how T cells impact fracture repair remains poorly understood. Reports show that elimination of the adaptive immune system benefits healing, but other reports show that elimination of certain subsets of T cells are detrimental to repair [25,126].

Our results indicate that stress fracture repair is a more direct model of post-injury osteogenesis. GO terms such as "*osteoblast development*", "*bone development*", "*skeletal system development*", and "*bone mineralization*" are uniquely enriched following stress fracture (Figures 3.7 & 3.8). Furthermore, in callus phenotyping, osteoblast associated genes are the strongest signal for any cell type following stress fracture (Figure 3.9 F). While full fracture is a mix of several important processes (i.e. osteogenesis, chondrogenesis, and inflammation), these additional processes can complicate interpretation of experiments designed to test defects in

ossification. On the other hand, stress fracture repair involves fewer processes and cell types and therefor elicits strong enrichment of bone cell and osteogenic signals.

While stress fracture is a simplified model of post-injury osteogenesis, it elicits a distinctive and more complex transcriptional process than non-injurious anabolic bone formation. Kelly et al. used RNA-seq to determine expression changes in cortical bone following anabolic loading stimulation [127]. Few of the DEGs in their analysis were DEGs at similar time points following stress fracture (Figure 3.12). This agrees with previous reports showing stress fracture-induced intramembranous bone formation is transcriptionally distinct from loading-induced lamellar bone formation [29].

The PI3K-Akt signaling pathway is the only pathway uniquely enriched at multiple time points in stress fracture repair (Figure 3.8). We also observed activation of this pathway in stress fracture callus using IHC (Figure 3.11). Interestingly, this pathway is important for osteoblast differentiation and function [128,129]. A few studies have examined this pathway in fracture repair. Qu et al. noted that inhibition of Akt signaling reduces MSC engraftment into fracture callus in a rescue model for rat non-union [130]. They further postulate that Akt signaling modulates post-injury osteogenesis via production of osteoprotegrin and bone gla protein. Furthermore, Scanlon et al. reported that PI3K can regulate thickening of the periosteum during the early stages of fracture repair [131]. These papers, along with our data, suggest PI3K-Akt signaling is an important and understudied component of bone regeneration.

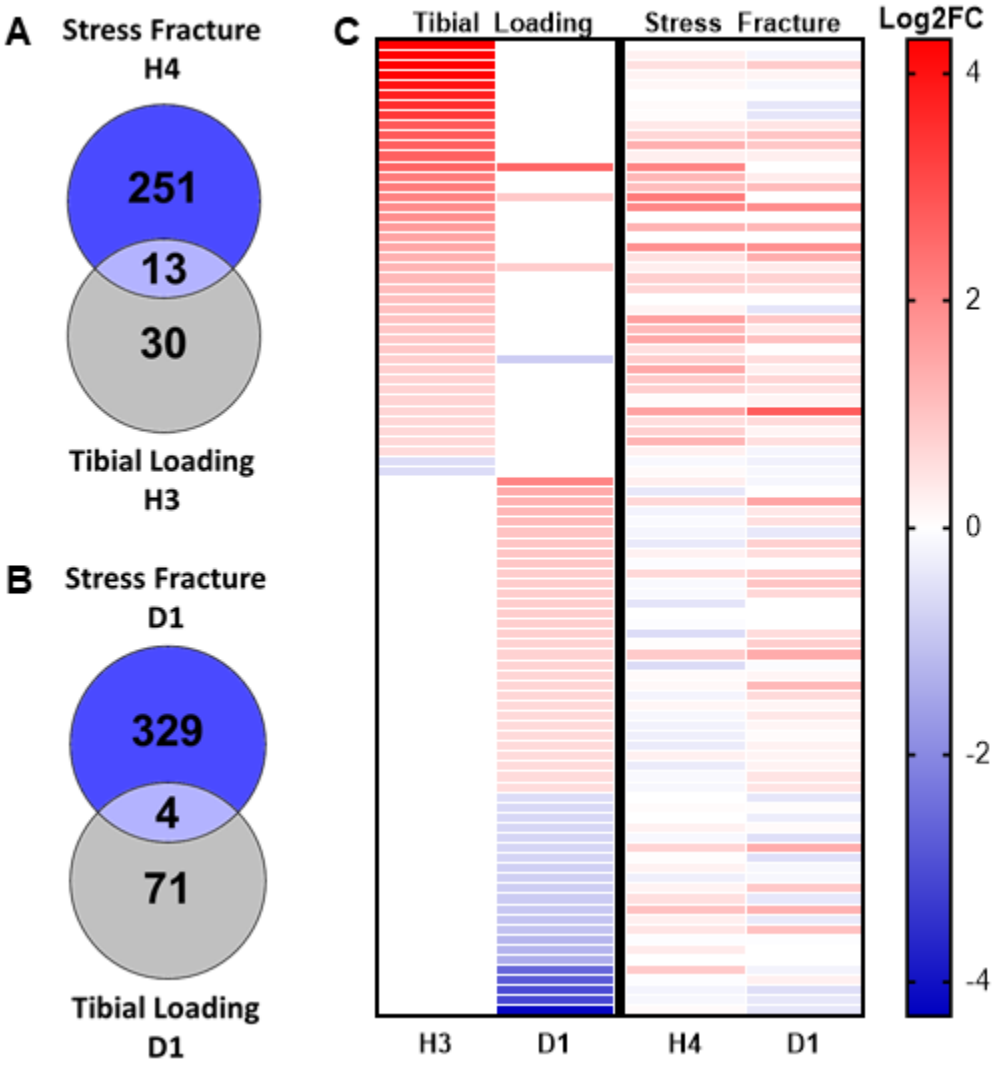

Figure 3.12: Comparison of stress fracture transcriptome to anabolic loading transcriptome. Of the 100 DEGs reported by Kelly et al. to be differentially regulated in cortical bone following anabolic tibia loading, few are also DEGs following stress fracture. **(A)** Only 13 DEGs are shared between hour 4 following stress fracture and hour 3 following tibia loading. **(B)** Only 4 DEGs are shared between stress fracture and tibia loading on day 1 following each model. **(C)** Log2 FC for all 100 DEGs reported 3 hours and 1 day after tibia loading in Kelly et al. and the Log2 FC of those same genes at 4 hours and 1 day after stress fracture.

Another difference between stress and full fracture repair is the host of ion transport-related GO terms ("*ion transport*", "*cellular calcium homeostasis*", "*potassium ion transmembrane transport*") and pathways ("*calcium signaling pathway*", "*cardiac muscle contraction*") which are uniquely enriched following full fracture. These terms were triggered by downregulation of calcium, potassium, and sodium voltage-gated channels (Figure 3.12, Table 3.4). One possibility for this downregulation includes ion channels directly influencing bone regeneration. Studies show ion channels involved in development and regeneration through endogenous bioelectrical patterning [132]. In fact, interfering with ion channels causes defective tail regeneration in amphibians [133]. Ion channels also have roles in bone cells, as potassium voltage gated channels regulate inflammation-induced bone resorption [134] and sodium voltage gated channels impact osteoblast function [135]. Reports of ion channels in bone repair have contradictory results [136,137] and would benefit from future exploration. The downregulation of ion channels could also involve pain sensation. Sodium, potassium, and calcium channels are components of pain sensation, and dysregulation of these channels result in painful neuropathies and hypersensitivities [138–140]. Furthermore, ion channels are downregulated in response to injury, contributing to post-injury mechanical hypersensitivity [141,142]. Whether ion channels impact fracture repair through either of these possible mechanisms or through a yet undiscussed mechanism, their downregulation is robust in full fracture repair and an appealing target for future study.

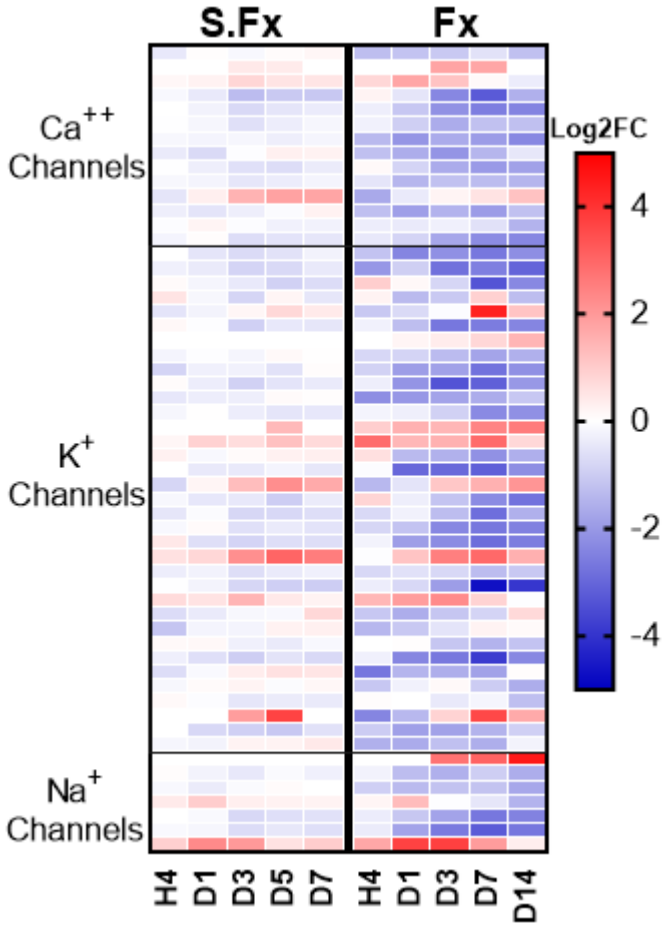

Figure 3.13: Ion channels are downregulated following full fracture. The Log2 FC of Calcium, Potassium, and Sodium Voltage Gated Channels which were DEGs are displayed across all time points for stress fracture (S.FX) and full fracture (FX). These channels were disproportionally down-regulated throughout full fracture repair. Due to these down-regulated DEGs, Go terms and pathways such as "*ion transport*", "*cellular calcium homeostasis*", "*potassium ion transmembrane transport*', "*calcium signaling pathway*", and "*cardiac muscle contraction*" were enriched during full fracture repair. A full list of these genes is provided in Table 3.4.

Table 3.4: Genes displayed in comparison of ion channel expression

Group	Gene IDs
Ca++	*Cacna1a, Cacna1b, Cacna1d, Cacna1E, Cacna1S, Cacna2d1, Cacnca2d2, Cacna2d3, Cacna2d4, Cacnb1, Cacnb3, Cacnb4, Cacng1, Cacng6*
K+	*Kcna1, Kcna2, Kcna3, Kcna5, Kcna6, Kcna7, Kcnab3, Kcnb1, Kcnb2, Kcnc1, Kcnc2, Kcnc4, Kcne3, Kcne4, Kcnf1, Kcng4, Knch2, Kcnh7, Kcnj10, Kcnj11, Kcnj12, Kncj15, Kcnj2, Kncj5, Kcnk13, Kcnk2, Kcnk3, Kcnk7, Kcnn2, Kcnq2, Kcnq4, Kcnq5, Kcns1, Kcnt1, Kcnt2*
Na+	*Scn1a, Scn1b, Scn2b, Scn3b, Scn4a, Scn4b, Scn5a*

By using a contralateral control of intact bone, which is inherently enriched for bone cells, callus composed of a variety of cell types will have “differential expression” which is the result of different cellular composition in addition to true changes in gene expression of native cells. This should be kept in mind when considering the DEGs represented in this work as this likely limits our ability to capture expression changes of native bone cells. However, utilizing this as a feature of our whole callus sequencing allowed us to use callus cellular phenotyping to infer cell types present throughout fracture repair. Furthermore, it is possible that the surgery performed while initiating the full fracture could itself influence gene expression when comparing to a no surgery contralateral control. Despite this possibility, we believe that fracture is the primary driver of gene expression and is responsible for the large differential expression reported herein.

3.6 Conclusions

In this report the gene expression of bone repair is examined using two models of murine fracture repair. Intramembranous repair, as modeled by ulnar stress fracture, and endochondral repair, as modeled by femur full fracture, exhibit vastly different transcriptional profiles throughout repair. Full fracture repair includes a much stronger inflammatory response and a down regulation in ion transporter genes not experienced in stress fracture repair. Within stress fracture repair is a strong signal of osteoblasts and osteogenesis which reflects a simpler repair process. These data offer a detailed description of gene transcription in bone fracture repair, and highlight several pathways and processes as potential new avenues of research that may lead to innovative solutions to clinical complications in fracture repair.

Chapter 4: Interleukin-6 (IL-6) deficiency enhances intramembranous osteogenesis following stress fracture

4.1 Introduction

Inflammation governs the initial response of the skeleton to injury. This inflammatory process is a critical component of successful healing and lays the foundation for the subsequent repair cascade. Of the various stages of fracture healing, the inflammatory phase remains the least understood. However, various data implicate the importance of this phase to successful repair. Firstly, inflammation must be tightly controlled both in extent and time-course [11,143]. If the inflammatory process is stunted, for example through use of nonsteroidal anti-inflammatory drugs, healing can be negatively influenced [20]. Additionally, if the inflammatory phase is abnormally high, which can occur in diabetic or obese patients, healing can also be negatively affected [14,16]. These examples point to the importance of the inflammatory phase as a critical initiator of the fracture repair process that must be tightly controlled to achieve optimal healing. A more thorough understanding of the role of the cells and cytokines contributing to this phase will aid in understanding how the inflammatory phase aids in fracture repair.

The critical components of the inflammatory phase of repair are still incompletely understood. Reports have shown that interleukin-6 (IL-6) is an early responding gene transcript following fracture [28] and stress fracture [29] with substantial transcriptional upregulation

following skeletal injury. However, the contributions of IL-6 to skeletal repair, particularly within the inflammatory phase, remain understudied.

IL-6 is a pleotropic cytokine with a multitude of functions across various biological processes and has been described to have both pro- and anti-inflammatory effects [144]. In non-skeletal injury models, IL-6 has been shown to mediate various inflammatory processes, in particular IL-6 is a mediatory of the transition between the neutrophil dominated initial response to a more controlled macrophage dominated response [145,146].

IL-6 is known to play a role in skeletal health [147]. It has long been known that IL-6 promotes osteoclast formation and is associated with many osteoclast mediated bone pathologies [148,149]. The impact of IL-6 on osteoblasts is less understood and many conflicting reports exist. Some groups report IL-6 as inhibitory to osteoblast function [150–152] but others show IL-6 as a promoting osteoblast function [153].

Previous studies have highlighted that IL-6 knockout mice have delays in endochondral repair [34,35]. But these studies do little to elucidate the mechanism through which IL-6 impacts skeletal repair. Furthermore, no studies have examined the role of IL-6 in intramembranous repair.

In this work, we investigate how IL-6 impacts endochondral and intramembranous bone formation following injury through the use of IL-6 global and conditional knockout mice. We take a methodical approach to elucidate the mechanism through which IL-6 plays a role in skeletal repair by assessing the impact of IL-6 knockout on osteoblast function, osteoclast function, immune cell recruitment, and production of inflammatory molecules during stress fracture repair.

4.2 Methods

4.2.1 Mice

All animal work was performed within an IAUCUC approved protocol. In total, 174 mice were used. For global knockout studies, IL-6 knockout mice were obtained (Jackson Labs, #002650) and crossed with wild type C57BL/6J mice (Jackson Labs, #000664) [154]. Breeders were heterozygotes for IL-6 knockout and littermate IL-6 knockout homozygote (IL-6 KO) or IL-6 wild type (WT) pups were used in experiments. For conditional deletion studies, Osteocalcin Cre (#019509) and LysM Cre (#004781) mice were ordered from Jackson Labs and were crossed to IL-6 floxed mice (European Mouse Mutant Archive, 05332) [155]. All full fracture and stress fracture experiments were performed on 12 week old animals, while anabolic loading was performed on 5 month old animals and primary osteoblasts for cell culture were obtained from 1-3 day old neonates.

4.2.2 Full Fracture

Full fractures were created in the femur mid-diaphysis of mice (N = 19). Detailed methodology for this procedure has previously been reported [28,44]. In brief, mice were anesthetized (Isoflurane 1-3%, inhalation), and the right femur was exposed through an incision and notched at mid-diaphysis to predispose that site to fracture. The right hind limb was then secured in a custom fixture and a fracture was created via 3-point bending (30 mm/s displacement ramp) by a material testing machine (Instron Dynamite). Stabilization was achieved through placement of a 24 G pin into the medullary space, then the incision was closed. Radiographs

(Faxitron Ultra) were taken to ensure proper fracture location and pin placement and then mice were returned to unrestricted cage activity until sacrifice. Slow release buprenorphrine (1 mg/kg, s.c.) was used to control pain.

4.2.3 Stress Fracture

Stress fractures were created in the ulna diaphysis of mice (N = 92) using cyclic forelimb compression. Cyclic loading for stress fracture creation has been thoroughly detailed in previous reports [88,89]. Briefly, while anesthetized (Isoflurane 1-3%) the right forearm of the mouse was secured at the wrist and elbow in custom fixtures on a hydraulic material testing machine (Instron Dynamite). Force controlled cyclic loading at 2 Hz was performed until reaching a desired displacement, at which a stress fracture has formed. Loading parameters for each strain were determined using a set of calibration animals (N = 29) to determine ultimate force of the forelimb and cyclic displacement to complete fracture of the ulna (Table 4.1). The left ulna served as a contralateral control. Mice were then administered buprenorphine (0.1 mg/kg, s.c.) and returned to unrestricted cage activity until sacrifice.

Table 4.1: Stress fracture calibration data for IL-6 mouse strains.

Strain	Ultimate Force (N)	Cyclic Loading Force (N)	Displacement to Fracture (mm)	Cyclic Stopping Displacement (mm)
IL-6 KO (n = 15)	4.0 ± 0.4	3.0	0.96 ± 0.28	0.48
LysM cKO (n = 6)	3.9 ± 0.4	3.0	0.95 ± 0.15	0.48
Oc cKO (n = 8)	4.4 ± 0.3	3.3	1.17 ± 0.13	0.59

4.2.4 MicroCT Analysis

Intact femurs were analyzed by microCT to assess if IL-6 knockout had a baseline impact on bone development. Femurs of IL-6 KO and WT mice were scanned on a Scanco VivaCT system at power of 55 kVp, intensity of 145 mA, integration time of 300 ms, and voxel size of 10.5 μm. To assess cortical bone, 100 slices surrounding the midpoint of the femur diaphysis were analyzed for cortical thickness, bone area, marrow area, tissue mineral density and polar moment of inertia. To assess cancellous bone, 100 slices were analyzed in the distal femur beginning just proximal to the growth plate. Parameters such as bone volume fraction, bone mineral density, trabecular thickness, trabecular separation, and trabecular number were obtained and compared. All parameters were evaluated by 2-way ANOVA with factors of genotype and sex.

Mice were sacrificed for microCT (μCT) analysis 14 days following full fracture or 7 days following stress fracture. Full fracture samples had the intramedullary pin removed and were scanned on a Scanco VivaCT using the same parameters as described for intact femurs. Scans were manually contoured for callus volume on 600 slices surrounding the mid-point of the fracture gap. Total volume was calculated as the volume within all contours and bone volume represented the volume of pixels with densities above a threshold high enough to represent bone. It is important to note the inclusion of incumbent cortical bone within these measurements, therefore not all reported bone volume is newly formed after injury. Stress fracture samples were scanned using a Scanco MicroCT 40 with 70 kVp power, 114 μA intensity, 300 ms integration time, and 10 μm voxel size. Samples were contoured to select only the new callus for

analysis and contours were drawn for the entirety of the callus. Total callus volume was the volume of the contours and the bone volume was the volume within the callus with density over.

4.2.5 Histology

Forelimbs were collected after either 1, 3, or 7 days following stress fracture and fixed in 10% neutral buffered formalin for 24 hours. Following fixation, forelimbs were decalcified by 14% EDTA for 2 weeks. Forelimbs were then embedded in paraffin and sectioned in the transverse plane at 5 μm thickness. Slides from the 7 day group were stained with TRAP to identify osteoclast activity within stress fracture callus. Bioquant software was then used to quantify osteoclast number per bone surface and osteoclast surface per bone surface to compare between IL-6 KO and WT mice. Slides from the day 1 and day 3 groups were used for immunohistochemistry to stain for antibodies associated with early responding immune cells in order to probe if IL-6 KO impacts the recruitment of immune cells to the site of injury following stress fracture. To identify neutrophils an antibody for Gr-1(Bio-Rad MCA2387T, 1:500 dilution) was used and to identify macrophages an antibody for F4/80 (Bio-Rad MCA497RT, 1:500 dilution) was used. Both of these primary antibodies were used in conjunction with ImmPRESS Reagent Anti-Rat IgG (VectaShield MP-7404) kit and DAB to stain for their respective cell type. Slides were then imaged on a slide scanner (Hamamatsu Nanozoomer) at 20X magnification. Neutrophils and macrophages were then quantified using Bioquant software to obtain measurements of cell density in the calluses of IL-6 KO and WT mice.

Similarly, day 3 slides were stained for an antibody for proliferating cell nuclear antigen (PCNA) in order to assess cell proliferation following stress fracture (Cell Signaling Technology 13110T). Proliferating cells were quantified using the IHC plugin for Image J.

4.2.6 Anabolic Tibia Loading

To study the role of IL-6 KO on the anabolic capabilities of osteoblasts, we used the tibia compression model of loading induced bone formation [156,157]. Mouse hind limbs (N = 22) were situated in a custom loading fixture at the knee and ankle. Cyclic loading was then performed at 8 N peak force at 4 Hz for 60 cycles. Loading was performed for 5 consecutive days (days 1 -5). Calcein (10 mg/kg, i.p.) was administered to mice on day 5 and Alizarin Red (30 mg/kg i.p.) was administered on day 10 to label newly forming bone matrix. Mice were sacrificed on day 12 and tibia were processed for plastic embedded histology. Once embedded, transverse sections were cut 5 mm proximal to the tibial-fibular junction on a microtome and imaged using a Leica confocal microscope. Calcein and alizarin red labeling were then analyzed using Bioquant software for parameters such as mineralizing surface, mineral apposition rate, and bone formation rate [71]. Measurement of mineral apposition rate and bone formation rate included woven bone. Each parameter was analyzed using a repeated measure 3-way ANOVA with factors of loading (paired), sex, and genotype. Males and females were then subdivided and analyzed using repeated measure 2-way ANOVA with factors of loading (paired) and genotype. To understand the force-strain relationship in this particular mouse line, strain gauging was performed (N=12) using a previously described method [158].

4.2.7 Primary Osteoblast Culture

To study if IL-6 knockout impacts the ability of osteoblasts to differentiate and form matrix we assayed primary calvarial osteoblasts *in vitro*. Litters of IL-6 KO or WT one to three day old pups were pooled. Pups were sacrificed by decapitation and calvaria were removed, scraped clean of connective tissue, and stored in ice cold PBS until digestion. Once all calvaria were collected, scissors were used to cut calvaria into small pieces. Calvaria pieces then underwent serial digestion in Collagenase/Dispase (Sigma 11097113001) for 10 min/step at 37 C. Product from the first digestion was discarded and cells were collected from the subsequent four digestions. Cells were pooled in αMEM to deactivate collagenase after each digestion. Cells were then spun down, resuspended in 3 mL growth media (αMEM, 10% FBS, 1% PS) and plated in a 25 cm flask. Media was changed every other day and cells were checked for confluence. Upon nearing confluence, cells were trypsinized, counted, and seeded at 50,000 cells/well in a 24 well plate. Following seeding, cells were grown in osteogenic media (growth media with 50 μg/mL ascorbic acid and 3 mM glycerophosphate) for the duration of the experiment. Following 7 days in osteogenic media, cells were stained for alkaline phosphatase activity (Sigma 85L2) and staining was quantified by a plate reader at 405 nm. Following 21 days of culture in osteogenic media, cells were stained for mineralization with alizarin red and staining was quantified following ascorbic acid digestion of alizarin red at 405 nm.

To assess the impact of exogenous IL-6 on osteoblasts *in vitro*, wild type cells were cultured as detailed above. Either IL-6 (50 ng/mL, R&D Systems 406-ML), IL-6 soluble receptor (IL-6R, 100 ng/mL, R&D Systems 1830-SR), or the combination of each was added to wells throughout osteogenic induction and staining for alkaline phosphatase and alizarin were conducted as previously described. Due to the divergent actions of IL-6 classical and trans signaling on

osteoblasts, we designed the experiment to test both signaling modalities [153]. The addition of IL-6 only should recapitulate classical IL-6 signaling through membrane bound receptors on osteoblasts, IL-6 soluble receptor only will serve as a control, and IL-6 plus IL-6R will recapitulate trans signaling.

4.2.8 RNA-sequencing

To assess gene expression during the inflammatory phase of stress fracture repair, RNA-seq was used. Stress fractures were administered to IL-6 KO and control animals who were sacrificed at either 1 or 3 days post-injury. Ulna were dissected, flash frozen, and RNA was extracted using the protocol detailed above for tibia. RNA was then delivered to the Washington University Genome Technology Access Center where samples were sequenced on an Illumnina HiSeq platform. Reads were aligned to the Ensembl release 76 primary assembly (STAR version 2.5.1a). Gene counts were derived from the number of uniquely aligned unambiguous reads (Subread:featureCount 1.4.6-p5). Normalization for library size was performed (EdgeR). Differential expression analysis was then performed to analyze differences between conditions (Limma).

4.2.9 IL-6 deletion validation

In order to confirm knockout of *IL-6* in global knockout mice, we used lipopolysaccharides (LPS) to induce inflammation in cell cultures of IL-6 KO and wild type cells [159]. Osteoblasts were collected and expanded as stated previously (section 4.2.7). Induction of osteogenesis was begun (day 1) and LPS (5 μg/mL, Sigma L4391) was added to media on day 3, and media was collected for examination on day 5. An ELISA for IL-6 (Thermo Fisher, KMC0061) was used to examine IL-6 protein levels in media. Wild type cells had baseline levels of IL-6 around 70 pg/mL (Figure 4.1). Following LPS treatment, IL-6 significantly increased ($p<0.0001$) to levels greater than the detection limit of the ELISA (>500 pg/mL). IL-6 KO cells had baseline levels of IL-6 which were lower than the detection limit of the ELISA (<7.8 pg/mL) and did not significantly increase ($p=0.7513$) with LPS treatment. Therefore, we concluded that *IL-6* knockout was confirmed in these global knockout mice.

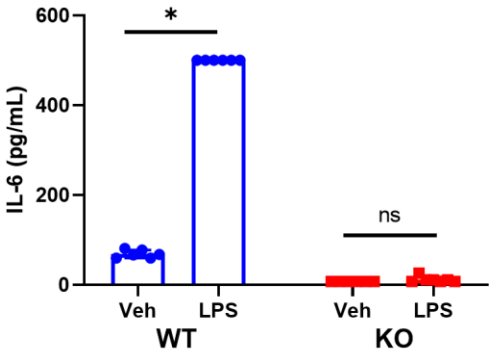

Figure 4.1: IL-6 KO is confirmed through ELISA. An ELISA for IL-6 was used to assess protein levels in cell culture media. Wild type mice had detectible levels of IL-6 at baseline which significantly increased with LPS treatment. IL-6 KO mice had undetectable levels of IL-6 at baseline which did not significantly increase with LPS treatment. Asterisk (*) denotes $p < 0.0001$.

In order to assess the knockdown efficiency of the conditional Cre mouse lines, bone marrow and tibia samples were collected from Oc cKO, and LysM cKO mice as well as relevant control animals for each strain. Bone marrow samples were immediately submerged in TRIzol, flash frozen, and stored at -80 C. Tibia samples were flash frozen and stored at -80 C, pulverized (Braun Mikrodismembrator), and then dissolved in TRIzol and stored at -80 C until processing. To extract RNA, TRIzol/sample solutions were processed with an RNA clean-up and concentration kit (Norgen Biotek). Then cDNA was produced (Bio-Rad iScript) using 500 ng of RNA from each sample. RT-qPCR was performed (Applied Biosystems StepOnePlus) using primers for *IL-6* (Mm. Pt. 58. 13354106), and reference genes *Tbp* (IDT, Mm. PT. 39a. 22214839) and *Ipo8* (IDT, Mm. PT. 39a. 22214844). Expression was normalized to reference genes and $2^{-\Delta Ct}$ expression values are reported. Comparisons between knockouts and controls were made using unpaired t-tests.

4.3 Results

4.3.1 Knockout of IL-6 does not impact skeletal morphology

MicroCT was used to evaluate uninjured femurs from IL-6 KO and WT mice to assess the skeletal development of IL-6 KO mice at 12 weeks of age (Figure 4.2). Cortical bone parameters reveal no genotype differences in cortical thickness, bone area, medullary area, tissue mineral density, or moment of inertia (Figure 4.2 A). Cancellous bone was also similar between genotypes in parameters such as bone volume fraction, bone mineral density, trabecular number, trabecular thickness, and trabecular separation (Figure 4.2 B). Two-way ANOVA revealed no genotype effect in any parameter.

4.3.2 Global knockout of IL-6 does not impair bone formation in endochondral ossification

Full fractures were created in IL-6 KO and wild type mice and calluses were measured by microCT 14 days later (Figure 4.3). IL-6 KO mice were able to form callus similar to wild type mice. Total callus volume, callus bone volume, bone volume fraction, tissue mineral density, and bone mineral density were all similar between groups (Figure 4.3 B-F).

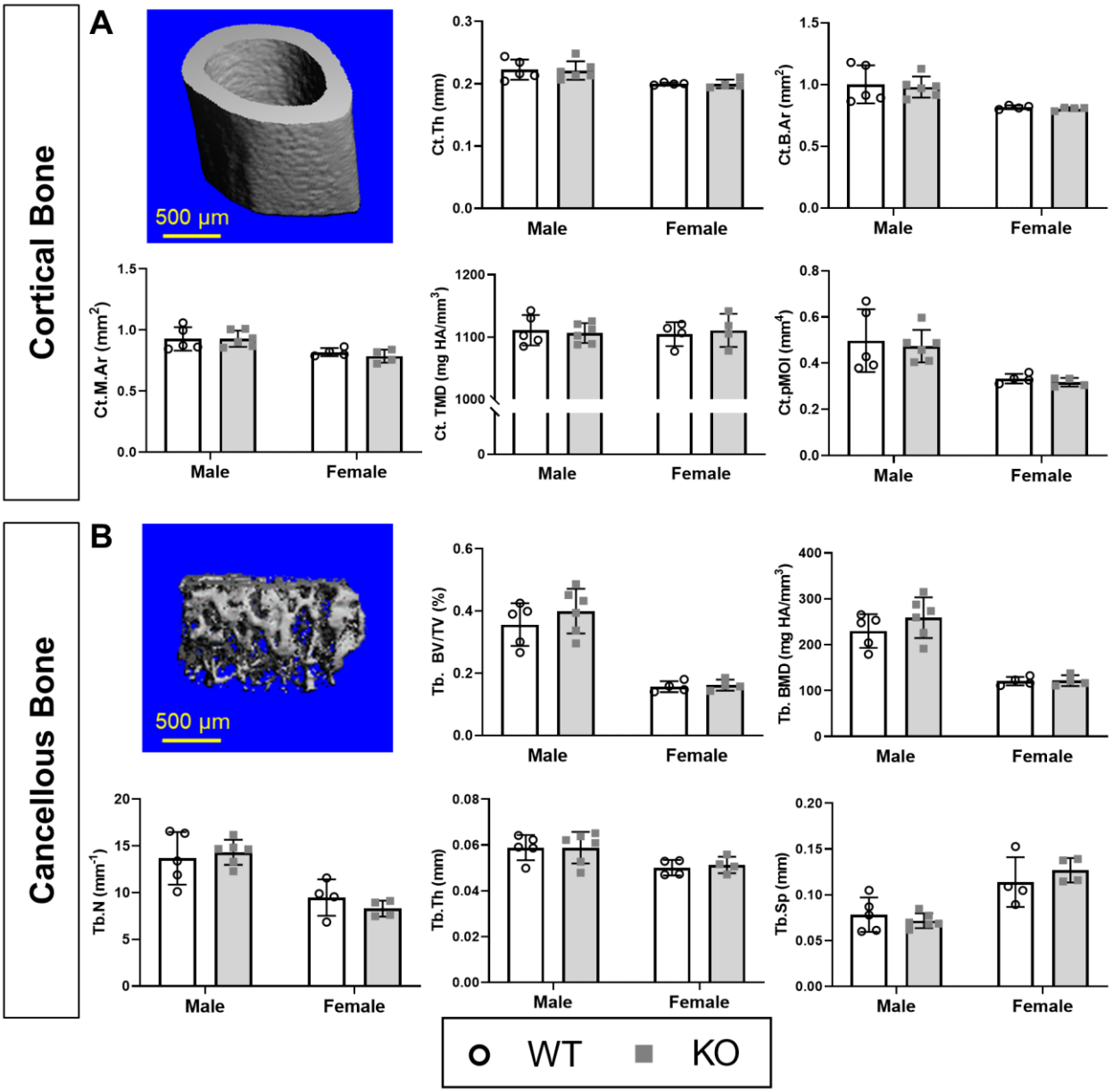

Figure 4.2: IL-6 KO did not impair skeletal morphology. MicroCT was used to assess cortical and cancellous bone in the femurs of 12 week old IL-6 KO and WT mice. Cortical analysis was performed at the femur mid-diaphysis. A representative reconstruction illustrates a typical sample. Cortical Thickness (Ct.Th), bone area (B.Ar), medullary area (M.Ar), tissue mineral density (TMD), and polar moment of inertia (pMOI) were similar between groups. Analysis of cancellous bone was performed in the distal femur. A representative reconstruction illustrates a typical sample. There were no differences between wild type and IL-6 KO for trabecular (Tb.) bone volume fraction (BV/TV), bone mineral density (BMD), trabecular number (Tb.N), thickness (Tb.Th), or separation (Tb.Sp).

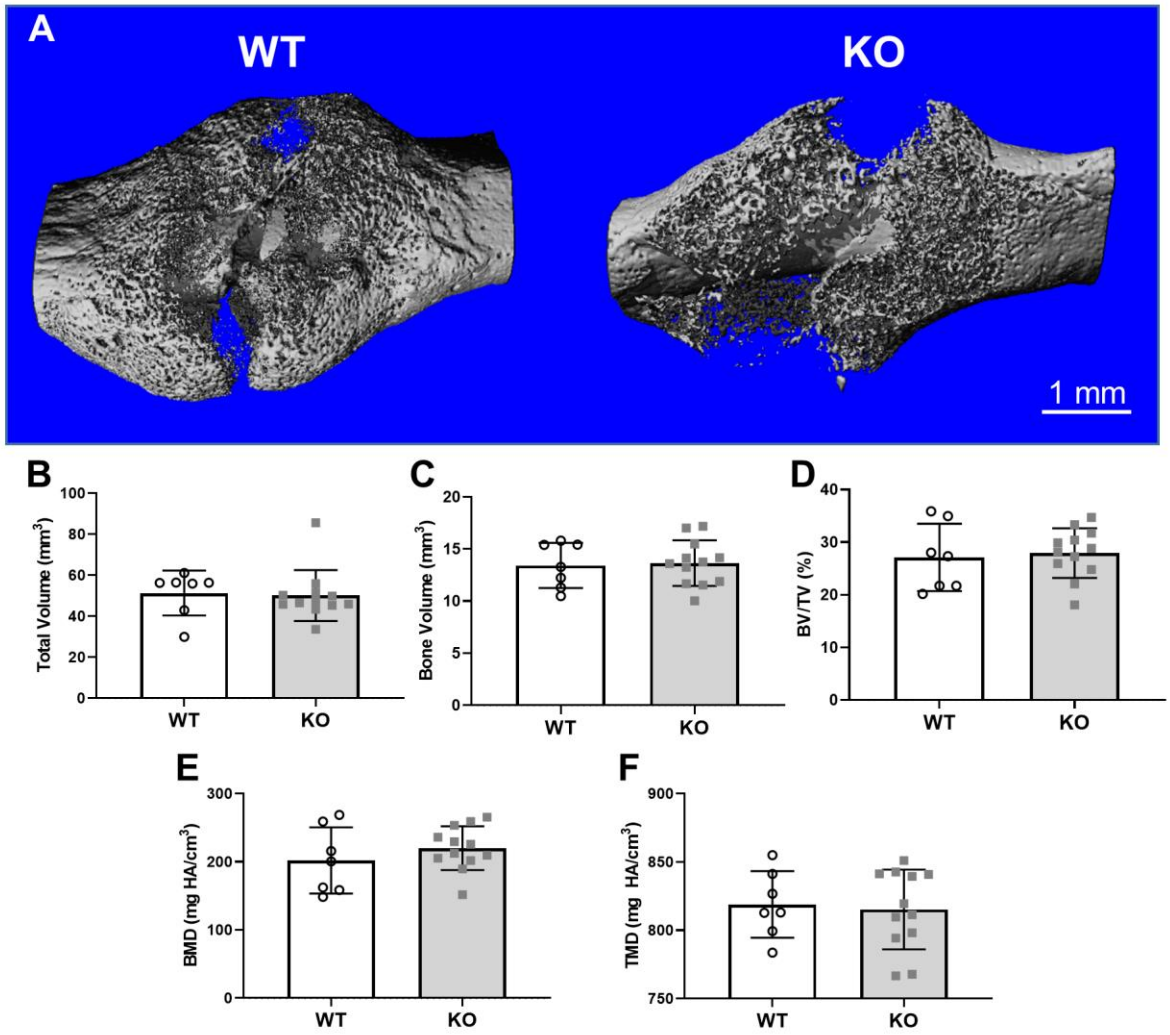

Figure 4.3: IL-6 KO did not alter full fracture callus formation. Day 14 full fracture callus was evaluated using microCT. (A) Representative wildtype (WT) and IL-6 KO callus reconstructions are shown. Callus total volume (B), bone volume (C), bone volume fraction (BV/TV) (D), bone mineral density (BMD) (E), and tissue mineral density (TMD) (F) are not different between groups.

4.3.3 Global knockout of IL-6 increases callus and bone formation in intramembranous ossification

Stress fractures were created in IL-6 KO and wild type mice and callus was measured by microCT 7 days later (Figure 4.4). IL-6 KO mice had significantly larger callus total volume ($p = 0.0202$) and bone volume ($p = 0.0446$) than wild type mice, representing an increased capacity for bone formation after stress fracture (Figure 4.3 B&C). The longitudinal length of the callus (woven bone extent) was also significantly increased ($p = 0.022$, Figure 4.3 D). Bone volume fraction was unchanged between groups. Bone mineral density and tissue mineral density of the callus were similar between groups. These data indicate that IL-6 KO contributes to larger callus formation and more bone formation in response to stress fracture, although the callus bone density is normal.

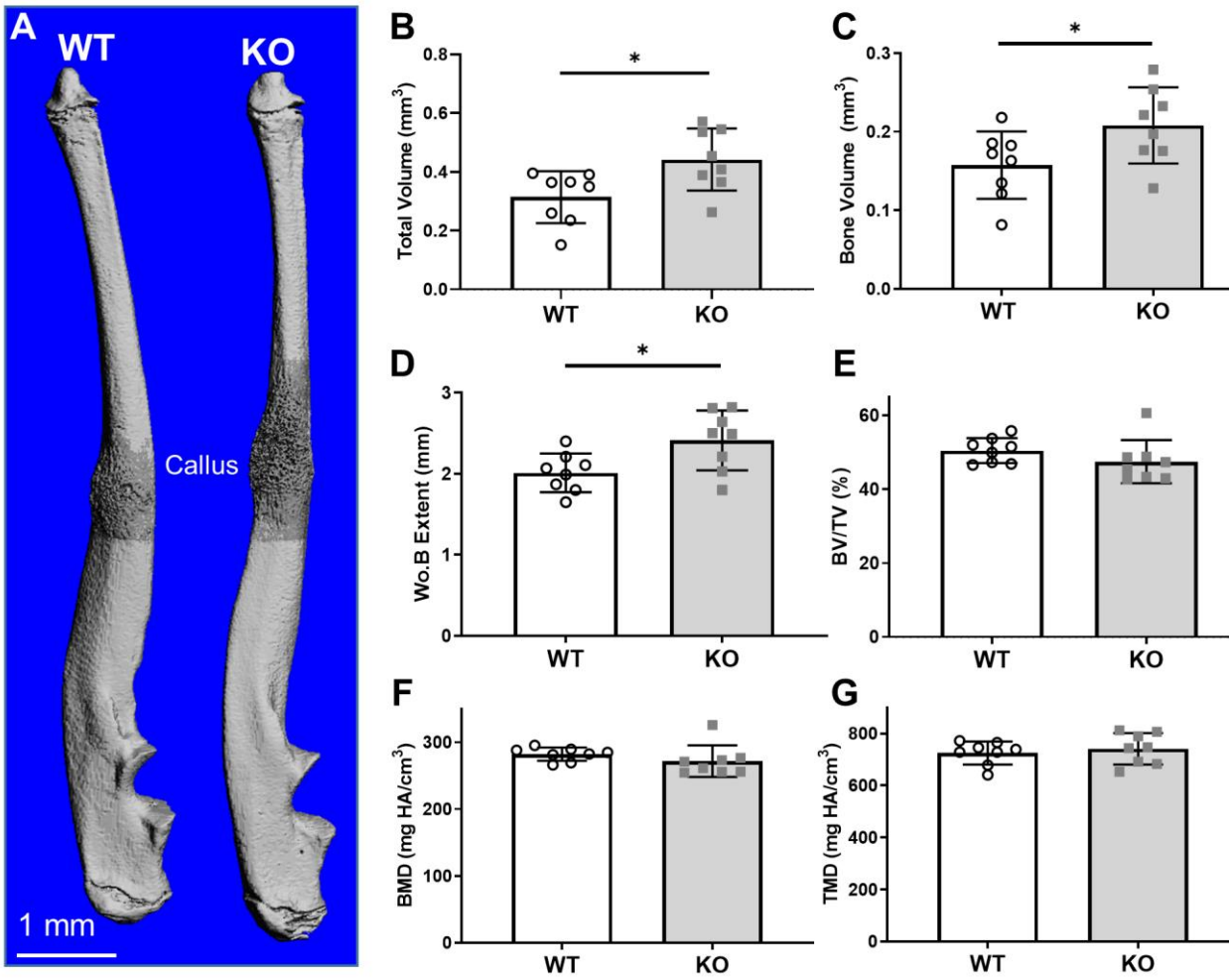

Figure 4.4: IL-6 KO increased stress fracture callus formation. Day 7 stress fracture callus was evaluated using microCT. Representative wildtype (WT) and IL-6 KO callus reconstructions are shown (A). Callus total volume (B), bone volume (C), and woven bone (Wo.B) extent (D) were all significantly increased in IL-6 KO animals. Bone volume fraction (BV/TV) (E), bone mineral density (BMD) (F), and tissue mineral density (TMD) (G) were not different between groups. Asterisk (*) denotes $p < 0.05$.

4.3.4 Global knockout of IL-6 does not alter immune cell recruitment in stress fracture repair

IL-6 has been reported to be a critical mediator of the innate immune system in response to injury. The transition from neutrophil recruitment to recruitment of macrophages is reliant upon IL-6 signaling [145,146]. Therefore, we wanted to investigate if IL-6 KO alters the balance of early responding immune cells in the stress fracture callus. To do so, we used immunohistochemistry (IHC) staining of day 1 and day 3 stress fracture callus for Gr-1, a marker of neutrophils, and F4/80, a marker of macrophages. IL-6 KO calluses had similar levels of Gr-1+ and F4/80+ cells at both day 1 and day 3 as did wild type calluses (Figure 4.5). Therefore, no imbalance of early responding immune cells is detected in IL-6 KO.

Two way ANOVA revealed a time effect on immune cell levels in stress fracture callus. Neutrophils had a significant increase in cell density from 1 to 3 days in the wild type animals ($p = 0.013$). IL-6 KO also had increased neutrophil levels, but failed to reach statistical significance ($p = 0.441$). Macrophage numbers increased from day 1 to day three in both wild type ($p = 0.081$) and KO animals ($p = 0.020$).

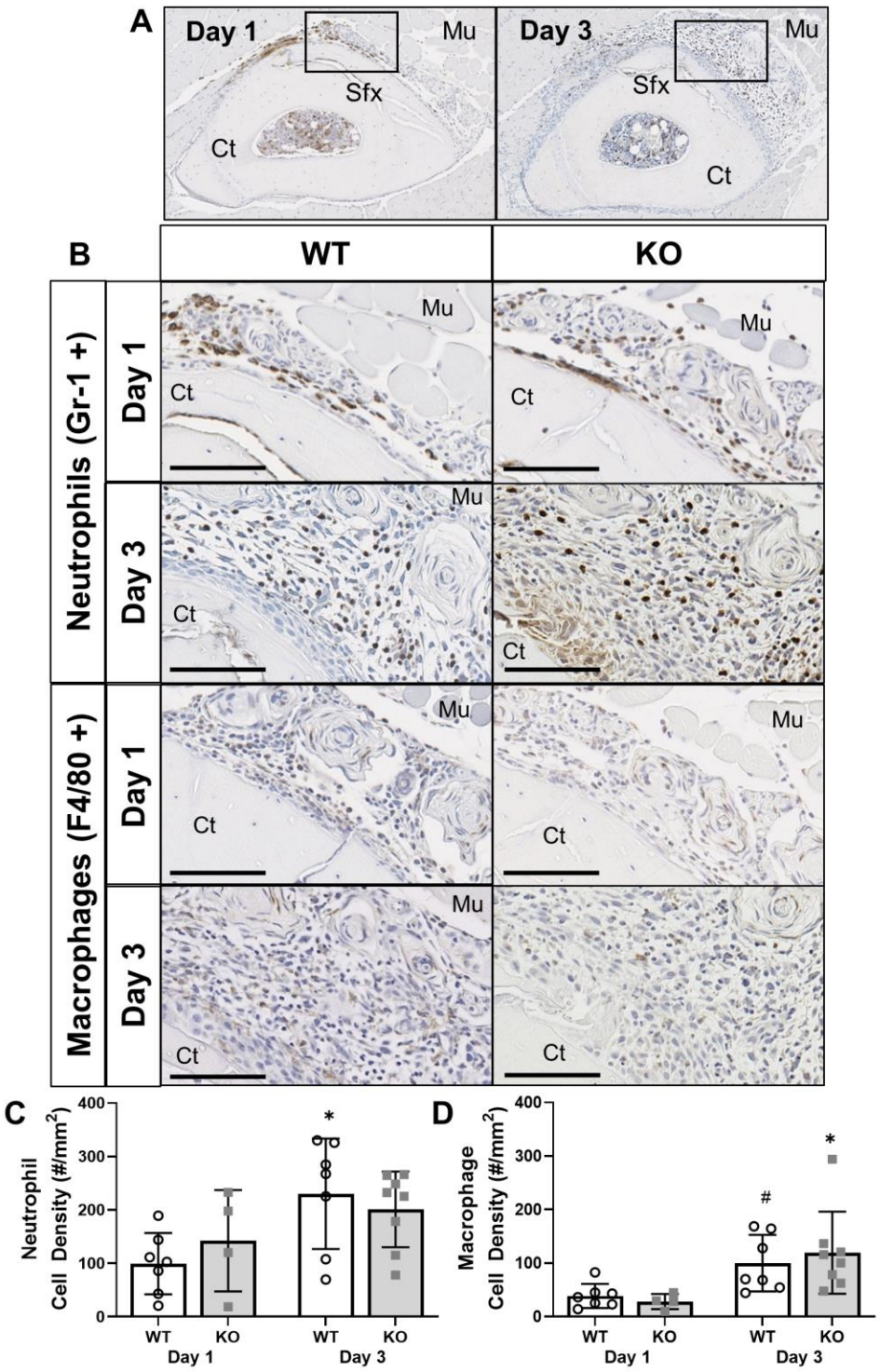

Figure 4.5: IL-6 KO did not alter immune cell recruitment after stress fracture. Day 1 and 3 stress fracture callus were evaluated using IHC for a neutrophil (Gr-1) and macrophage marker (F4/80). Representative images (A) demonstrate typical callus morphology at each time point including cortical bone (Ct), stress fracture crack (Sfx) and surrounding muscle (Mu). The black box represents general location of more magnified representative images (B) of callus shown for each genotype, time point, and antibody which demonstrate typical levels of staining. Quantification revealed no change in neutrophil (C) or macrophage (D) levels between genotypes. Scale bars are 100 μm length. * denotes $p < 0.05$ vs. day 1, # denotes $p < 0.1$ vs. day 1.

4.3.5 Global knockout of IL-6 decreases inflammatory and increases cell proliferation associated gene expression

We used RNA-seq to compare gene expression between IL-6 KO and wild type mice following stress fracture. Initial comparisons were conducted between day 1 and day 3 time points for IL-6 KO vs. wild type animals. However, no genes reached statistical significance (FDR < 0.05) to qualify as differentially expressed genes (DEGs) when comparing directly between genotypes.

Therefore, in order to make comparisons between genotypes, we generated lists of differentially expressed genes for each group against non-injured controls of the same genotype. We then made comparisons between those lists. The top DEGs for each time point and genotype reveal many similar genes that were most highly upregulated in both KO and WT animals (Table 4.2).

Venn diagrams were generated to show the number of shared and unique DEGs for each genotype at day 1 and day 3 time points (Figure 4.6 A). At 1 day, 546 DEGs were shared between the genotypes, while 461 DEGs were unique to wild type mice and 321 DEGs were unique to IL-6 KO. At day 3, there were 1769 genes were shared as DEGs, while 847 were unique to wild type and 725 were unique to IL-6 KO. The genes that were shared between genotypes were plotted according to their fold change (Figure 4.6 B). Genes such as *Reg3g* and *Wnt1* were more highly expressed in KO callus than WT callus, meanwhile Matn3 was more highly expressed in WT callus. Each genotype and time point were evaluated for enriched biological process gene ontology terms as compared to non-injured controls (Figure 4.6 C). Inflammatory processes such as “inflammatory response”, “immune response”, and “cytokine

production" were more highly enriched in wild type than IL-6 KO. Terms such as collagen organization, bone development, and ossification were also more highly enriched in wild type than knockout. Proliferation processes such as cell cycle, DNA replication, and cell division were more highly enriched in IL-6 KO than wild type.

In total, these data suggest a less pronounced inflammatory reaction in IL-6 KO mice following stress fracture. Furthermore, IL-6 KO has increased enrichment for proliferation related genes. Finally, a handful of genes such as *Wnt 1*, were more highly upregulated in KO callus.

Table 4.2: Top up- and down-regulated DEGs for each genotype and time point.

	WT D1		KO D1		WT D3		KO D3	
	Gene	Linear FC	Gene	Linear FC	Gene	Linear FC	Gene	Linear FC
Up-regulated	Il11	27.9	Reg3g	55.9	Matn3	76.8	Car12	36.0
	Reg3g	24.4	Il11	22.8	Car12	29.3	Reg3g	35.5
	Saa3	21.7	Saa3	12.7	Ptgs2	20.3	Panx3	31.9
	Cldn2	12.1	Wnt1	12.5	C1qtnf3	18.1	Steap1	21.8
	Ccl7	11.0	Ccl7	12.5	Panx3	17.8	Hapln4	17.8
	Ptgs2	10.5	Cldn2	11.4	Steap1	16.9	Mymk	17.3
	Il6	8.9	Steap1	9.2	Reg3g	13.9	Drd4	17.2
	Mt2	8.6	Ptgs2	9.2	Saa3	13.3	Ptgs2	15.4
	Ccl2	8.6	Cxcl1	9.2	Scn1a	13.2	C1qtnf3	14.8
	Timp1	7.5	Prg4	9.0	H2-Pb	12.4	C2cd4a	12.2
Down-regulated	Inmt	-8.9	Inmt	-8.1	Ankrd2	-9.0	Ighv5-16	-17.8
	Gkn3	-3.6	Dsp	-7.1	Dsp	-7.4	Dsp	-8.3
	Gsta3	-3.4	Nyap2	-3.7	Cidea	-6.9	Adrb3	-5.2
	Stmn4	-3.3	Krt75	-3.3	Cst6	-6.4	Dmkn	-4.9
	Col6a6	-3.2	Col25a1	-3.3	Fa2h	-6.0	Krt75	-4.9
	Crym	-3.2	Gm10115	-3.2	Cyp2e1	-5.6	Cidea	-4.7
	Fgf23	-3.1	Cdsn	-3.0	Gsta3	-5.6	Inmt	-4.5
	Sbk3	-3.0	Fa2h	-2.9	Adrb3	-5.3	Fgf23	-4.5
	Kera	-2.9	Cyp2e1	-2.9	Tmem179	-5.1	Cyp2e1	-4.5
	Gm29183	-2.8	Hpse2	-2.8	Cdsn	-5.1	Ighv1-39	-4.4

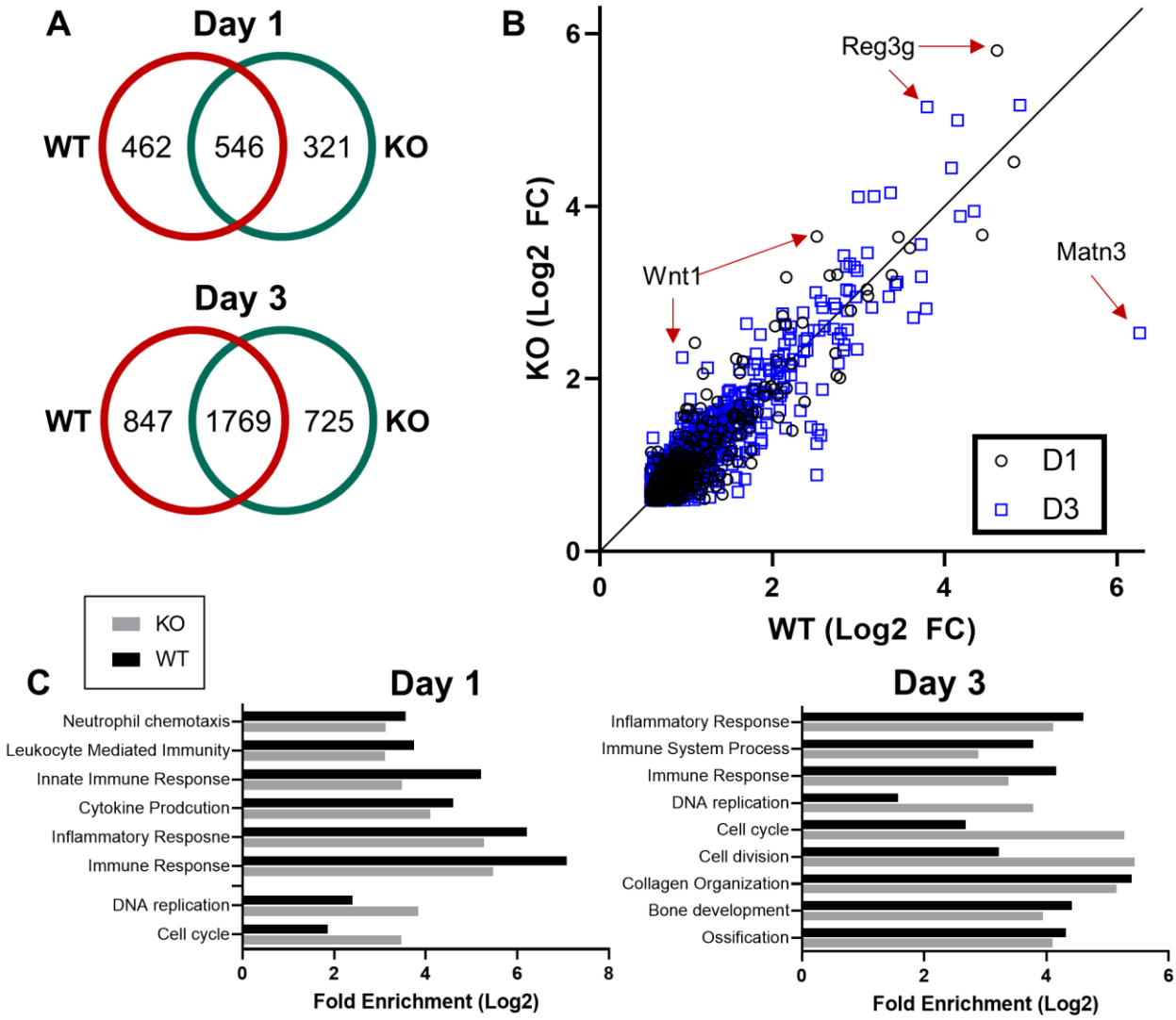

Figure 4.6: IL-6 KO had more proliferation and less inflammatory gene expression after stress fracture. Day 1 and 3 bulk tissue stress fracture callus was evaluated for gene expression using RNA-seq. Differentially expressed genes (DEGs) were found for each genotype and time point though comparison to uninjured control of same genotype. Comparisons of DEG lists at Day 1 and 3 reveal the largest number of DEGs are shared between genotypes, but many DEGs are unique to one genotype (A). DEGs that were shared by both genotypes were graphed by log2 fold change (FC) and reveal several genes which have greater increases expression in KO (B). Enriched biological process gene ontology terms were compared between genotypes (C). KO samples were more enriched for proliferative terms, while WT samples were more enriched for inflammatory terms and bone related terms.

4.3.6 Global knockout of IL-6 does not alter osteoclasts activity in stress fracture repair

IL-6 is reported to be important in osteoclast development. Therefore, we wanted to investigate the possibility that the increased bone in IL-6 KO callus was the result of decreased levels of bone resorbing osteoclasts. To assay this, we used TRAP staining on histology slices of day 7 stress fracture callus (Figure 4.7). Quantification of TRAP+ osteoclasts does not show any change in normalized osteoclast number (#/mm bone surface) or osteoclast surface fraction. Therefore, changes in osteoclast numbers are likely not the cause of increased bone formation after stress fracture.

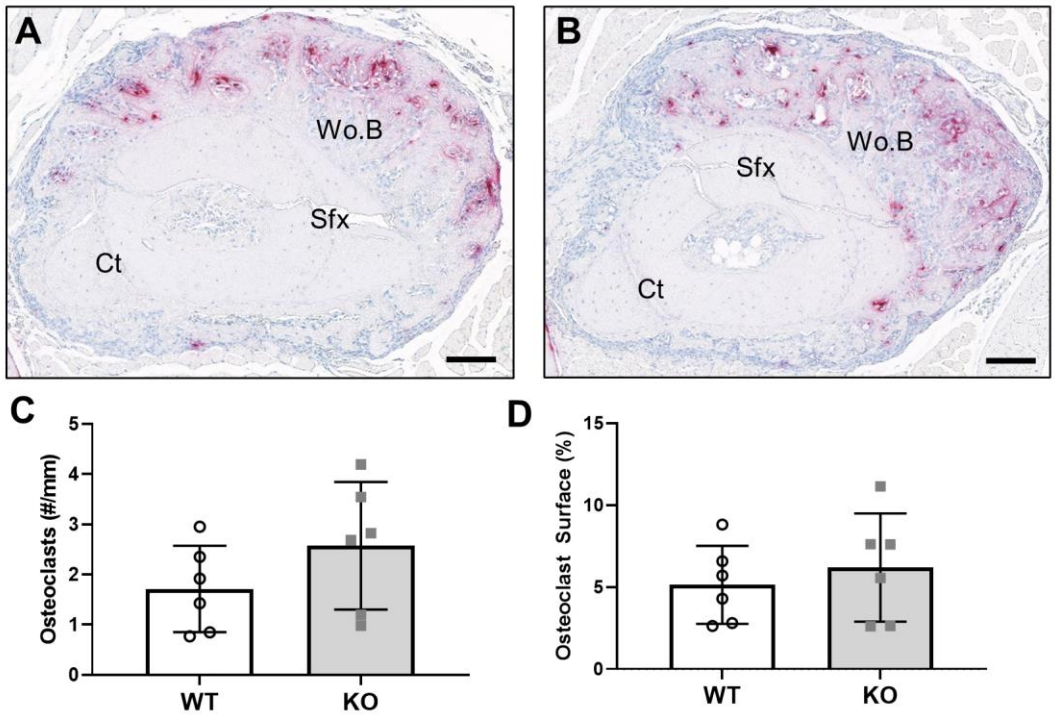

Figure 4.7: IL-6 KO does not alter osteoclast numbers in stress fracture callus. Day 7 stress fracture callus was evaluated using TRAP staining of histology sections to visualize osteoclasts. Representative images of a wild type callus (A) and IL-6 KO callus (B) demonstrate typical callus morphology including original cortical bone (Ct), stress fracture crack (Sfx), and callus woven bone (Wo.B). TRAP is visualized as pink staining and slides were counter stained with hematoxylin. Quantification revealed that normalized number of osteoclasts to bone surface (C) and osteoclast surface fraction (D) were consistent between genotypes. Scale bars are 100 μm in length.

4.3.7 Global knockout of IL-6 increases capacity for woven bone formation *in vivo*

Based on increased bone in stress fracture callus, we hypothesized that IL-6 KO may increase the ability of osteoblasts to produce new bone matrix. To test this idea, we employed a tibia model of anabolic loading in order to stimulate bone formation in the absence of an injury response. This allowed us to test the impact of IL-6 KO on osteoblast function, without the confounding factors of immune cell recruitment and release of inflammatory molecules associated with stress fracture repair.

Male and female IL-6 KO and wild type mice were all cyclically loaded to 8 N force for this experiment. Post-hoc strain gauge experiments revealed males (both KO and WT) reached tensile strain levels of approximately 1000 με, while females reached tensile strain levels of approximately 2000 με (Figure 4.8).

A 3-way ANOVA with factors of loading, sex, and genotype was performed on the primary three outcomes from dynamic histomorphometry (mineralizing surface, mineral apposition rate, and bone formation rate). Sex and Loading-Sex interaction were significant for all outcomes. Therefore, with these data in combination with the strain gage data, we determined to analyze male and female groups independently.

A

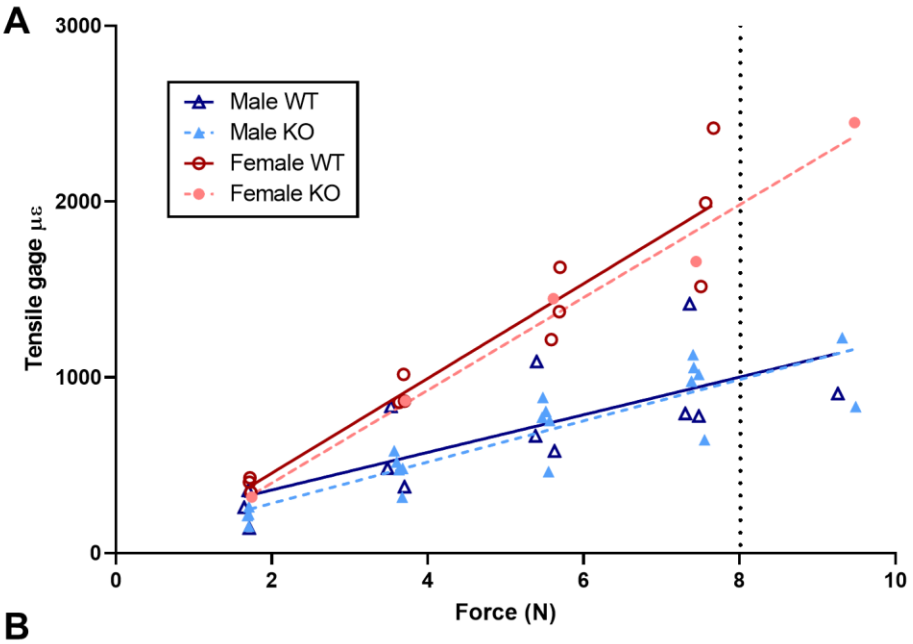

B

		WT	KO	Pooled
Male	Equation	$\varepsilon = 107.0 \times F + 146.1$	$\varepsilon = 117.3 \times F + 49.5$	$\varepsilon = 113.4 \times F + 86.1$
	r^2	0.5637	0.8059	0.7040
	Strain at 8 N	1002.1 με	987.9 με	993.3 με
Female	Equation	$\varepsilon = 269.5 \times F - 83.1$	$\varepsilon = 263.7 \times F - 127.5$	$\varepsilon = 264.7 \times F - 82.0$
	r^2	0.8993	0.9822	0.9276
	Strain at 8 N	2072.9 με	1982.1 με	2035.6 με

Figure 4.8: Post-hoc tibia strain gauging revealed males and females were loaded to different strains. 5 month old mice were used for strain gaging to assess the response of the mouse tibia to cyclic compression. Strain and force relationship (A) shows males and females reside on different lines, but genotypes within sex are closely related. Regression equations were calculated and estimated strain for male and female groups are shown (B),

Male animals were found to be loaded to a relatively low strain stimulus, which was capable of triggering modest lamellar bone formation (Figure 4.9 A). Mineralizing surface was non-significantly increased in the loaded limbs of male mice as compared to non-loaded controls, but no genotype difference was detected by 2-way ANOVA (Figure 4.9 B). Mineral apposition rate and bone formation rate were significantly increased in the loaded limbs of IL-6 KO males, but not wild type, as compared to non-loaded limbs. Knockout loaded limbs, though modestly greater, were not significantly different than wild type loaded limbs. Therefore, in bones stimulated with low strain, there was no significant difference in lamellar bone formation between IL-6 KO and wild type mice.

Female animals were loaded to a higher strain stimulus, capable of producing consistent lamellar bone formation and some limited woven bone formation (Figure 4.9 A). For both wild type and IL-6 KO mice, loaded bones had significantly greater mineralizing surface, mineral apposition rate, and bone formation rate than did non-loaded limbs (Figure 4.9 B). There was no genotype difference detected in mineralizing surface. But IL-6 KO animals had higher levels of mineral apposition rate and bone formation rate than did wild type animals. This was primarily driven by an increased capacity for knockout animals to form woven bone. Therefore, in bones stimulated with high strain, there was a significant increase in the ability of IL-6 KO animals to create bone, especially woven bone.

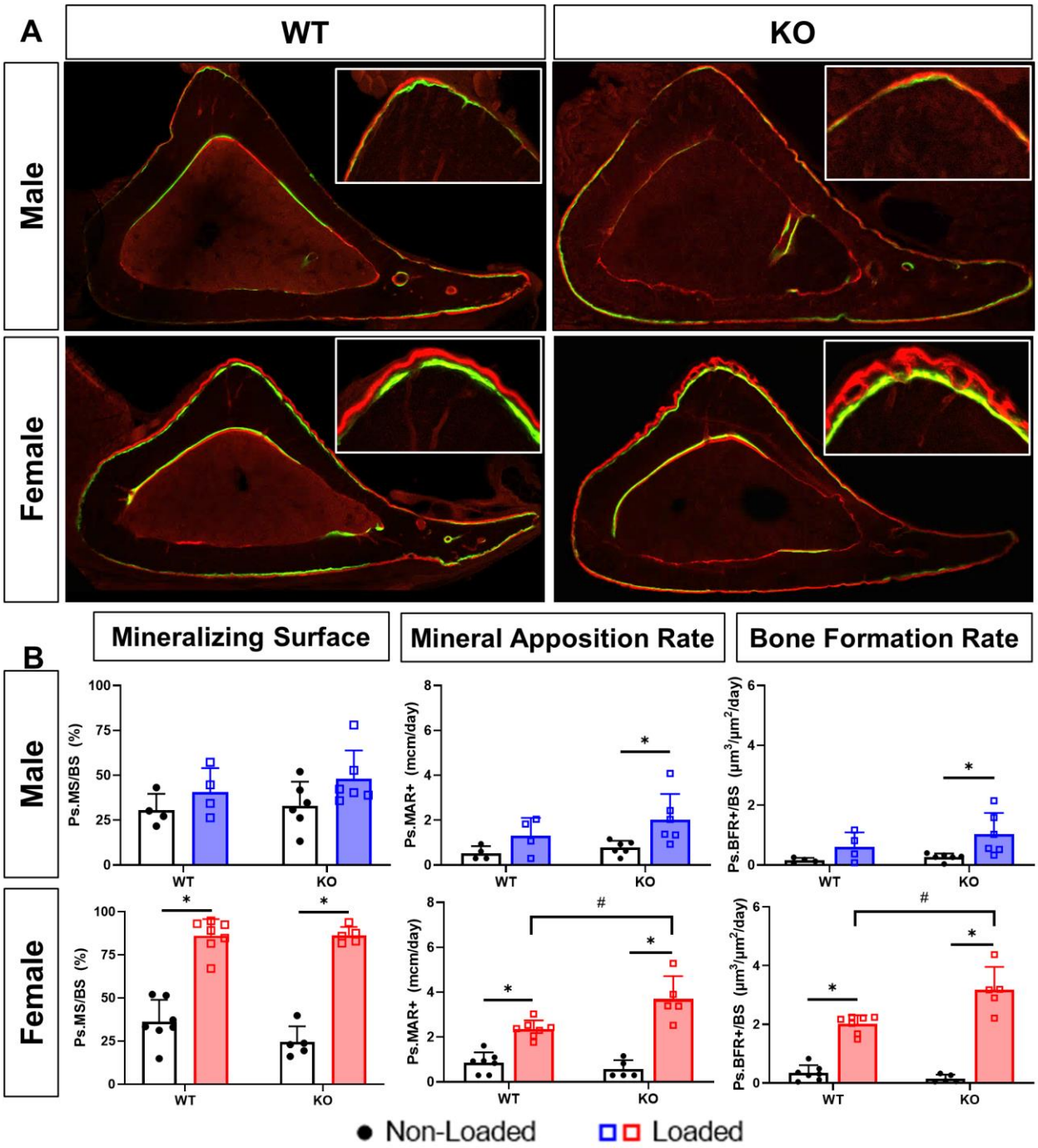

Figure 4.9: IL-6 KO mice have increased woven bone formation following anabolic loading. Tibia compression was used to stimulate loading induced bone formation in 5 month old IL-6 KO and WT mice. Representative images of each sex and genotype (A) demonstrate greater bone formation observed in female mice and greater woven bone formation in female KO mice. Dynamic histomorphometry using calcein and alizarin labels allowed quantification of bone formation parameters. In males, the only significant difference between non-loaded and loaded limbs was observed in knockout animals for mineral apposition rate and bone formation rate. For females significant increases were observed for each parameter and genotype between non-loaded and loaded limbs. KO mice also had significantly greater mineral apposition rate and bone formation rate as compared to wild type mice. * denotes $p < 0.05$ vs. non-loaded group, # denotes $p < 0.05$ vs. wild type loaded group.

4.3.8 Global knockout of IL-6 does not impact *in vitro* osteogenesis

We also examined the implications of IL-6 KO on osteoblasts using an *in vitro* culture model of osteogenesis. Because IL-6 KO mice had an increased capacity for bone formation following stress fracture and tibial loading, we hypothesized that IL-6 KO primary murine osteoblasts would have increased osteoblast differentiation and mineralization *in vitro*. IL-6 KO and wild type osteoblasts were collected from neonate pups and grown in culture. Upon addition of osteogenic media, staining for alkaline phosphatase was performed at day 7 and staining for alizarin red was performed at day 21 (Figure 4.10 A). Semi-quantitative analysis was performed using a plate reader for absorbance at 405 nm. IL-6 KO and wild type cells had similar levels of alkaline phosphatase and alizarin red staining (Figure 4.10 A). Therefore, the baseline performance of primary osteoblasts was comparable between IL-6 KO and wild type cultures.

We then investigated how IL-6 signaling impacted osteogenesis by dosing cells with exogenous IL-6 and its soluble receptor. Cells dosed with IL-6 only or IL-6 soluble receptor only had similar levels of alkaline phosphatase staining as vehicle dosed controls (Figure 4.10 B). However, cells dosed with the combination of IL-6 and soluble had significantly higher levels of alkaline phosphatase and alizarin red staining. Thus, IL-6 signaling appears to enhance *in vitro* osteogenesis in these culture conditions.

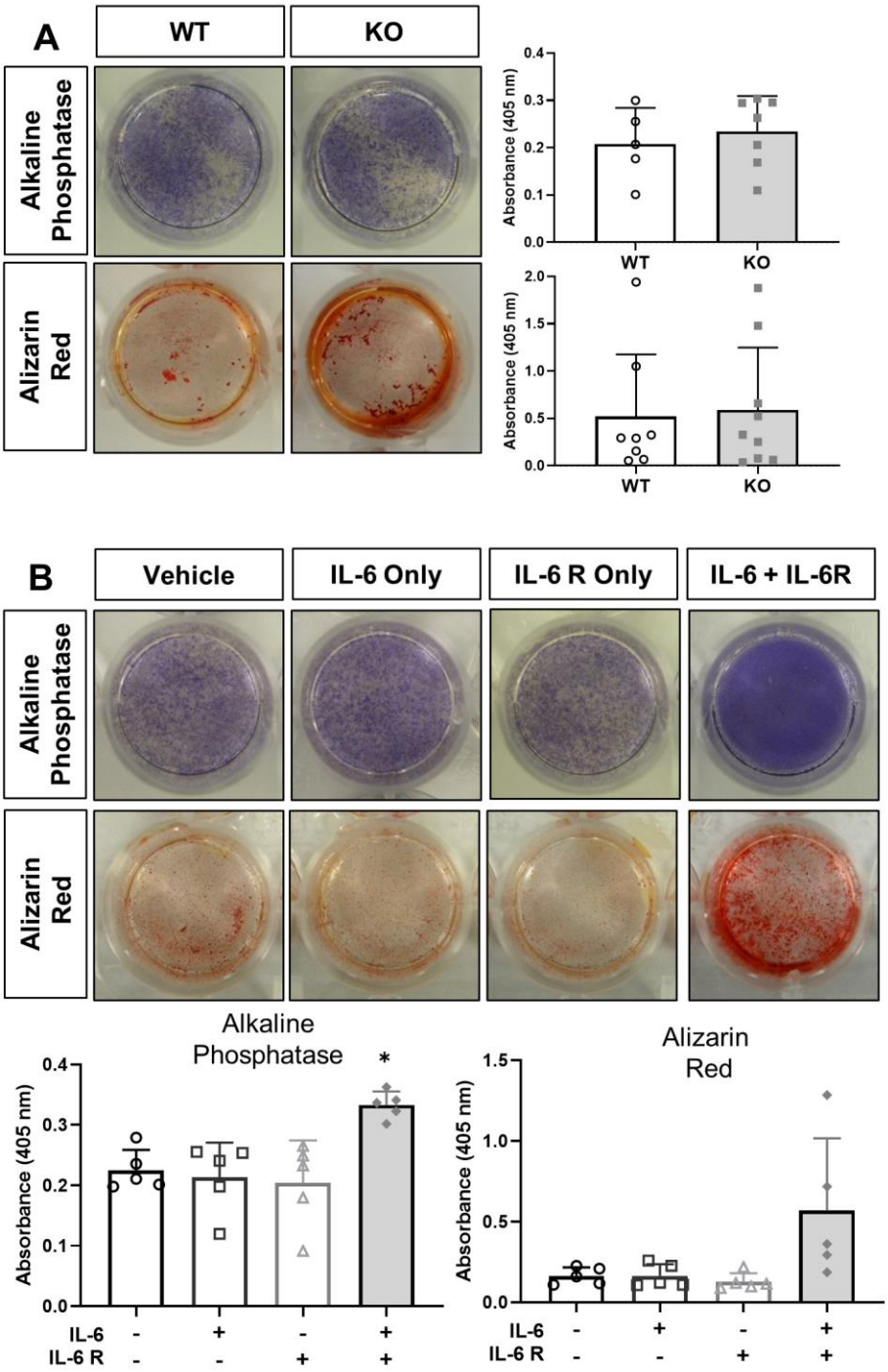

Figure 4.10: IL-6 KO does not impact in vitro osteogenesis. Calvarial osteoblasts were collected from wild type and IL-6 knockout mice and grown in culture. Following introduction of osteogenic media, alkaline phosphatase activity was measure at day 7 and alizarin red staining was measured at day 21. In baseline conditions, using only osteogenic media, no differences were detected in the alkaline phosphatase or alizarin red staining of WT or KO mice (A). A similar experiment was conducted with the continuous dosing of exogenous IL-6, IL-6 soluble receptor (IL-6 R), or a combination of the two (B). Neither IL-6 or IL-6 R alone altered alkaline phosphatase or alizarin red. But the combination of IL-6 and IL-6 R led to increased alkaline phosphatase and alizarin red staining. * denotes $p < 0.05$ vs vehicle group.

4.3.9 PCNA staining is unchanged in IL-6 KO stress fracture callus

We used staining for PCNA on slides of day 3 stress fracture callus to assess the proliferation of cells in IL-6 KO and wild type mice (Figure 4.11). Similar levels of PCNA positive cells were observed in the stress fracture callus of IL-6 KO and WT mice.

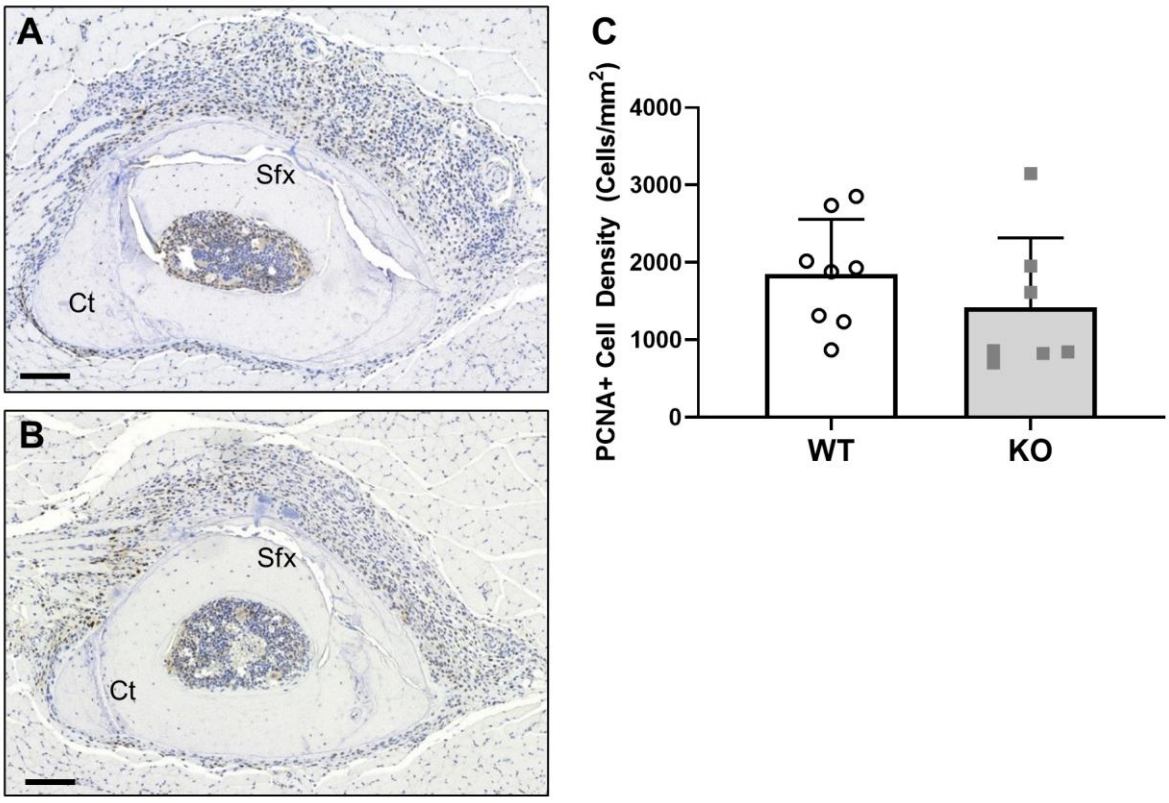

Figure 4.11: IL-6 KO does not alter PCNA staining following stress fracture. Day 3 stress fracture callus was evaluated for PCNA staining, a marker of cell proliferation, by IHC. Representative images of a WT (A) and KO (B) callus display typical staining intensities. Quantification of PCNA + cells (C) do not show any statistical difference between WT and KO callus. Scale bars are 100 um in length.

4.3.10 Condition deletion of IL-6 from osteoblasts or myeloid cells does not recapitulate the global knockout phenotype

In order to study the importance of IL-6 from different cell types, we generated conditional knockout mice which deleted IL-6 in the osteoblast lineage (Oc Cre) or the myeloid lineage (LysM Cre). Knockdown efficiency of these strains were assessed in two tissues of interest, bone marrow and cortical bone (Figure 4.12 A). Oc Cre driven deletion of IL6 had no effect on IL-6 expression in bone marrow, but expression of IL-6 in cortical bone was reduced by 67% ($p = 0.003$). LysM Cre significantly reduced IL-6 expression in bone marrow by 98% ($p = 0.008$), and also caused a non-significant reduction in cortical bone ($p = 0.186$). Cre mice for both strains were bred with Td tomato expressing Ai9 transgenes to confirm spatial expression of Cre activity (Figure 4.12 B). Oc Cre was widely expressed in osteocytes, endosteum, periosteum, and throughout the woven bone surface of stress fracture callus. LysM Cre had Td tomato expression in bone marrow as well as sparse expression throughout the stress fracture callus. Stress fractures were generated in these strains and bone formation was measured with microCT 7 days later. Neither total callus volume nor bone volume were different between Oc cKO or LysM cKO and their respective controls (Figure 4.12 C).

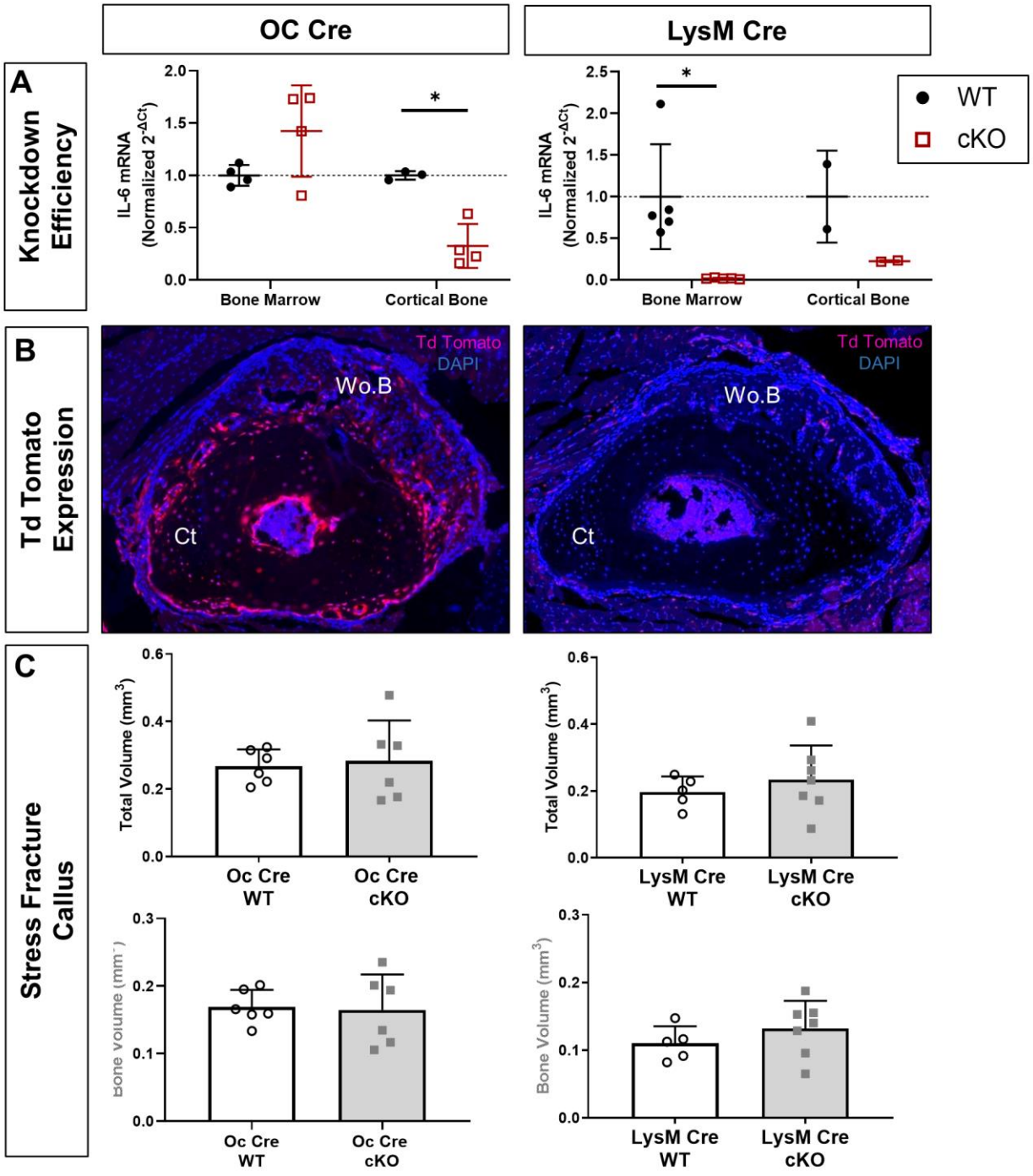

Figure 4.12: Conditional deletion of IL-6 with OC Cre or LysM Cre does not alter stress fracture callus formation. Deletion of IL-6 was assessed in two target tissues, bone marrow and cortical bone for both strains (A). OC Cre demonstrated 67% knockdown in cortical bone, while LysM Cre demonstrated 98% knockdown in bone marrow. Td tomato expression as observed by transverse histology of day 7 stress fracture callus shows OC cre driven expression throughout cortical bone and callus woven bone (B). LysM driven Td tomato expression was observed in the bone marrow and also sparsely throughout the callus (B). MicroCT was used to analyze stress fracture callus morphology at day 7 (C). Neither total callus volume nor bone volume were altered by conditional deletion of IL-6.

4.4 Discussion

Following skeletal injury, a crucial inflammatory phase is the first stage of successful repair. A component of this phase, IL-6 is highly upregulated following fracture. However, by what means IL-6 affects subsequent bone formation and fracture repair remains incompletely understood. Therefore, we sought to examine the role of *interleukin-6* (*IL-6*) in post-injury bone formation.

Following stress fracture, IL-6 KO mice were found to have enhanced capacity for bone formation. Specifically, IL-6 KO mice on average made 41% larger callus which contained 32% more bone (Figure 4.4). These calluses also extended further along the longitudinal length of the bone as did wild type callus. This represents an increased capacity for repair in IL-6 KO mice in response to stress fracture and suggests that IL-6 may be an inhibitor of intramembranous bone formation.

Due to the pleotropic nature of IL-6, a multitude of potential mechanisms were hypothesized for enhanced bone formation following stress fracture. Firstly, we postulated that IL-6 KO was directly altering the inflammatory phase of repair. This could be done through disruption of a balanced recruitment of important early responding immune cells, or through alterations in inflammatory signaling present in the early callus. Secondly, we speculated that IL-6 KO could impact the formation of the bone callus directly. This could be achieved by decreasing the effectiveness of osteoclasts to remodel and resorb newly formed bone or by enhancing the ability of osteoblasts to create new bone matrix. We explored each of these theories in subsequent experiments.

It has been reported that IL-6 is directly involved in the chemotaxis of early responding immune cells to sites of injury [146]. Therefore, we chose to analyze the levels of neutrophils and macrophages in the stress fracture callus of early time points (day 1 and day 3 post-injury). We used IHC of Gr-1 and F4/80, which are known markers for neutrophils and macrophages respectively. We did not observe any genotype driven differences in the level of Gr-1 or F4/80 positive cells in stress fracture callus (Figure 4.5). This indicates that there was no change in recruitment of neutrophils and macrophages due to IL-6 KO.

The release of inflammatory cytokines and the relay of inflammatory signaling cascades are important processes in the inflammatory phase. Knowing that IL-6 is a component of this phase, we hypothesized that gene expression could be altered in the callus of IL-6 KO mice. To examine this, we used RNA-seq to appraise gene expression in bulk callus tissue of day 1, day 3, and uninjured IL-6 KO or wild type mice. IL-6 KO did not result in drastic changes in gene expression in stress fracture callus. In fact, in direct comparisons between day 1 KO vs. WT callus, and day 3 KO vs. WT callus, no genes met statistical significance for differential expression (FDR < 0.05).

When comparing each genotype to its own respective non-injured control there was an abundance of differential gene expression (Table 4.2 & Figure 4.6). We were then able to make comparisons between the DEGs and enriched biological process gene ontology terms (BP GO terms) between these subsets. There was overlap between these DEG lists, but a sizable number of genes were DEGs for only one genotype. DEGs shared between WT and KO were plotted by fold change value. A handful of genes, including *Wnt1* and *Reg3g*, had greater upregulation in KO than WT at both day 1 and day 3. *Wnt1* is a potent bone anabolic agent and is associated with bone formation [160,161]. Regenerating family member 3 gamma (*Reg3g*) is a bactericide

with reported involvement in the regeneration of several tissues, however its role in fracture repair is not reported [162,163]. Higher upregulation of *Wnt1* and *Reg3g* could play a role in the greater bone formation observed in KO mice.

Enriched GO terms were also compared between genotypes. GO terms related to proliferation such as "*cell cycle*", "*DNA replication*", and "*cell division*" were more highly enriched in KO callus tissue. Proliferation is an important process in the production of woven bone [164]. An increase in proliferating osteoblasts could in part explain the increased woven bone produced in IL-6 KO mice following stress fracture. GO terms related to inflammation such as "*immune response*", "*inflammatory response*", "*cytokine production*", and "*innate immune response*" were more highly enriched in wild type callus tissue. This is suggestive of a slightly weakened inflammatory reaction to injury in IL-6 KO mice and may be representative of "missing IL-6 signaling" in these mice. It could be that this modest reduction in inflammation is a better precursor to bone formation than the wild type reaction and thus leads to greater bone formation.

IL-6 is known to stimulate osteoclast formation [148,149]. Therefore, it was hypothesized that IL-6 KO mice, in response to stress fracture callus formation, may have a decreased capacity to produce osteoclasts. Osteoclasts play an important role in reshaping callus as it forms and eventually in remodeling the fracture callus in the resolving phase of fracture repair. Although osteoclasts likely do not play an outsized role as early as day 7 – a time point when callus is still growing rapidly – it remains possible that a decrease in osteoclasts could in fact lead to an increase in bone present in callus. To assess osteoclast numbers, we used TRAP staining on histology of day 7 stress fracture callus (Figure 4.7). We did not observe a change in either osteoclast number or osteoclast surface per bone surface in the woven bone of stress fracture

callus in IL-6 KO mice. Therefore, it is unlikely changes in osteoclast formation are responsible for the increased callus and bone in IL-6 KO mice.

It was also a possibility that IL-6 has a direct impact on osteoblasts in stress fracture repair. Therefore, we hypothesized that IL-6 KO rendered osteoblasts more capable of producing bone matrix than wild type osteoblasts. To examine this, we employed both *in vivo* and *in vitro* experiments.

To examine the impact of IL-6 KO on osteoblasts *in vivo*, we chose to employ a tibia compression model of loading induced bone formation. This model allowed us to examine how osteoblasts respond when challenged with a loading stimulus, but without the confounding factors of injury induced inflammation. Thus, using this model, we hoped to gain an understanding of how IL-6 directly impacts osteoblast function. Males and females were both loading to an 8 N stimulus for these experiments. Strain gaging was performed subsequent to bone formation experiments, and although there were no genotype driven differences in strain response, it was revealed that males and females had very different strain responses to the 8 N stimulus (Figure 4.8). We estimated that Females experienced ~2000 με at the 8 N force stimulus, while, males experienced ~1000 με at 8 N force. Due to this different strain response to loading – females and males were analyzed separately as a high and low stimulus group respectively.

Dynamic histomorphometry was used to observe and quantify loading induced bone formation. Male mice, which received a "low" stimulus had a modest response to loading (Figure 4.9). Mineralizing surface, mineral apposition rate, and bone formation rate were increased with loading in both genotypes. However, only mineral apposition rate and bone formation rate in

knockout animals reached significance over non-loaded controls. IL-6 KO and WT loaded limbs were not significantly different for males. Female mice received a “high” stimulus and had a significant response to loading for both genotypes for mineralizing surface, mineral apposition rate, and bone formation rate (Figure 4.9). Furthermore, among loaded limbs, IL-6 KO had significantly higher mineral apposition rate and bone formation rate than did wild type animals. This increased response was mostly due to an increased propensity for woven bone formation in IL-6 KO mice. In fact, if mineral apposition rate and bone formation rate are calculated using only lamellar bone, and not adjusted to include woven bone, the difference between WT and KO becomes non-significant. Four samples of the 5 KO samples experienced woven bone formation while only one of the five WT samples had woven bone formation. Taken together, these data suggest that IL-6 KO mice are more capable of woven bone formation. This is complimentary to the increased bone formation observed in stress fracture callus, where bone formation is primarily woven bone. Meanwhile, IL-6 KO does not appear to impact lamellar bone formation, as observed in the male cohort. This is complimentary of the baseline skeletal phenotyping which indicates IL-6 KO mice have normal bone parameters.

To examine how IL-6 KO affects osteoblasts *in vitro* we used a culture model of osteogenesis with calvarial osteoblasts from IL-6 KO and WT mice. We measured two relevant outcomes for osteoblast function, alkaline phosphatase staining – an early marker for osteoblast differentiation, and alizarin red staining – a marker for matrix production and mineralization which characterizes osteoblast function. Osteogenic media was used to induce *in vitro* osteogenesis in these cells. The baseline ability osteogenesis of IL-6 KO was not different from WT cells (Figure 4.10 A). KO cells displayed equivalent levels of alkaline phosphatase and alizarin red staining as did control cells. These data paralleled data showing *in vivo* skeletal

development was not impacted by IL-6 KO. Therefore, we wanted to challenge these cells with some inflammatory stimulus which might better recapitulate what is experienced by osteoblasts in response to stress fracture. To do this, we turned to a model of exogenous IL-6 signaling in our *in vitro* osteogenesis system. We hypothesized that if IL-6 KO was advantageous to bone formation (as observed post-stress fracture and tibial loading) then it stood to reason that adding IL-6 to osteoblast cultures would have the opposite effect and would be deleterious to osteogenesis. To test this, we dosed wild type cell cultures with IL-6, IL-6 soluble receptor, or a combination of the two. We observed increased alkaline phosphatase and alizarin red staining in cells treated with the combination of IL-6 and soluble receptor (Figure 4.10 B). This represents an increased capacity for *in vitro* osteogenesis in the presence of IL-6 trans-signaling and was contrary to our hypothesis.

Reports in the literature on the impact of IL-6 on osteoblasts contain many conflicting reports. IL-6 has been demonstrated to both decrease osteoblast function [150–152] and increase osteoblast function [153]. These data in combination with our *in vitro* studies suggest the implications of IL-6 for osteoblasts are highly context dependent. It is unlikely that *in vitro* osteogenesis through osteogenic media induction closely matches the *in vivo* context of stress fracture repair. Therefore, while an intriguing complimentary experiment, these data likely do not shed much light on post-injury bone formation.

Proliferation is an important process for woven bone formation [164]. Increased woven bone in IL-6 KO mice formation following stress fracture and tibia loading could in part be explained by increased proliferation of osteoblasts. Furthermore, gene expression in early stress fracture callus revealed IL-6 KO mice having increased enrichment for proliferation related gene ontology terms (Figure 4.6). Therefore, we wanted to examine cell proliferation in response to stress

fracture in IL-6 KO mice. To do this, we used IHC staining for PCNA on day 3 stress fracture callus (Figure 4.11). However, quantification of PCNA + cells in stress fracture callus does not indicate any difference in proliferation exists between WT and IL-6 KO callus.

We observed differing phenotypes for IL-6 KO mice in response to full fracture and stress fracture. Through microCT evaluation of day 14 full fracture callus, no differences were observed between IL-6 KO and wild type callus (Figure 4.3). This suggests that IL-6 may act in different manners in endochondral versus intramembranous bone formation. It should be noted that this was an evaluation of only one time point, and effects of IL-6 KO could possibly impact different stages of full fracture repair that we didn't assay.

Knowing that IL-6 KO is capable of increased bone formation in stress fracture callus, we wanted to know what the cellular source of IL-6 was in response to injury. Are bone cells the master regulators of bone fracture repair, or are infiltrating immune cells or other cell sources responsible for initiating successful repair. In an attempt to answer this question, we generated two conditional deletion (cKO) mouse strains. Oc Cre mice were used to delete IL-6 from mature osteoblasts and osteocytes and LysM Cre was used to delete IL-6 from myeloid derived cells such as neutrophils and macrophages. Neither strain of cKO mice recapitulated the increased bone formation observed in the global knockout mice. Many possible explanations exists for why this occurred. Firstly, IL-6 could be supplied by a combination of various cells types which could compensate when one source is depleted. Secondly, it is possible neither of our cell population targets is a critical source of IL-6 post-stress fracture and an untested population could be involved. Osteoblast precursor cells, which are not yet Oc +, could fit this role and Osx Cre could have been used to assess. Lastly, we could have targeted the correct cell populations, but did not achieve great enough deletion efficiency to recapitulate the phenotype. Whichever of

these possibilities hold true, the cell population which produces IL-6 following skeletal injury remains unknown.

Yang and colleges were the first to study fracture repair in IL-6 KO mice [34]. They reported that 2 weeks following a full fracture, KO mice had reduced mineralization in callus tissue and that KO callus had increased cartilage content. These differences disappeared by the 4 week time point. Therefore, Yang et al. report that IL-6 deletion delays fracture repair [34]. A subsequent report by Wallace et al. reported that at 2 week following a tibia full fracture, IL-6 KO had reduced callus strength [35]. Together, these reports paint a picture of delayed bone healing in IL-6 KO mice. However, in our model of full fracture repair we did not detect any change in callus morphology for IL-6 KO mice at a two week time point.

A few other reports have studied the role of IL-6 in fracture repair using pharmacological approaches. Prystaz et. al report that inhibition of IL-6 classical signaling through antibody injections results in delayed fracture healing. However, Kaiser et al., in a model of polytrauma and fracture, reported that inhibition of IL-6 trans signaling improved healing outcomes. Therefore, in it appears that the impact that IL-6 has in fracture repair is very context dependent. The age of the animal, the particulars of the injury, the method of ossification, and complications such as polytrauma can all provide varied results for IL-6 inhibition in fracture repair.

4.5 Conclusions

Herein, we report that IL-6 KO enhances bone formation in a stress fracture model of intramembranous ossification. IL-6 KO mice produced larger stress fracture calluses which contained more bone than control mice. There was no change in the recruitment of neutrophils or macrophages nor was there a change in osteoclast numbers in IL-6 KO stress fracture callus. IL-6 KO resulted in slight changes in gene expression following injury, with increased enrichment in cell proliferation gene ontology terms and decreased inflammatory terms. IL-6 KO also had greater fold changes in the bone anabolic gene *Wnt1*. A model for loading-induced bone formation revealed that osteoblast ability to produce woven bone was enhanced in IL-6 KO mice in the absence of injury.

In total, we have found that IL-6 KO mice have greater bone formation in response to stress fractures, through increased proliferation gene expression, decreased inflammatory gene expression, and an enhanced capacity for osteoblast driven woven bone creation.

Chapter 5: Cxcr2 deficiency decreases intramembranous osteogenesis following stress fracture

5.1 Introduction

Inflammation is a critical process for successful skeletal repair following injury. This inflammatory stage of repair is tightly controlled in both extent and time course [10,11]. An inflammatory reaction which is too great can be detrimental to healing. This has been shown clinically in reports of hyper-inflammation in patients with polytrauma [12,13], obesity [14], or diabetes [15,16]. On the other hand, an inflammatory reaction which is insufficiently strong will also lead to sub-optimal repair. This has been reported clinically in patients with HIV [17] and those treated with NSAID drugs [18–20]. Therefore, a high clinical importance exists for a thorough understanding of the inflammatory phase of fracture healing and how it facilitates a successful repair cascade.

Previous data from our lab have shown that the CXC family of chemokines are among the most highly upregulated genes following skeletal injury [28]. Despite their abundance in the inflammatory phase of repair, little is known about the role these ligands may play in successful repair.

The CXC chemokines most upregulated following skeletal injury (*Cxcl1*, *Cxcl2*, *Cxcl3*, and *Cxcl5*) all signal through CXC receptor 2 (*Cxcr2*). These chemokines are reported to mediate the recruitment of neutrophils from the bone marrow to circulation in order to respond to injured

tissue [115]. CXC signaling through CXCR2 is also involved in recruitment of endothelial cells as a mediator of angiogenesis [116]. Because of the importance of neutrophil recruitment [165] and angiogenesis [166,167] for successful fracture repair, it is possible that CXC signaling in early fracture callus acts through one of these two mechanisms to facilitate successful repair.

Herein, we examine the role of CXC family receptor 2 (*Cxcr2*) in post-injury bone formation through the use of transgenic mice and two models of skeletal fracture. We hypothesize that knockout of *Cxcr2* will impair fracture repair through either reduced neutrophil recruitment and/or reduced angiogenesis.

5.2 Methods

5.2.1 Mice

All mouse studies were conducted under guidance of a Washington University IACUC approved protocol. A total of 73 mice were used in this study. All mice were housed in 12:12 light/dark conditions, given water and food ad libitum. All mice were 12 weeks of age at time of use and males and females were both used in these experiments. In order to study the impact of CXC family signaling in bone regeneration we chose to target the knockout of CXC receptor 2 (*Cxcr2*), the common receptor for the CXC ligands upregulated in response to fracture. We obtained *Cxcr2* global knockout mice (Cxcr2 KO; gift from D. Link) [115] to test effects of global knockout compared to wild type littermate controls. Cxcr2 KO and littermate wild type controls were generated using breeders that were heterozygous for the Cxcr2 KO transgene.

In order to examine if CXC signaling through immune cells is important in fracture repair, we conditionally deleted Cxcr2 in myeloid derived cells by crossing the LysM Cre mouse (Jackson Labs #004781) [168] to the Cxcr2 floxed mouse (Jackson Labs #024638) [169]. LysM $Cre^{+/+}$;$Cxcr2^{fl/fl}$ mice were used as experimental animals (LysM cKO) and were compared to littermate LysM $Cre^{+/+}$;$Cxcr2^{+/+}$ control mice (LysM control). Experimental animals were generated through the paired breeding of mice heterozygous for Cxcr2 floxed transgene (LysM $Cre^{+/+}$;$Cxcr2^{+/fl}$). All mice were on a C57BL/6J background.

5.2.2 Full Fracture

Full fractures were created in the femur mid-diaphysis of mice (N = 43). Detailed methodology for this procedure has been previously reported [44]. In brief, mice were kept under anesthesia (isoflurane 1-3%) throughout the procedure. The right femur was exposed through an incision and notched with a scalpel blade to predispose the mid-diaphysis to fracture. The right hind limb was then secured in a custom fixture on a hydraulic material testing machine (Instron Dynamite). A displacement controlled ramp (30 mm/s) was used to initiate three-point bending of the femur to achieve fracture. The broken femur was then stabilized by insertion of a 24 G pin inserted into the intramedullary space and the incision was closed. The left femur served as an uninjured contralateral control. X-ray radiographs were taken at time of injury to ensure a break at the mid-diaphysis and proper pin placement. Mice were then administered buprenorphine SR (1 mg/kg, s.c.) and returned to their cages with unrestricted activity for 14 days until sacrifice.

5.2.3 Stress Fracture

Stress fracture were created in the ulna diaphysis of mice (N = 30). Cyclic loading for stress fracture creation has been thoroughly detailed in previous reports [88,89]. Briefly, while anesthetized (Isoflurane 1-3%) the right forearm of the mouse is secured at the wrist and elbow in custom fixtures on a hydraulic material testing machine (Instron Dynamite). Force controlled cyclic loading at 2 Hz is performed until reaching a desired displacement at which a stress fracture has formed. Loading parameters for each strain were determined using a set of calibration animals to determine ultimate force of the forelimb and cyclic displacement to complete fracture of the ulna and are listed in Table 5.1. The left ulna served as a contralateral control. Mice were then administered buprenorphine (0.1 mg/kg, s.c.) and returned to unrestricted cage activity until sacrifice.

Table 5.1: Stress fracture calibration data for Cxcr2 mouse strains.

Strain	Ultimate Force (N)	Cyclic Loading Force (N)	Displacement to Fracture (mm)	Cyclic Stopping Displacement (mm)
Cxcr2 KO (n = 8)	3.9 ± 0.4	2.9	1.13 ± 0.15	0.56
LysM cKO (n = 9)	4.4 ± 0.3	3.3	1.10 ± 0.36	0.55

5.2.4 MicroCT

In order to evaluate baseline differences in the skeleton of wild type and Cxcr2 KO mice, intact femurs were collected and scanned using microCT (Scanco VivaCT). Femurs were scanned in air, with energy of 55 kVp, intensity of 145 μA, integration time of 300 ms, and voxel size of 10.5 μm. Analysis of cortical bone was performed on 100 slices centered on the midpoint of the femur length. Analysis of cancellous bone was performed on 100 slices in the distal femur beginning proximal to the growth plate. Due to the smaller body size of Cxcr2 KO animals, measurements were adjusted for body size using the linear regression method [170].

Similar approaches were used to evaluate fracture callus following full fracture or stress fracture. For full fracture, femurs were dissected and scanned using same parameters as intact femur scanning. Full fracture callus was analyzed for 600 slices centered on the fracture location. For stress fracture, ulna were dissected and scanned using a Scanco MicroCT40 system in 3% agarose, with energy of 70 kVp, intensity of 114 μA, integration time of 300 ms, and voxel size of 10 μm. Stress fracture callus was analyzed for the entire length of the callus.

5.2.5 Histology

Injured limbs were dissected and fixed for 24 hours in 10% buffered formalin. Injured bones were then demineralized by EDTA 14% for 14 days. Samples were then embedded in paraffin and sectioned at 5 μm transverse sections. Immunohistochemistry staining was performed using an antibody for the neutrophil marker Gr-1 (Bio-Rad MCA2387T) at a concentration of 1:500 and an ImmPRESS reagent anti-rat kit (Vector Labs MP-7444). Slides were then imaged on a slide scanner (Hamamatsu Nanozoomer) at 20X magnification. Quantification of stained cells was performed with Bioquant software.

5.2.6 Deletion efficiency validation with qPCR

In order to test the knockdown efficiency of LysM cKO mice, bone marrow was collected from left tibia of LysM cKO and LysM control mice, submerged in TRIzol, and stored at -80 C. To extract RNA, TRIzol/sample solutions were processed with an RNA clean-up and concentration kit (Norgen Biotek). cDNA was then produced (Bio-Rad iScript) using 500 ng of RNA from each sample. qRT-PCR was performed (Applied Biosystems StepOnePlus) using primers for *Cxcr2* (IDT, F: AGC AAA CAC CTC TAC TAC CCT CTA, R: GGG CTG CAT CAA TTC AAA TAC CA), and reference genes *Tbp* (IDT, Mm. PT. 39a. 22214839) and *Ipo8* (IDT, Mm. PT. 39a. 22214844). Expression was normalized to reference genes and $2^{-\Delta Ct}$ expression values are reported.

5.3 Results

5.3.1 Cxcr2 KO mice have smaller body size but comparable skeletons to wild types

Cxcr2 knockout mice had smaller body weights than wild type control mice (Figure 5.1). A 2-way ANOVA of the cancellous and cortical bone parameters revealed significant genotype effects for most parameters, with Cxcr2 KO having less bone than controls (Table 5.2). However, due to significantly decreased body weight in Cxcr2 KO animals, skeletal measurements were adjusted to account for body weight using the linear regression method [170]. After body weight adjustments, genotype effects were only observed in a handful of parameters (Table 5.2). Therefore, after accounting for reduced body size, Cxcr2 KO animals develop normal skeletons.

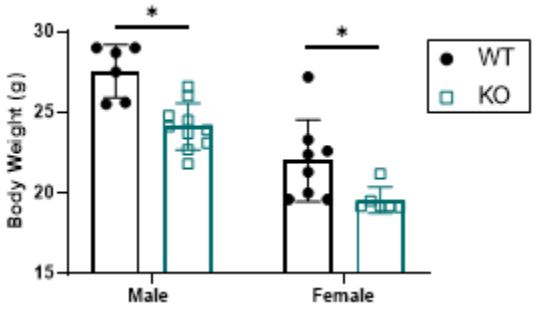

Figure 5.1: Cxcr2 mice have lower body weights than wild type contols. Body weights were measured at 12 weeks of age prior to injury. Asterisk (*) denotes $p < 0.05$

Table 5.2: Body weight adjusted values for MicroCT evaluation of baseline skeleton in Cxcr2 KO mice

		Non-Adjusted			Body Weight Adjusted		
		WT	**KO**	**Sig**	**WT**	**KO**	**Sig**
Cancellous							
	BV/TV	24.8 ± 14.5	18.9 ± 7.7	*	21.0 ± 6.7	21.1 ± 4.5	ns
	BMD	169.7 ± 87.8	130.1 ± 51.6	*	146.8 ± 41.2	145.4 ± 28.5	ns
	Tb.N	8.3 ± 3.2	6.9 ± 2.2	*	7.4 ± 1.2	7.6 ± 1.1	ns
	Tb.Th	0.057 ± 0.009	0.052 ± 0.005	*	0.055 ± 0.006	0.053 ± 0.005	ns
	Tb.Sp	0.14 ± 0.05	0.17 ± 0.05	*	0.16 ± 0.02	0.15 ± 0.03	ns
Cortical							
	Ct.Th	0.20 ± 0.02	0.18 ± 0.02	*	0.19 ± 0.01	0.18 ± 0.01	*
	TMD	1022.8 ± 28.6	992.1 ± 62.0	*	1024.1 ± 28.2	1002.8 ± 54.2	ns
	T.Ar	1.87 ± 0.32	1.86 ± 0.12	ns	1.78 ± 0.11	1.89 ± 0.09	*
	B.Ar	0.89 ± 0.18	0.80 ± 0.10	*	0.84 ± 0.06	0.83 ± 0.05	ns
	M.Ar	0.98 ± 0.15	1.05 ± 0.08	ns	0.94 ± 0.06	1.06 ± 0.08	*
	pMOI	0.45 ± 0.17	0.40 ± 0.07	ns	0.40 ± 0.06	0.42 ± 0.04	ns

Values represent group mean with standard deviation. Asterisk (*) denotes $p < 0.05$ genotype effect by 2-way ANOVA.

5.3.2 Cxcr2 knockout does not impair endochondral ossification following full fracture

Mice were subjected to full femur fractures and sacrificed following 14 days to observe post-injury bone formation. MicroCT was used to analyze callus and bone formation (Figure 5.2). No significant changes were observed between wild type and Cxcr2 KO mice. Total callus volume, bone volume, callus bone volume fraction (BV/TV), callus tissue mineral density (TMD), and callus BMD were all consistent between wild type and knockout mice (Figure 5.2B-F). Cxcr2 knockout mice produce equivalent callus and bone formation following full fracture.

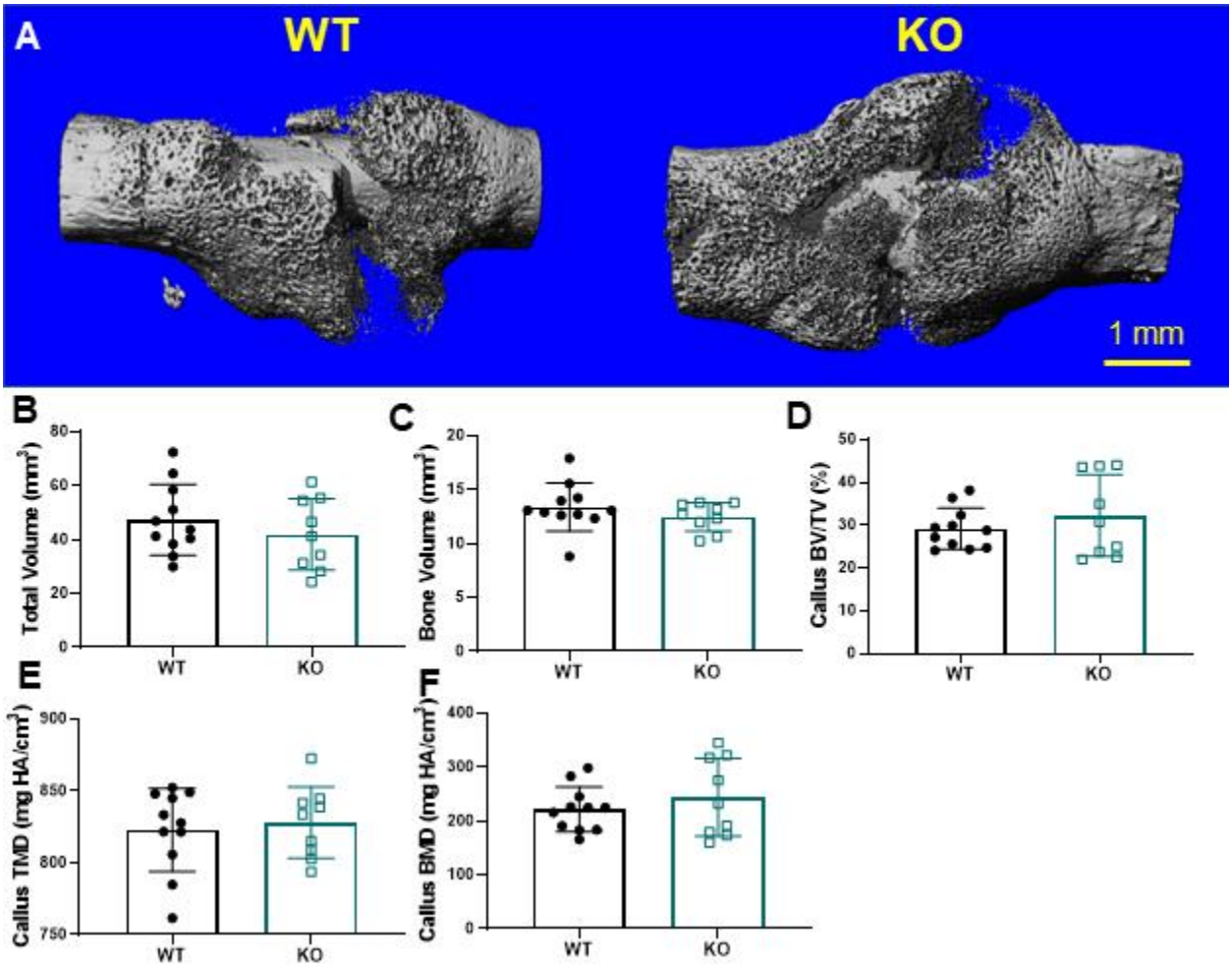

Figure 5.2: Cxcr2 knockout mice have normal full fracture callus formation. Full fractures were examined using microCT at day 14 post-injury. 3D reconstructions of samples with median callus volume are depicted for each group (A). Parameters such as total callus volume (B), callus bone volume (C), callus bone volume fraction (BV/TV) (D), callus tissue mineral density (TMD) (E), and callus bone mineral density (BMD) (F) were measured. No significant differences were detected in these parameters between wildtype and Cxcr2 knockout mice.

5.3.3 Cxcr2 knockout impair intramembranous ossification following stress fracture

Mice were sacrificed 7 days after ulna stress fractures and microCT was used to visualize callus and bone formation (Figure 5.3). Crack extent was consistent between wild type and knockout mice (Figure 5.3 B), representing equivalent damage burden produced by the model. Woven bone (Wo.B) extent (Figure 5.3 C), measured as the longitudinal length of woven bone callus, was also consistent between genotypes. The total callus volume and callus bone volume were significantly reduced in knockout mice (Figure 5.3 D & E). Callus bone fraction (BV/TV) was significantly increased in Cxcr2 KO mice (Figure 5.3 F). Callus bone mineral density (BMD) was unchanged, but callus tissue mineral density (TMD) was significantly reduced in knockout mice (Figure 5.3 G & H), suggesting that the bone in the callus was less mineralized in knockouts. Cxcr2 knockout mice respond to stress fracture with reduced production of callus and bone formation as compared to wild type controls.

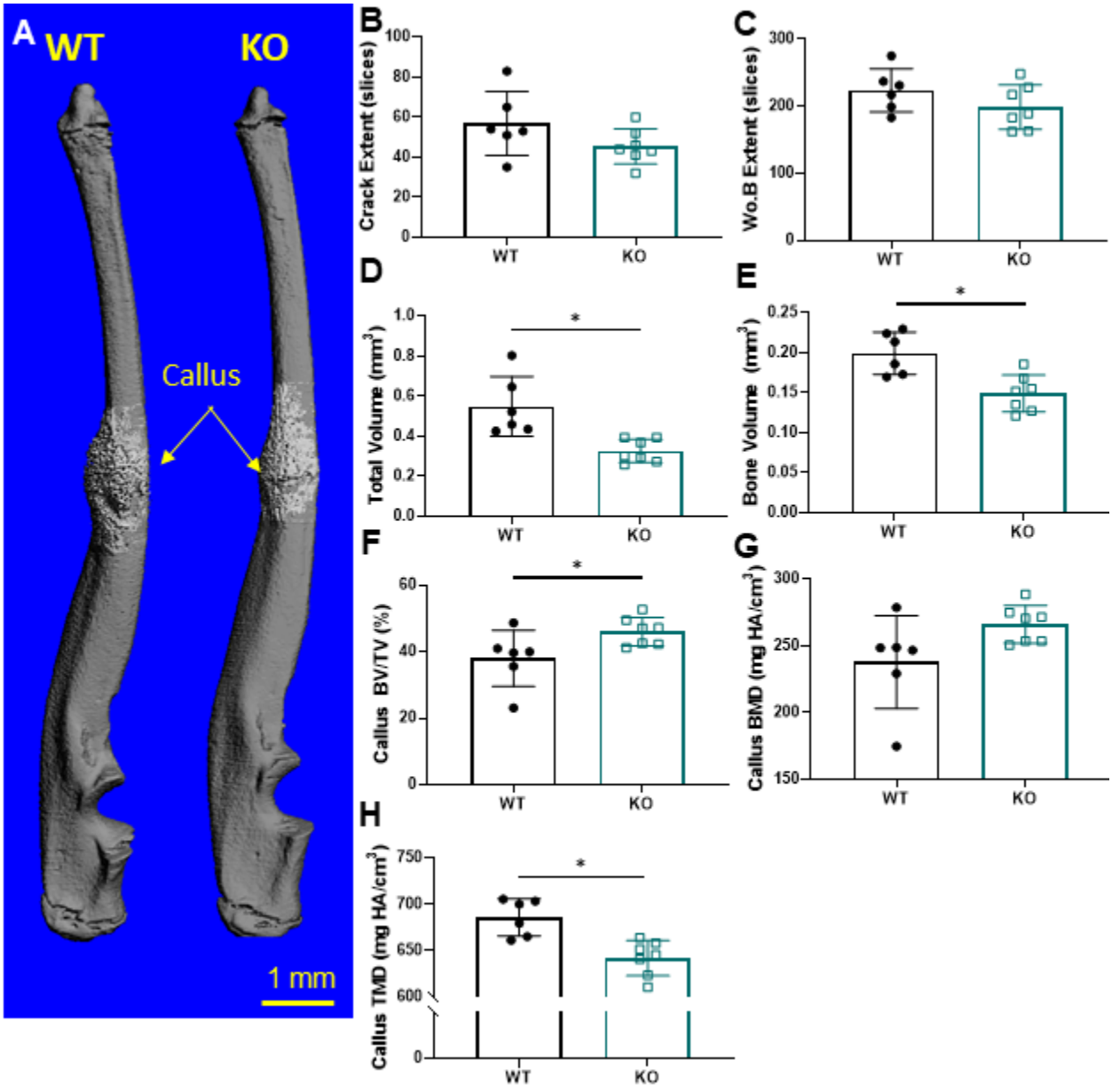

Figure 5.3: Cxcr2 knockout mice form smaller callus with less bone following stress fracture. MicroCT was used to evaluate callus and bone formation 7 days after stress fracture. 3D reconstructions are shown for samples with median total callus volume for each group (A). Crack extent (B) and woven bone (Wo.B) extent (C) were comparable between groups. Cxcr2 KO mice formed callus with less total callus volume (D) and less bone volume (E) than wildtype controls. Callus bone volume fraction (F) was increased in knockout mice. Callus bone mineral density (BMD) (G) was unchanged between groups, but tissue mineral density (TMD) (H) was reduced in Cxcr2 KO mice. Asterisk (*) denotes $p<0.05$.

5.3.4 Cxcr2 knockout impaired neutrophil recruitment to stress fracture callus

Immunohistochemistry was used to stain stress fracture callus for Gr-1, a marker of neutrophils. Wild type callus showed abundant staining for Gr-1, representing robust recruitment of neutrophils as an immediate response (1 day post-injury) to stress fracture (Figure 5.4 A). However, Cxcr2 knockout animals had little staining for Gr-1, representing deficient neutrophil recruitment to the site of stress fracture injury (Figure 5.4 B). Quantification of Gr-1 staining reveals a significant decrease in the cell density of Gr-1 positive cells in stress fracture callus of Cxcr2 knockout mice (Figure 5.4 C).

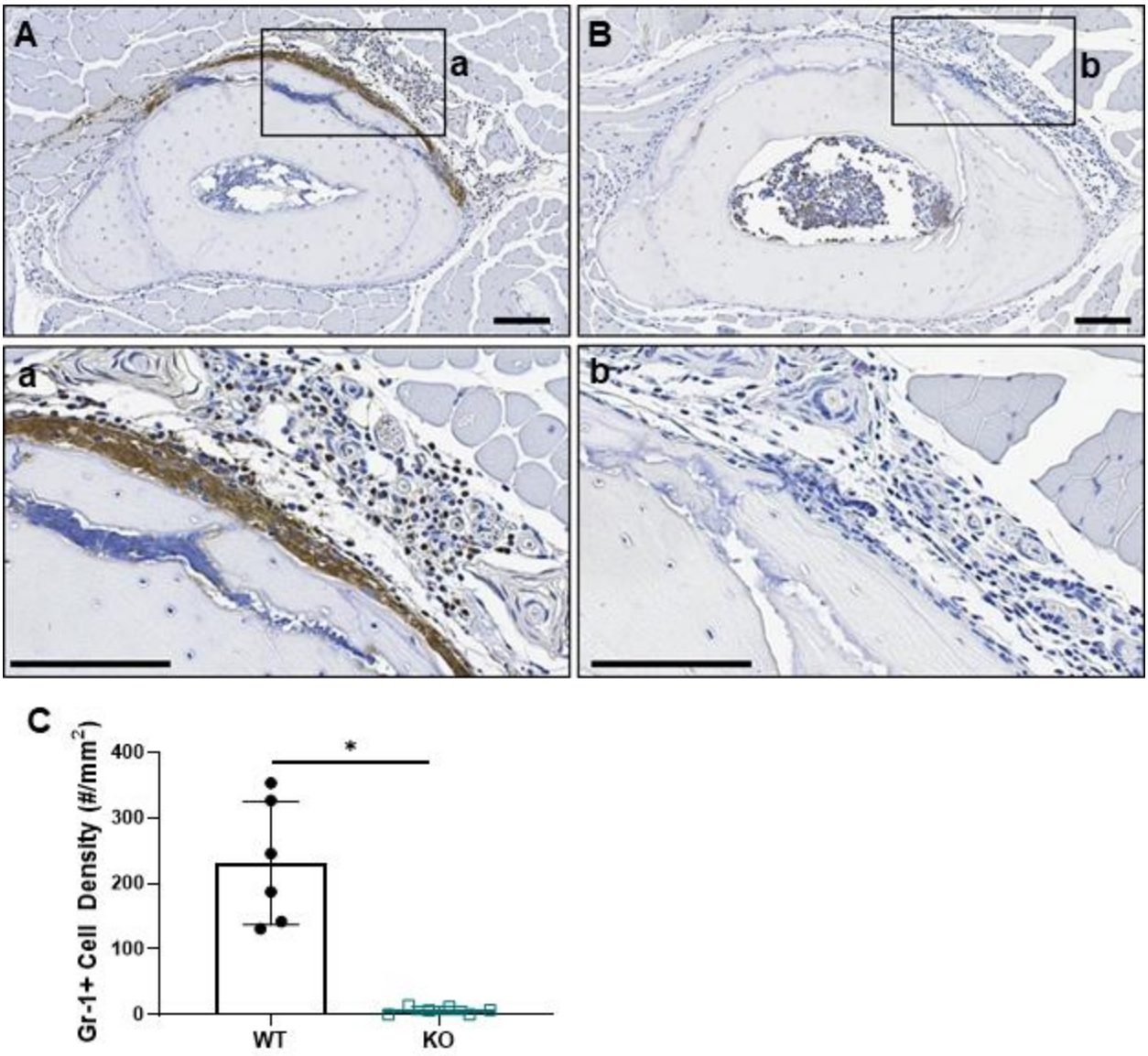

Figure 5.4: Cxcr2 knockout mice have reduced neutrophil recruitment after stress fracture. Immunohistochemistry was performed on day 1 stress fracture callus using an antibody for Gr-1, a marker for neutrophils. Representative images for a wildtype (A) and Cxcr2 KO (B) callus are shown. Quantifying the cell density of neutrophils in the callus reveals significantly fewer neutrophils in Cxcr2 Ko callus (C). Scale bars are 100 μm length. Asterisk (*) denotes $p<0.0001$.

5.3.5 LysM cKO mice do not phenocopy global knockout mice

Due to the reduction in neutrophils in the stress fracture callus of Cxcr2 KO mice, we wanted to more closely examine if CXC signaling through neutrophils was responsible for the reduced bone formation phenotype. To do this, LysM cKO mice were used to examine if deletion of *Cxcr2* in myeloid cells would result in a comparable diminished bone formation following stress fracture as observed in Cxcr2 KO mice. Expression of *Cxcr2* in bone marrow was reduced by 68% ($p < 0.0001$) in LysM cKO mice as compared to control mice. In microCT measurements of full fracture callus and stress fracture callus, LysM cKO mice had comparable total callus volume and callus bone volume as compared to LysM control mice (Figure 5.5 B-E). These results do not follow the same reduction in stress fracture total volume and bone volume that is seen in the global Cxcr2 KO mice.

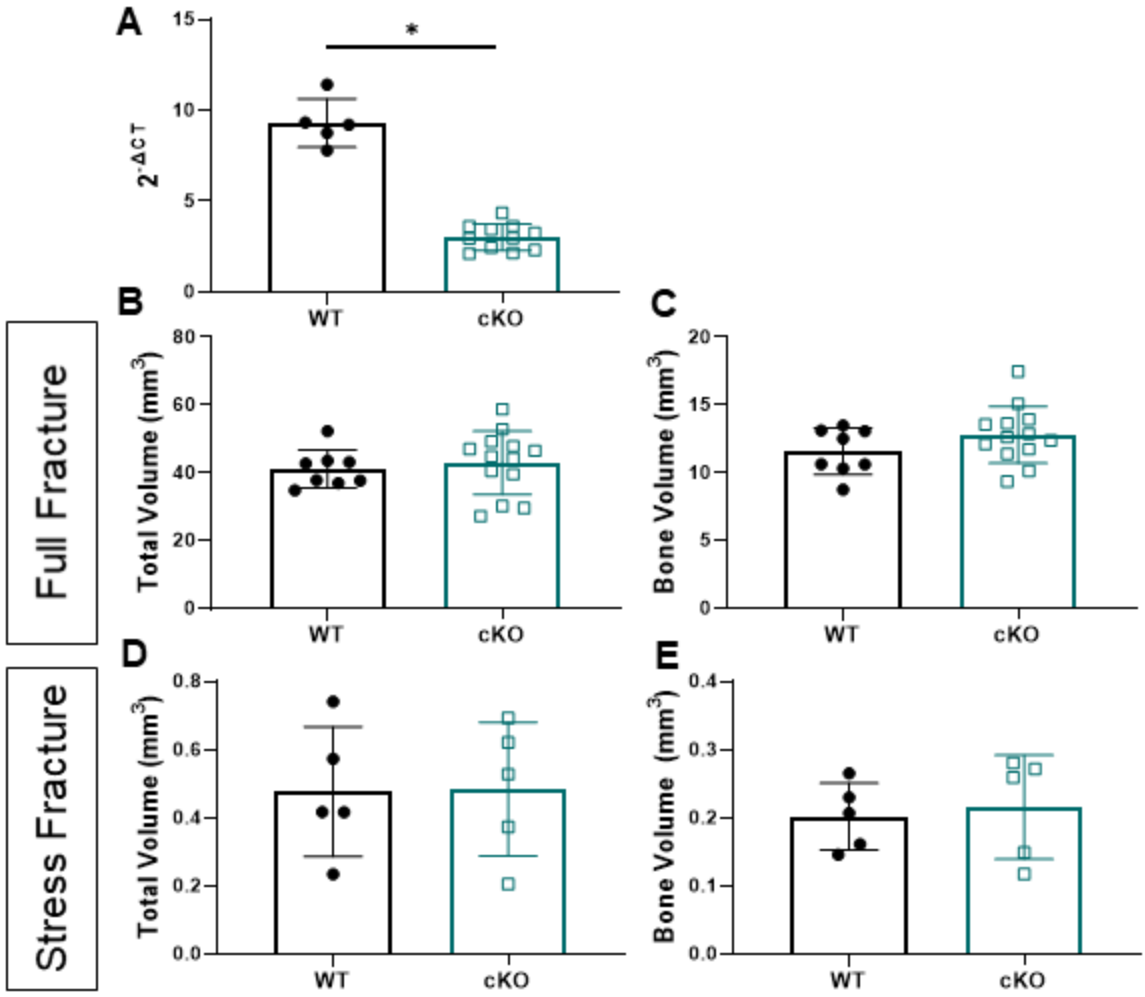

Figure 5.5: LysM-Cxcr2 mice did not recapitulate the global knockout phenotype. Expression of Cxcr2 was reduced by 68% in the bone marrow of cKO mice (A). Following full fracture, total volume (B) and bone volume (C) of callus was consistent between groups. Following stress fracture, total volume (D) and bone volume (E) were consistent between groups.

5.4 Discussion

Following skeletal injury, ligands of the CXC chemokine family are highly upregulated, suggesting they are involved in the inflammatory phase of fracture repair [28]. We set out to explore the role of CXC family chemokines in bone fracture repair by using knockout mice targeting the shared CXC receptor *Cxcr2*.

Cxcr2 knockout mice have a diminished capacity to form callus and woven bone following stress fracture injury. Furthermore, Cxcr2 knockout mice showed reduced staining for the neutrophil marker Gr-1, suggesting an inability to recruit neutrophils to the site of injury. This lack of the earliest responding immune cell likely plays a role in the diminished repair process, highlighting the important role of CXC family chemokines as some of the earliest responders to skeletal injury.

We used Cxcr2 KO mice in order to study the role of the CXC family of chemokines on post-injury bone formation. At 14 days following a femur full fracture, no difference was observed in callus or bone formation between wild type and Cxcr2 KO mice (Figure 5.2). However, 7 days following stress fracture, Cxcr2 KO mice have smaller callus, indicating a reduced capacity for intramembranous repair (Figure 5.3), which is the predominant mode of osteogenesis in stress fracture repair [6,89]. Crack burden was similar between groups, indicating consistent damage burden created within the stress fracture model. Total callus volume and callus bone volume were both significantly reduced in the Cxcr2 KO mice. However, woven bone extent was unchanged between groups. This indicates that KO and wild type animals display an equal capacity to form callus along the periosteal surface, and that Cxcr2 KO mice are forming smaller callus due to reduced expansion of the callus away from the periosteum. Callus

bone mineral density was increased in knockout mice. This is driven by total callus volume being more greatly reduced than bone volume – resulting in increased volumetric bone density. On the other hand, tissue mineral density was reduced in knockout mice – indicating that the woven bone formed by knockout mice is less mineralized than wild type counterparts at this 7 day time point.

A similar reduction in intramembranous bone formation has been reported in a model of cranial defects by Bischoff et al [36]. They report Cxcr2 KO mice had 48% less bone ingrowth within the defect site and a 54% reduction in vasculature within new bone matrix. However, it is not evident why Cxcr2 KO does not interfere with post-injury endochondral ossification as seen in the full fracture model.

Cxcr2 KO mice were found to have smaller body weights than control animals (Figure 5.1). After adjusting for smaller size, baseline skeletal features or cancellous and cortical bone were comparable between Cxcr2 KO and control animals (Table 5.2). An earlier study by Bischoff and colleagues [36] which reported a reduction in cancellous and cortical bone of Cxcr2 KO mice. However, this study did not adjust for reduced body weight.

We used IHC for the neutrophil marker Gr-1 to assess recruitment of immune cells to the site of stress fracture 1 day after injury. Cxcr2 KO mice showed a greatly reduced potential for neutrophil recruitment to the site of stress fracture than did wild type mice (Figure 5.4). Neutrophils are the first responders of the immune system and play critical roles in wound repair through their capacity to release important inflammatory cytokines [171–173]. A previous report has shown that a reduction in neutrophil recruitment, as achieved through systemic antibody treatment, is harmful for bone fracture repair [21]. Therefore, the inability for Cxcr2 KO mice to

recruit neutrophils to the site of stress fracture injury is possibly a major contributor to reduced bone formation.

Conditionally deleting *Cxcr2* in immune cells using LysM Cre mice did not display the same blunted response to stress fracture as did Cxcr2 KO mice (Figure 5.5). This might be explained by deletion efficiency of *Cxcr2* in neutrophils being less than 100%. Therefore, although most neutrophils are unable to respond to stress fracture injury, enough do respond and provide enough support to promote normal bone formation.

While histology demonstrations that neutrophil recruitment was greatly impaired by global knockout of *Cxcr2*, we did not investigate if other mechanism may also be playing a role in the reduced bone formation observed following stress fracture in these mice. Worth investigating would be the role that Cxcr2 plays in angiogenesis. It has been reported that Cxcr2 on endothelial cells is an important moderator of cell recruitment and angiogenesis [116,174,175]. It would be interesting to examine if this contributes to reduced bone formation by limiting the recruitment of endothelial cells to stress fracture callus and thus limiting angiogenic-osteogenic coupling which is vitally important to bone formation [166,167].

Also of importance might be to investigate the mechanisms through which neutrophils are impacting fracture repair. Specifically of interest would be how levels of inflammatory cytokines in the early fracture callus are impacted by Cxcr2 KO.

In summary, we report that Cxcr2 KO mice have a reduced ability to form callus and bone following stress fracture injury. This blunted bone formation is likely due to a disrupted inflammatory phase, due to the inability of Cxcr2 KO mice to recruit neutrophils to the site of injury. This work highlights the importance of a well-balanced inflammatory phase to successful fracture repair and characterizes CXC family chemokines as contributors this phase.

Chapter 6: Conclusions and Future Directions

6.1 Conclusions

Bone possesses an impressive capacity for repair following skeletal injury. However, in the clinic, fracture repair fails in up to 10% of patients [38]. This represents a fundamental need for better understanding of the complex biology of fracture repair. Depending on the extent of injury and mechanical stability of the injured bone, repair can occur through either intramembranous formation, featuring direct formation of bone callus, or endochondral formation, which features a cartilage intermediary callus [7]. We utilize two clinically relevant injury models to initiate these bone formation cascades. Stress fractures are used to initiate intramembranous bone formation and full fractures are used to initiate endochondral repair. Using these models in combination with transgenic mouse models provide valuable insight into the biology of fracture repair.

Successful fracture repair is contingent on the coordinated response of many different cell types, signaling pathways, and biological processes. By more completely understanding the events related to successful repair, we can more thoroughly understand how to best correct sub-standard repair. In order to better understand the biology of fracture repair, we used RNA-seq to analyze the gene expression across several time points in models of intramembranous or endochondral ossification.

Intramembranous and endochondral bone formation were found to have distinct patterns of gene expression. Endochondral ossification involved a greater number of differentially expressed genes. An inflammatory reaction was present for both formation types, however endochondral repair had expression of inflammatory genes and recruitment of immune cells that were orders of magnitude greater than observed in intramembranous repair. Intramembranous repair was more enriched for genes associated with osteoblasts and bone formation and intramembranous repair was uniquely enriched for PI3K-Akt signaling. This is likely reflective of more simplified nature of bone formation in intramembranous repair – which does not require production of a cartilage intermediary callus. We also observed a dramatic downregulation of voltage gated ion channels in endochondral repair, which was not present in intramembranous repair.

The inflammatory phase of fracture repair is the initial response of the skeleton to injury and promotes successful repair through the production of cytokines and the recruitment of immune cells [8,9]. *Interleukin-6 (IL-6*) is a component of this inflammatory response and is highly upregulated in response to skeletal injury. Despite its abundance in the early fracture callus, how *IL-6* influences fracture repair remains incompletely understood. Therefore, we sought to examine the role *IL-6* plays in fracture repair using two clinically relevant injury models *and IL-6* global knockout mice (IL-6 KO).

IL-6 KO mice developed normal skeletons and respond similarly to controls following full fracture. But in response to stress fracture, IL-6 KO mice display an enhanced ability for repair. IL-6 KO mice have larger calluses with more bone formation following stress fracture than control animals. We investigated several mechanisms through which *IL-6* may lead to increased bone formation. There were no changes in osteoclast number or immune cell

recruitment in IL-6 KO mice. Early gene expression was slightly altered and featured a decreased inflammatory response and higher expression of *Wnt1*, a bone anabolic protein. Furthermore, an examination of osteoblast function using a model for loading induced bone formation revealed IL-6 KO osteoblasts to have an increased capacity for woven bone production. In response to stress fracture, *IL-6* appears to be an antagonist of bone formation and global knockout of *IL-6* increases callus production through slight alterations of inflammatory gene expression and increased osteoblast matrix production.

The CXC family of chemokines are also highly upregulated as part of the inflammatory phase of fracture repair. CXC chemokines signal through *CXC family receptor 2* (*Cxcr2*) to induce chemotaxis of cells, primarily neutrophils and endothelial cells [115,175]. But, the impact of *Cxcr2* on fracture repair has not been reported. To explore this, we utilized two clinically relevant fracture models and *Cxcr2* global knockout mice (Cxcr2 KO).

Cxcr2 KO mice had reduced body weights as compared to controls but developed proportionally normal skeletons. Cxcr2 KO mice also had comparable callus formation following full fracture. In response to stress fracture, Cxcr2 KO mice had a reduced capacity for repair – displaying smaller calluses with less bone formation than control animals. Histology revealed a substantial reduction in the recruitment of neutrophils to the site of stress fracture in Cxcr2 KO mice. Therefore, we concluded that the CXC family of chemokines assist in post-injury bone formation through recruitment of neutrophils during the inflammatory response.

Overall, this work provides insight into fracture repair and post-injury bone formation. We were able to detail the transcriptomic profile of endochondral and intramembranous bone formation across several time points. These data revealed several novel genes and pathways

involved in fracture repair, including voltage gated ion channels in endochondral repair and PI3K-Akt signaling in intramembranous repair. We hope this work can serve as a roadmap for "normal" fracture repair, which can be a resource for planning future experiments on the genetic contributors to bone formation.

Furthermore, we explored two components of the inflammatory phase of fracture repair. In intramembranous bone formation following stress fracture, IL-6 KO was found to enhance repair. On the contrary, Cxcr2 KO was found to decrease callus formation. These results highlight the delicate balance of inflammation, which can serve as both a help and hindrance to optimal fracture repair.

6.2 Future Directions

The work detailed in this dissertation provides insight into both the temporal gene expression and the inflammatory reaction involved in fracture repair. However, as some questions were answered herein, many others remain unanswered and could be intriguing topics for future study.

In particular, the work describing the transcriptomics of fracture repair provides a plethora of interesting follow up experiments. We found that the PI3K-Akt signaling pathway was enriched throughout several time points in intramembranous repair. The role of this pathway in osteogenesis is not completely understood. Assessment of this pathway in stress fracture repair could be of importance to the field. Using pathway antagonists and agonists, experiments could be designed to measure the impact of PI3K-Akt signaling on bone formation.

Another finding from the transcriptional profiling was the potent down regulation of voltage gated ion channels during endochondral repair. There are not many reports regarding the role of ion channels in bone repair. Therefore any investigation into the systematic downregulation of ion transporters in endochondral repair would be illuminating. Ion channel antagonists and agonists could be used to stimulate ion channels during fracture repair and bone formation could be measured.

Through investigations of *IL-6*, we were able to reveal IL-6 KO led to increased bone formation after stress fracture. Several follow up experiments could be potentially enlightening. Firstly, in an attempt to identify the cellular source of *IL-6*, we were unable to recapitulate the increase bone formation phenotype using conditional deletion of *IL-6* with LysM or Osteocalcin Cre lines. This indicates that either we targeted the wrong population of cells for deletion, or that *IL-6* is produced by several cell types. An experiment to measure *IL-6* expression by qPCR in stress fracture callus of LysM and OC cKO mice could answer what proportion of *IL-6* is supplied by each cell population. Depending on the results, this experiment could also explain the lack of phenotype in these mice, especially if compensating sources of *IL-6* prevent a dramatic decrease in *IL-6* production. It would also be possible to attempt these stress fracture experiments again using different Cre lines. One interesting target would be osterix Cre, which would cast a wider net than OC Cre and target all bone cells in the osteoblast lineage from progenitors to mature osteocytes.

Another interesting question involves identifying the cell population which is responding to *IL-6* in stress fracture repair. Our experiments, which reveal increased woven bone production, suggest that osteoblasts are responsive to *IL-6* signaling, and thus IL-6 KO. It could be

interesting to conditionally target the osteoblast lineage for *IL-6 Receptor* deletion and observe if increased bone formation occurs after stress fracture.

We found decreased stress fracture repair capabilities in Cxcr2 KO mice. However, a more thorough examination of these mice should be completed. *Cxcr2* is known to facilitate the chemotaxis of both neutrophils and endothelial cells. We were able to show through histology the reduced potential for neutrophil recruitment to the stress fracture callus of Cxcr2 KO mice. However, we did not investigate the possibility of diminished angiogenesis from reduced endothelial cell migration. One experiment to test angiogenesis would be histology staining for endomucin, a marker for endothelial cells. If Cxcr2 stress fracture callus showed reduced staining of endomucin relative to callus size, it could be concluded that reduced bone formation after stress fracture is caused by reductions in both neutrophil and endothelial cell recruitment.

References

[1] D. Nandiraju, I. Ahmed, Human skeletal physiology and factors affecting its modeling and remodeling, Fertility and Sterility. 112 (2019) 775–781. https://doi.org/10.1016/j.fertnstert.2019.10.005.

[2] F.G.F. Tresguerres, J. Torres, J. López-Quiles, G. Hernández, J.A. Vega, I.F. Tresguerres, The osteocyte: A multifunctional cell within the bone, Annals of Anatomy - Anatomischer Anzeiger. 227 (2020) 151422. https://doi.org/10.1016/j.aanat.2019.151422.

[3] D.J. Hadjidakis, I.I. Androulakis, Bone Remodeling, Annals of the New York Academy of Sciences. 1092 (2006) 385–396. https://doi.org/10.1196/annals.1365.035.

[4] S.J. Roberts, N. van Gastel, G. Carmeliet, F.P. Luyten, Uncovering the periosteum for skeletal regeneration: The stem cell that lies beneath, Bone. 70 (2015) 10–18. https://doi.org/10.1016/j.bone.2014.08.007.

[5] L.C. Gerstenfeld, D.M. Cullinane, G.L. Barnes, D.T. Graves, T.A. Einhorn, Fracture healing as a post-natal developmental process: Molecular, spatial, and temporal aspects of its regulation, Journal of Cellular Biochemistry. 88 (2003) 873–884. https://doi.org/10.1002/jcb.10435.

[6] Z. Thompson, T. Miclau, D. Hu, J.A. Helms, A model for intramembranous ossification during fracture healing, Journal of Orthopaedic Research. 20 (2002) 1091–1098. https://doi.org/10.1016/S0736-0266(02)00017-7.

[7] R. Marsell, T.A. Einhorn, The biology of fracture healing, Injury. 42 (2011) 551–555. https://doi.org/10.1016/j.injury.2011.03.031.

[8] F. Loi, L.A. Córdova, J. Pajarinen, T. Lin, Z. Yao, S.B. Goodman, Inflammation, fracture and bone repair, Bone. 86 (2016) 119–130. https://doi.org/10.1016/j.bone.2016.02.020.

[9] P. Hoff, T. Gaber, C. Strehl, K. Schmidt-Bleek, A. Lang, D. Huscher, G.R. Burmester, G. Schmidmaier, C. Perka, G.N. Duda, F. Buttgereit, Immunological characterization of the early human fracture hematoma, Immunologic Research. 64 (2016) 1195–1206. https://doi.org/10.1007/s12026-016-8868-9.

[10] L. Claes, S. Recknagel, A. Ignatius, Fracture healing under healthy and inflammatory conditions, Nat Rev Rheumatol. 8 (2012) 133–143. https://doi.org/10.1038/nrrheum.2012.1.

[11] O. Grundnes, O. Reikeraas, Effects of macrophage activation on bone healing, J Orthop Sci. 5 (2000) 243–247. https://doi.org/10.1007/s007760050159.

[12] K. Kaiser, K. Prystaz, A. Vikman, M. Haffner-Luntzer, S. Bergdolt, G. Strauss, G.H. Waetzig, S. Rose-John, A. Ignatius, Pharmacological inhibition of IL-6 trans-signaling improves compromised fracture healing after severe trauma, Naunyn-Schmiedeberg's Archives of Pharmacology. 391 (2018) 523–536. https://doi.org/10.1007/s00210-018-1483-7.

[13] O.W. Bastian, A. Kuijer, L. Koenderman, R.K. Stellato, W.W. van Solinge, L.P. Leenen, T.J. Blokhuis, Impaired bone healing in multitrauma patients is associated with altered leukocyte kinetics after major trauma, J Inflamm Res. 9 (2016) 69–78. https://doi.org/10.2147/JIR.S101064.

[14] E.K. Rodriguez, C. Boulton, M.J. Weaver, L.M. Herder, J.H. Morgan, A.T. Chacko, P.T. Appleton, D. Zurakowski, M.S. Vrahas, Predictive factors of distal femoral fracture

nonunion after lateral locked plating: a retrospective multicenter case-control study of 283 fractures, Injury. 45 (2014) 554–559. https://doi.org/10.1016/j.injury.2013.10.042.
[15] M.S. Gaston, A.H.R.W. Simpson, Inhibition of fracture healing, The Journal of Bone and Joint Surgery. British Volume. 89-B (2007) 1553–1560. https://doi.org/10.1302/0301-620X.89B12.19671.
[16] T. Roszer, Inflammation as death or life signal in diabetic fracture healing, Inflamm. Res. 60 (2011) 3–10. https://doi.org/10.1007/s00011-010-0246-9.
[17] J. Richardson, A.M. Hill, C.J.C. Johnston, A. McGregor, A.R. Norrish, D. Eastwood, C.B.D. Lavy, Fracture healing in HIV-positive populations, J Bone Joint Surg Br. 90 (2008) 988–994. https://doi.org/10.1302/0301-620X.90B8.20861.
[18] R.D. Altman, L.L. Latta, R. Keer, K. Renfree, F.J. Hornicek, K. Banovac, Effect of nonsteroidal antiinflammatory drugs on fracture healing: a laboratory study in rats, J Orthop Trauma. 9 (1995) 392–400. https://doi.org/10.1097/00005131-199505000-00006.
[19] P. Wheeler, Do non-steroidal anti-inflammatory drugs adversely affect stress fracture healing? A short review, British Journal of Sports Medicine. 39 (2005) 65–69. https://doi.org/10.1136/bjsm.2004.012492.
[20] C.K. Butcher, D.R. Marsh, Nonsteroidal anti-inflammatory drugs delay tibial fracture union, Injury. 27 (1996) 375. https://doi.org/10.1016/0020-1383(96)86874-4.
[21] A. Kovtun, S. Bergdolt, R. Wiegner, P. Radermacher, M. Huber-Lang, A. Ignatius, The crucial role of neutrophil granulocytes in bone fracture healing, Eur Cell Mater. 32 (2016) 152–162.
[22] L. Vi, G.S. Baht, H. Whetstone, A. Ng, Q. Wei, R. Poon, S. Mylvaganam, M. Grynpas, B.A. Alman, Macrophages Promote Osteoblastic Differentiation In Vivo: Implications in Fracture Repair and Bone Homeostasis: MACROPHAGES PROMOTE OSTEOBLASTIC DIFFERENTIATION, J Bone Miner Res. 30 (2015) 1090–1102. https://doi.org/10.1002/jbmr.2422.
[23] P. Guihard, M.-A. Boutet, B. Brounais-Le Royer, A.-L. Gamblin, J. Amiaud, A. Renaud, M. Berreur, F. Rédini, D. Heymann, P. Layrolle, F. Blanchard, Oncostatin M, an Inflammatory Cytokine Produced by Macrophages, Supports Intramembranous Bone Healing in a Mouse Model of Tibia Injury, The American Journal of Pathology. 185 (2015) 765–775. https://doi.org/10.1016/j.ajpath.2014.11.008.
[24] C. Schlundt, T. El Khassawna, A. Serra, A. Dienelt, S. Wendler, H. Schell, N. van Rooijen, A. Radbruch, R. Lucius, S. Hartmann, G.N. Duda, K. Schmidt-Bleek, Macrophages in bone fracture healing: Their essential role in endochondral ossification, Bone. 106 (2018) 78–89. https://doi.org/10.1016/j.bone.2015.10.019.
[25] T. Ono, K. Okamoto, T. Nakashima, T. Nitta, S. Hori, Y. Iwakura, H. Takayanagi, IL-17-producing γδ T cells enhance bone regeneration, Nature Communications. 7 (2016). https://doi.org/10.1038/ncomms10928.
[26] I. Könnecke, A. Serra, T. El Khassawna, C. Schlundt, H. Schell, A. Hauser, A. Ellinghaus, H.-D. Volk, A. Radbruch, G.N. Duda, K. Schmidt-Bleek, T and B cells participate in bone repair by infiltrating the fracture callus in a two-wave fashion, Bone. 64 (2014) 155–165. https://doi.org/10.1016/j.bone.2014.03.052.
[27] G. Sun, Y. Wang, Y. Ti, J. Wang, J. Zhao, H. Qian, Regulatory B cell is critical in bone union process through suppressing proinflammatory cytokines and stimulating Foxp3 in Treg cells, Clin Exp Pharmacol Physiol. 44 (2017) 455–462. https://doi.org/10.1111/1440-1681.12719.

[28] B.A. Coates, J.A. McKenzie, E.G. Buettmann, X. Liu, P.M. Gontarz, B. Zhang, M.J. Silva, Transcriptional profiling of intramembranous and endochondral ossification after fracture in mice, Bone. 127 (2019) 577–591. https://doi.org/10.1016/j.bone.2019.07.022.
[29] J.A. McKenzie, E.C. Bixby, M.J. Silva, Differential gene expression from microarray analysis distinguishes woven and lamellar bone formation in the rat ulna following mechanical loading, PLoS ONE. 6 (2011) e29328. https://doi.org/10.1371/journal.pone.0029328.
[30] X. Zhang, E.M. Schwarz, D.A. Young, J.E. Puzas, R.N. Rosier, R.J. O'Keefe, Cyclooxygenase-2 regulates mesenchymal cell differentiation into the osteoblast lineage and is critically involved in bone repair, Journal of Clinical Investigation. 109 (2002) 1405–1415. https://doi.org/10.1172/JCI15681.
[31] A.M. Simon, M.B. Manigrasso, J.P. O'Connor, Cyclo-Oxygenase 2 Function Is Essential for Bone Fracture Healing, Journal of Bone and Mineral Research. 17 (2002) 963–976. https://doi.org/10.1359/jbmr.2002.17.6.963.
[32] J. Lange, A. Sapozhnikova, C. Lu, D. Hu, X. Li, T. Miclau, R.S. Marcucio, Action of IL-1beta during fracture healing, J. Orthop. Res. 28 (2010) 778–784. https://doi.org/10.1002/jor.21061.
[33] X. Wang, T.E. Friis, P.P. Masci, R.W. Crawford, W. Liao, Y. Xiao, Alteration of blood clot structures by interleukin-1 beta in association with bone defects healing, Scientific Reports. 6 (2016). https://doi.org/10.1038/srep35645.
[34] X. Yang, B.F. Ricciardi, A. Hernandez-Soria, Y. Shi, N. Pleshko Camacho, M.P.G. Bostrom, Callus mineralization and maturation are delayed during fracture healing in interleukin-6 knockout mice, Bone. 41 (2007) 928–936. https://doi.org/10.1016/j.bone.2007.07.022.
[35] A. Wallace, T.E. Cooney, R. Englund, J.D. Lubahn, Effects of Interleukin-6 Ablation on Fracture Healing in Mice, Journal of Orthopaedic Research. 29 (2011) 1437–1442. https://doi.org/10.1002/jor.21367.
[36] D.S. Bischoff, T. Sakamoto, K. Ishida, N.S. Makhijani, H.E. Gruber, D.T. Yamaguchi, CXC receptor knockout mice: Characterization of skeletal features and membranous bone healing in the adult mouse☆, Bone. 48 (2011) 267–274. https://doi.org/10.1016/j.bone.2010.09.026.
[37] W.-C. Pollak, Andrew N. Sylvia I., Fracture Trends, in: United States Bone and Joint Initiative: The Burden of Musculoskeletal Diseases in the United States (BMUS), Third Edition, 2014, Rosemont, IL, n.d. http://www.boneandjointburden.org/ (accessed November 13, 2018).
[38] R. Zura, Z. Xiong, T. Einhorn, J.T. Watson, R.F. Ostrum, M.J. Prayson, G.J. Della Rocca, S. Mehta, T. McKinley, Z. Wang, R.G. Steen, Epidemiology of Fracture Nonunion in 18 Human Bones, JAMA Surgery. 151 (2016) e162775. https://doi.org/10.1001/jamasurg.2016.2775.
[39] D. Marsh, Concepts of Fracture Union, Delayed Union, and Nonunion:, Clinical Orthopaedics and Related Research. 355S (1998) S22–S30. https://doi.org/10.1097/00003086-199810001-00004.
[40] A. Bell, D. Templeman, J.C. Weinlein, Nonunion of the Femur and Tibia, Orthopedic Clinics of North America. 47 (2016) 365–375. https://doi.org/10.1016/j.ocl.2015.09.010.

[41] G.M. Calori, W. Albisetti, A. Agus, S. Iori, L. Tagliabue, Risk factors contributing to fracture non-unions, Injury. 38 (2007) S11–S18. https://doi.org/10.1016/S0020-1383(07)80004-0.
[42] G. Andersson, American Academy of Orthopaedic Surgeons, The burden of musculoskeletal diseases in the United States: prevalence, societal, and economic cost., American Academy of Orthopaedic Surgeons, Rosemont, IL, 2008.
[43] A.S. Nazrun, M.N. Tzar, S.A. Mokhtar, I.N. Mohamed, A systematic review of the outcomes of osteoporotic fracture patients after hospital discharge: morbidity, subsequent fractures, and mortality, Ther Clin Risk Manag. 10 (2014) 937–948. https://doi.org/10.2147/TCRM.S72456.
[44] X. Liu, J.A. McKenzie, C.W. Maschhoff, M.J. Gardner, M.J. Silva, Exogenous hedgehog antagonist delays but does not prevent fracture healing in young mice, Bone. 103 (2017) 241–251. https://doi.org/10.1016/j.bone.2017.07.017.
[45] M.B. Schaffler, K. Choi, C. Milgrom, Aging and matrix microdamage accumulation in human compact bone, Bone. 17 (1995) 521–525.
[46] M.B. Schaffler, Role of bone turnover in microdamage, Osteoporos Int. 14 Suppl 5 (2003) S73-77; discussion S77-80. https://doi.org/10.1007/s00198-003-1477-1.
[47] D.B. Burr, Remodeling and the repair of fatigue damage, Calcif. Tissue Int. 53 Suppl 1 (1993) S75-80; discussion S80-81.
[48] Z. Seref-Ferlengez, O.D. Kennedy, M.B. Schaffler, Bone microdamage, remodeling and bone fragility: how much damage is too much damage?, BoneKEy Reports. 4 (2015). https://doi.org/10.1038/bonekey.2015.11.
[49] C.J. Hernandez, Bone fatigue, stress fractures and bone repair (Sun Valley 2013), IBMS BoneKEy. 10 (2013). https://doi.org/10.1038/bonekey.2013.182.
[50] D. Taylor, T.C. Lee, Microdamage and mechanical behaviour: predicting failure and remodelling in compact bone, J. Anat. 203 (2003) 203–211. https://doi.org/10.1046/j.1469-7580.2003.00194.x.
[51] E.S. Siris, R. Adler, J. Bilezikian, M. Bolognese, B. Dawson-Hughes, M.J. Favus, S.T. Harris, S.M. Jan de Beur, S. Khosla, N.E. Lane, R. Lindsay, A.D. Nana, E.S. Orwoll, K. Saag, S. Silverman, N.B. Watts, The clinical diagnosis of osteoporosis: a position statement from the National Bone Health Alliance Working Group, Osteoporos Int. 25 (2014) 1439–1443. https://doi.org/10.1007/s00198-014-2655-z.
[52] E. Seeman, Reduced bone formation and increased bone resorption: rational targets for the treatment of osteoporosis, Osteoporosis International. 14 (2003) 2–8. https://doi.org/10.1007/s00198-002-1340-9.
[53] E.M. Lewiecki, Bisphosphonates for the treatment of osteoporosis: insights for clinicians, Ther Adv Chronic Dis. 1 (2010) 115–128. https://doi.org/10.1177/2040622310374783.
[54] M.T. Drake, B.L. Clarke, S. Khosla, Bisphosphonates: mechanism of action and role in clinical practice, Mayo Clin. Proc. 83 (2008) 1032–1045. https://doi.org/10.4065/83.9.1032.
[55] C. Acevedo, H. Bale, B. Gludovatz, A. Wat, S.Y. Tang, M. Wang, B. Busse, E.A. Zimmermann, E. Schaible, M.R. Allen, D.B. Burr, R.O. Ritchie, Alendronate treatment alters bone tissues at multiple structural levels in healthy canine cortical bone, Bone. 81 (2015) 352–363. https://doi.org/10.1016/j.bone.2015.08.002.
[56] T. Mashiba, T. Hirano, C.H. Turner, M.R. Forwood, C.C. Johnston, D.B. Burr, Suppressed bone turnover by bisphosphonates increases microdamage accumulation and reduces some

biomechanical properties in dog rib, J. Bone Miner. Res. 15 (2000) 613–620. https://doi.org/10.1359/jbmr.2000.15.4.613.
[57] Y.-F. Hsieh, M.J. Silva, In vivo fatigue loading of the rat ulna induces both bone formation and resorption and leads to time-related changes in bone mechanical properties and density, J. Orthop. Res. 20 (2002) 764–771. https://doi.org/10.1016/S0736-0266(01)00161-9.
[58] B. Wu, C. Zhang, B. Chen, L. Zhang, R. Dai, X. Wu, Y. Jiang, E. Liao, Self-Repair of Rat Cortical Bone Microdamage after Fatigue Loading In Vivo, International Journal of Endocrinology. 2013 (2013) 1–8. https://doi.org/10.1155/2013/321074.
[59] V. Bentolila, T.M. Boyce, D.P. Fyhrie, R. Drumb, T.M. Skerry, M.B. Schaffler, Intracortical remodeling in adult rat long bones after fatigue loading, Bone. 23 (1998) 275–281.
[60] B.C. Herman, L. Cardoso, R.J. Majeska, K.J. Jepsen, M.B. Schaffler, Activation of bone remodeling after fatigue: Differential response to linear microcracks and diffuse damage, Bone. 47 (2010) 766–772. https://doi.org/10.1016/j.bone.2010.07.006.
[61] Z. Seref-Ferlengez, J. Basta-Pljakic, O.D. Kennedy, C.J. Philemon, M.B. Schaffler, Structural and Mechanical Repair of Diffuse Damage in Cortical Bone In Vivo: REPAIR OF DIFFUSE DAMAGE IN BONE IN VIVO, J Bone Miner Res. 29 (2014) 2537–2544. https://doi.org/10.1002/jbmr.2309.
[62] M. Martiniakova, M. Vondrakova, M. Fabis, Investigation of the Microscopic Structure of Rabbit Compact Bone Tissue, Scripta Medica. 76 (2003) 215–220.
[63] U.E. Pazzaglia, G. Bonaspetti, L.F. Rodella, F. Ranchetti, F. Azzola, Design, morphometry and development of the secondary osteonal system in the femoral shaft of the rabbit, J. Anat. 211 (2007) 303–312. https://doi.org/10.1111/j.1469-7580.2007.00782.x.
[64] O.D. Kennedy, O. Brennan, P. Mauer, S.M. Rackard, F.J. O'Brien, D. Taylor, T.C. Lee, The effects of increased intracortical remodeling on microcrack behaviour in compact bone, Bone. 43 (2008) 889–893. https://doi.org/10.1016/j.bone.2008.07.235.
[65] D. Vashishth, Hierarchy of Bone Microdamage at Multiple Length Scales, Int J Fatigue. 29 (2007) 1024–1033. https://doi.org/10.1016/j.ijfatigue.2006.09.010.
[66] B.L. Pennypacker, L.T. Duong, T.E. Cusick, P.J. Masarachia, M.A. Gentile, J.-Y. Gauthier, W.C. Black, B.B. Scott, R. Samadfam, S.Y. Smith, D.B. Kimmel, Cathepsin K inhibitors prevent bone loss in estrogen-deficient rabbits, J Bone Miner Res. 26 (2011) 252–262. https://doi.org/10.1002/jbmr.223.
[67] D. Jing, X. Hao, F. Xu, J. Liu, F. Xu, E. Luo, G. Meng, Effects of local delivery of BMP2, zoledronate and their combination on bone microarchitecture, biomechanics and bone turnover in osteoporotic rabbits, Sci Rep. 6 (2016) 28537. https://doi.org/10.1038/srep28537.
[68] P.R. Jensen, T.L. Andersen, B.L. Pennypacker, L.T. Duong, J.-M. Delaissé, The Bone Resorption Inhibitors Odanacatib and Alendronate Affect Post-Osteoclastic Events Differently in Ovariectomized Rabbits, Calcif Tissue Int. 94 (2014) 212–222. https://doi.org/10.1007/s00223-013-9800-0.
[69] J.G. Barrett, S.J. Sample, J. McCarthy, V.L. Kalscheur, P. Muir, L. Prokuski, Effect of short-term treatment with alendronate on ulnar bone adaptation to cyclic fatigue loading in rats, J. Orthop. Res. 25 (2007) 1070–1077. https://doi.org/10.1002/jor.20395.

[70] E.G. Buettmann, M.J. Silva, Development of an in vivo bone fatigue damage model using axial compression of the rabbit forelimb, J Biomech. 49 (2016) 3564–3569. https://doi.org/10.1016/j.jbiomech.2016.08.020.
[71] D.W. Dempster, J.E. Compston, M.K. Drezner, F.H. Glorieux, J.A. Kanis, H. Malluche, P.J. Meunier, S.M. Ott, R.R. Recker, A.M. Parfitt, Standardized nomenclature, symbols, and units for bone histomorphometry: A 2012 update of the report of the ASBMR Histomorphometry Nomenclature Committee, J Bone Miner Res. 28 (2013) 2–17. https://doi.org/10.1002/jbmr.1805.
[72] D.B. Burr, M. Hooser, Alterations to the en bloc basic fuchsin staining protocol for the demonstration of microdamage produced in vivo, Bone. 17 (1995) 431–433.
[73] C.P. Jerome, C.S. Carlson, T.C. Register, F.T. Bain, M.J. Jayo, D.S. Weaver, M.R. Adams, Bone functional changes in intact, ovariectomized, and ovariectomized, hormone-supplemented adult cynomolgus monkeys (Macaca fascicularis) evaluated by serum markers and dynamic histomorphometry, Journal of Bone and Mineral Research. 9 (2009) 527–540. https://doi.org/10.1002/jbmr.5650090413.
[74] A.P. Baumann, M.W. Aref, T.L. Turnbull, A.G. Robling, G.L. Niebur, M.R. Allen, R.K. Roeder, Development of an in vivo rabbit ulnar loading model, Bone. 75 (2015) 55–61. https://doi.org/10.1016/j.bone.2015.01.022.
[75] M. Pepper, V. Akuthota, E.C. McCarty, The Pathophysiology of Stress Fractures, Clinics in Sports Medicine. 25 (2006) 1–16. https://doi.org/10.1016/j.csm.2005.08.010.
[76] S.J. Warden, D.B. Burr, P.D. Brukner, Stress Fractures: Pathophysiology, Epidemiology, and Risk Factors, (n.d.) 7.
[77] M. Schaffler, Bone fatigue and remodeling in the devlopment of stress fractures, in: D. Burr, C. Milgrom (Eds.), Musculoskeletal Fatigue and Stress Fractures, CRC Press, Boca Raton, 2000: pp. 161–82.
[78] K.L. Bennell, P.D. Brukner, EPIDEMIOLOGY AND SITE SPECIFICITY OF STRESS FRACTURES, Clinics in Sports Medicine. 16 (1997) 179–196. https://doi.org/10.1016/S0278-5919(05)70016-8.
[79] F. Bonnarens, T.A. Einhorn, Production of a standard closed fracture in laboratory animal bone, Journal of Orthopaedic Research. 2 (1984) 97–101. https://doi.org/10.1002/jor.1100020115.
[80] J.H. Hebb, J.W. Ashley, L. McDaniel, L.A. Lopas, J. Tobias, K.D. Hankenson, J. Ahn, Bone healing in an aged murine fracture model is characterized by sustained callus inflammation and decreased cell proliferation: FRACTURE HEALING IN AGED MICE, Journal of Orthopaedic Research. (2017). https://doi.org/10.1002/jor.23652.
[81] C. Yuan, J. Cai, Time-series expression profile analysis of fracture healing in young and old mice, Mol Med Rep. 16 (2017) 4529–4536. https://doi.org/10.3892/mmr.2017.7198.
[82] R. Grimes, K.J. Jepsen, J.L. Fitch, T.A. Einhorn, L.C. Gerstenfeld, The transcriptome of fracture healing defines mechanisms of coordination of skeletal and vascular development during endochondral bone formation, Journal of Bone and Mineral Research. 26 (2011) 2597–2609. https://doi.org/10.1002/jbmr.486.
[83] C.H. Rundle, H. Wang, H. Yu, R.B. Chadwick, E.I. Davis, J.E. Wergedal, K.-H.W. Lau, S. Mohan, J.T. Ryaby, D.J. Baylink, Microarray analysis of gene expression during the inflammation and endochondral bone formation stages of rat femur fracture repair, Bone. 38 (2006) 521–529. https://doi.org/10.1016/j.bone.2005.09.015.

[84] G. Zimmermann, K.H.K. Schmeckenbecher, S. Boeuf, S. Weiss, R. Bock, A. Moghaddam, W. Richter, Differential gene expression analysis in fracture callus of patients with regular and failed bone healing, Injury. 43 (2012) 347–356. https://doi.org/10.1016/j.injury.2011.10.031.
[85] M. Hauser, M. Siegrist, I. Keller, W. Hofstetter, Healing of fractures in osteoporotic bones in mice treated with bisphosphonates - A transcriptome analysis, Bone. 112 (2018) 107–119. https://doi.org/10.1016/j.bone.2018.04.017.
[86] K.M. Sanders, E. Seeman, A.M. Ugoni, J.A. Pasco, T.J. Martin, B. Skoric, G.C. Nicholson, M.A. Kotowicz, Age- and Gender-Specific Rate of Fractures in Australia: A Population-Based Study, Osteoporosis International. 10 (1999) 240–247. https://doi.org/10.1007/s001980050222.
[87] S.R. Cummings, L.J. Melton, Epidemiology and outcomes of osteoporotic fractures, The Lancet. 359 (2002) 1761–1767. https://doi.org/10.1016/S0140-6736(02)08657-9.
[88] S.H. McBride-Gagyi, J.A. McKenzie, E.G. Buettmann, M.J. Gardner, M.J. Silva, Bmp2 conditional knockout in osteoblasts and endothelial cells does not impair bone formation after injury or mechanical loading in adult mice, Bone. 81 (2015) 533–543. https://doi.org/10.1016/j.bone.2015.09.003.
[89] M.D. Martinez, G.J. Schmid, J.A. McKenzie, D.M. Ornitz, M.J. Silva, Healing of non-displaced fractures produced by fatigue loading of the mouse ulna, Bone. 46 (2010) 1604–1612. https://doi.org/10.1016/j.bone.2010.02.030.
[90] D.W. Huang, B.T. Sherman, R.A. Lempicki, Systematic and integrative analysis of large gene lists using DAVID bioinformatics resources, Nature Protocols. 4 (2009) 44–57. https://doi.org/10.1038/nprot.2008.211.
[91] D.W. Huang, B.T. Sherman, R.A. Lempicki, Bioinformatics enrichment tools: paths toward the comprehensive functional analysis of large gene lists, Nucleic Acids Research. 37 (2009) 1–13. https://doi.org/10.1093/nar/gkn923.
[92] M. Angelova, P. Charoentong, H. Hackl, M.L. Fischer, R. Snajder, A.M. Krogsdam, M.J. Waldner, G. Bindea, B. Mlecnik, J. Galon, Z. Trajanoski, Characterization of the immunophenotypes and antigenomes of colorectal cancers reveals distinct tumor escape mechanisms and novel targets for immunotherapy, Genome Biology. 16 (2015). https://doi.org/10.1186/s13059-015-0620-6.
[93] G. Calabrese, B.J. Bennett, L. Orozco, H.M. Kang, E. Eskin, C. Dombret, O. De Backer, A.J. Lusis, C.R. Farber, Systems Genetic Analysis of Osteoblast-Lineage Cells, PLoS Genetics. 8 (2012) e1003150. https://doi.org/10.1371/journal.pgen.1003150.
[94] G.A. Rodan, M. Noda, Gene expression in osteoblastic cells, Crit. Rev. Eukaryot. Gene Expr. 1 (1991) 85–98.
[95] A.D. Barrow, N. Raynal, T.L. Andersen, D.A. Slatter, D. Bihan, N. Pugh, M. Cella, T. Kim, J. Rho, T. Negishi-Koga, J.-M. Delaisse, H. Takayanagi, J. Lorenzo, M. Colonna, R.W. Farndale, Y. Choi, J. Trowsdale, OSCAR is a collagen receptor that costimulates osteoclastogenesis in DAP12-deficient humans and mice, J. Clin. Invest. 121 (2011) 3505–3516. https://doi.org/10.1172/JCI45913.
[96] N. Irie, Y. Takada, Y. Watanabe, Y. Matsuzaki, C. Naruse, M. Asano, Y. Iwakura, T. Suda, K. Matsuo, Bidirectional signaling through ephrinA2-EphA2 enhances osteoclastogenesis and suppresses osteoblastogenesis, J. Biol. Chem. 284 (2009) 14637–14644. https://doi.org/10.1074/jbc.M807598200.

[97] J. Jiang, H. Li, F.S. Fahid, E. Filbert, K.E. Safavi, L.S. Spangberg, Q. Zhu, Quantitative analysis of osteoclast-specific gene markers stimulated by lipopolysaccharide, J Endod. 32 (2006) 742–746. https://doi.org/10.1016/j.joen.2006.02.003.
[98] M. Yang, M.J. Birnbaum, C.A. MacKay, A. Mason-Savas, B. Thompson, P.R. Odgren, Osteoclast stimulatory transmembrane protein (OC-STAMP), a novel protein induced by RANKL that promotes osteoclast differentiation, J. Cell. Physiol. 215 (2008) 497–505. https://doi.org/10.1002/jcp.21331.
[99] M. Zaidi, H.C. Blair, B.S. Moonga, E. Abe, C.L.-H. Huang, Osteoclastogenesis, Bone Resorption, and Osteoclast-Based Therapeutics, Journal of Bone and Mineral Research. 18 (2003) 599–609. https://doi.org/10.1359/jbmr.2003.18.4.599.
[100] C.G. Rivera, S. Mellberg, L. Claesson-Welsh, J.S. Bader, A.S. Popel, Analysis of VEGF-A Regulated Gene Expression in Endothelial Cells to Identify Genes Linked to Angiogenesis, PLoS ONE. 6 (2011) e24887. https://doi.org/10.1371/journal.pone.0024887.
[101] M.F. Sabbagh, J.S. Heng, C. Luo, R.G. Castanon, J.R. Nery, A. Rattner, L.A. Goff, J.R. Ecker, J. Nathans, Transcriptional and epigenomic landscapes of CNS and non-CNS vascular endothelial cells, Elife. 7 (2018). https://doi.org/10.7554/eLife.36187.
[102] T. Dehne, R. Schenk, C. Perka, L. Morawietz, A. Pruss, M. Sittinger, C. Kaps, J. Ringe, Gene expression profiling of primary human articular chondrocytes in high-density micromasses reveals patterns of recovery, maintenance, re- and dedifferentiation, Gene. 462 (2010) 8–17. https://doi.org/10.1016/j.gene.2010.04.006.
[103] F.-T. Xu, H.-M. Li, C.-Y. Zhao, Z.-J. Liang, M.-H. Huang, Q. Li, Y.-C. Chen, G.-Y. Chi, Characterization of Chondrogenic Gene Expression and Cartilage Phenotype Differentiation in Human Breast Adipose-Derived Stem Cells Promoted by Ginsenoside Rg1 In Vitro, Cell. Physiol. Biochem. 37 (2015) 1890–1902. https://doi.org/10.1159/000438550.
[104] L. Yu, H. Liu, M. Yan, J. Yang, F. Long, K. Muneoka, Y. Chen, Shox2 is required for chondrocyte proliferation and maturation in proximal limb skeleton, Dev. Biol. 306 (2007) 549–559. https://doi.org/10.1016/j.ydbio.2007.03.518.
[105] Y.-C. Lin, S.R. Roffler, Y.-T. Yan, R.-B. Yang, Disruption of Scube2 Impairs Endochondral Bone Formation, J. Bone Miner. Res. 30 (2015) 1255–1267. https://doi.org/10.1002/jbmr.2451.
[106] C.N. Withers, D.M. Brown, I. Byiringiro, M.R. Allen, K.W. Condon, J. Satin, D.A. Andres, Rad GTPase is essential for the regulation of bone density and bone marrow adipose tissue in mice, Bone. 103 (2017) 270–280. https://doi.org/10.1016/j.bone.2017.07.018.
[107] F. Paic, J.C. Igwe, R. Nori, M.S. Kronenberg, T. Franceschetti, P. Harrington, L. Kuo, D.-G. Shin, D.W. Rowe, S.E. Harris, I. Kalajzic, Identification of differentially expressed genes between osteoblasts and osteocytes, Bone. 45 (2009) 682–692. https://doi.org/10.1016/j.bone.2009.06.010.
[108] S.R. Bond, A. Lau, S. Penuela, A.V. Sampaio, T.M. Underhill, D.W. Laird, C.C. Naus, Pannexin 3 is a novel target for Runx2, expressed by osteoblasts and mature growth plate chondrocytes, J. Bone Miner. Res. 26 (2011) 2911–2922. https://doi.org/10.1002/jbmr.509.
[109] M. Ishikawa, Y. Yamada, The Role of Pannexin 3 in Bone Biology, Journal of Dental Research. 96 (2017) 372–379. https://doi.org/10.1177/0022034516678203.

[110] Y. Zhou, J.-Y. Wang, H. Feng, C. Wang, L. Li, D. Wu, H. Lei, H. Li, L.-L. Wu, Overexpression of C1q/Tumor Necrosis Factor–Related Protein-3 Promotes Phosphate-Induced Vascular Smooth Muscle Cell Calcification Both In Vivo and In Vitro, Arteriosclerosis, Thrombosis, and Vascular Biology. 34 (2014) 1002–1010. https://doi.org/10.1161/ATVBAHA.114.303301.
[111] A.K. Coussens, C.R. Wilkinson, I.P. Hughes, C.P. Morris, A. van Daal, P.J. Anderson, B.C. Powell, Unravelling the molecular control of calvarial suture fusion in children with craniosynostosis, BMC Genomics. 8 (2007) 458. https://doi.org/10.1186/1471-2164-8-458.
[112] G.R. Wohl, D.A. Towler, M.J. Silva, Stress fracture healing: Fatigue loading of the rat ulna induces upregulation in expression of osteogenic and angiogenic genes that mimic the intramembranous portion of fracture repair, Bone. 44 (2009) 320–330. https://doi.org/10.1016/j.bone.2008.09.010.
[113] P. Fedi, A. Bafico, A.N. Soria, W.H. Burgess, T. Miki, D.P. Bottaro, M.H. Kraus, S.A. Aaronson, Isolation and Biochemical Characterization of the Human Dkk-1 Homologue, a Novel Inhibitor of Mammalian Wnt Signaling, Journal of Biological Chemistry. 274 (1999) 19465–19472. https://doi.org/10.1074/jbc.274.27.19465.
[114] X. Li, Y. Zhang, H. Kang, W. Liu, P. Liu, J. Zhang, S.E. Harris, D. Wu, Sclerostin Binds to LRP5/6 and Antagonizes Canonical Wnt Signaling, Journal of Biological Chemistry. 280 (2005) 19883–19887. https://doi.org/10.1074/jbc.M413274200.
[115] K.J. Eash, A.M. Greenbaum, P.K. Gopalan, D.C. Link, CXCR2 and CXCR4 antagonistically regulate neutrophil trafficking from murine bone marrow, Journal of Clinical Investigation. 120 (2010) 2423–2431. https://doi.org/10.1172/JCI41649.
[116] J.A. Belperio, M.P. Keane, D.A. Arenberg, C.L. Addison, J.E. Ehlert, M.D. Burdick, R.M. Strieter, CXC chemokines in angiogenesis, Journal of Leukocyte Biology. 68 (2000) 1–8. https://doi.org/10.1189/jlb.68.1.1.
[117] L.C. Gerstenfeld, M. Thiede, K. Seibert, C. Mielke, D. Phippard, B. Svagr, D. Cullinane, T.A. Einhorn, Differential inhibition of fracture healing by non-selective and cyclooxygenase-2 selective non-steroidal anti-inflammatory drugs, Journal of Orthopaedic Research. 21 (2003) 670–675. https://doi.org/10.1016/S0736-0266(03)00003-2.
[118] Y. Takeuchi, S. Watanabe, G. Ishii, S. Takeda, K. Nakayama, S. Fukumoto, Y. Kaneta, D. Inoue, T. Matsumoto, K. Harigaya, T. Fujita, Interleukin-11 as a Stimulatory Factor for Bone Formation Prevents Bone Loss with Advancing Age in Mice, Journal of Biological Chemistry. 277 (2002) 49011–49018. https://doi.org/10.1074/jbc.M207804200.
[119] L. Campbell, C.R. Saville, P.J. Murray, S.M. Cruickshank, M.J. Hardman, Local Arginase 1 Activity Is Required for Cutaneous Wound Healing, J Invest Dermatol. 133 (2013) 2461–2470. https://doi.org/10.1038/jid.2013.164.
[120] T. Kon, T.-J. Cho, T. Aizawa, M. Yamazaki, N. Nooh, D. Graves, L.C. Gerstenfeld, T.A. Einhorn, Expression of Osteoprotegerin, Receptor Activator of NF-κB Ligand (Osteoprotegerin Ligand) and Related Proinflammatory Cytokines During Fracture Healing, Journal of Bone and Mineral Research. 16 (2001) 1004–1014. https://doi.org/10.1359/jbmr.2001.16.6.1004.
[121] D.N. Tatakis, Interleukin-1 and bone metabolism: a review, J. Periodontol. 64 (1993) 416–431.
[122] M. Li, D.F. Carpio, Y. Zheng, P. Bruzzo, V. Singh, F. Ouaaz, R.M. Medzhitov, A.A. Beg, An Essential Role of the NF- B/Toll-Like Receptor Pathway in Induction of Inflammatory

and Tissue-Repair Gene Expression by Necrotic Cells, The Journal of Immunology. 166 (2001) 7128–7135. https://doi.org/10.4049/jimmunol.166.12.7128.
[123] C. Shi, T. Jia, S. Mendez-Ferrer, T.M. Hohl, N.V. Serbina, L. Lipuma, I. Leiner, M.O. Li, P.S. Frenette, E.G. Pamer, Bone Marrow Mesenchymal Stem and Progenitor Cells Induce Monocyte Emigration in Response to Circulating Toll-like Receptor Ligands, Immunity. 34 (2011) 590–601. https://doi.org/10.1016/j.immuni.2011.02.016.
[124] L.J. Kidd, N.R. Cowling, A.C. Wu, W.L. Kelly, M.R. Forwood, Selective and non-selective cyclooxygenase inhibitors delay stress fracture healing in the rat ulna, Journal of Orthopaedic Research. 31 (2013) 235–242. https://doi.org/10.1002/jor.22203.
[125] S. Levy, J.M. Feduska, A. Sawant, S.R. Gilbert, J.A. Hensel, S. Ponnazhagan, Immature myeloid cells are critical for enhancing bone fracture healing through angiogenic cascade, Bone. 93 (2016) 113–124. https://doi.org/10.1016/j.bone.2016.09.018.
[126] D. Toben, I. Schroeder, T. El Khassawna, M. Mehta, J.-E. Hoffmann, J.-T. Frisch, H. Schell, J. Lienau, A. Serra, A. Radbruch, G.N. Duda, Fracture healing is accelerated in the absence of the adaptive immune system, Journal of Bone and Mineral Research. 26 (2011) 113–124. https://doi.org/10.1002/jbmr.185.
[127] N.H. Kelly, J.C. Schimenti, F.P. Ross, M.C.H. van der Meulen, Transcriptional profiling of cortical versus cancellous bone from mechanically-loaded murine tibiae reveals differential gene expression, Bone. 86 (2016) 22–29. https://doi.org/10.1016/j.bone.2016.02.007.
[128] A. Yang, Y. Lu, J. Xing, Z. Li, X. Yin, C. Dou, S. Dong, F. Luo, Z. Xie, T. Hou, J. Xu, IL-8 Enhances Therapeutic Effects of BMSCs on Bone Regeneration via CXCR2-Mediated PI3k/Akt Signaling Pathway, Cellular Physiology and Biochemistry. 48 (2018) 361–370. https://doi.org/10.1159/000491742.
[129] I.M. McGonnell, A.E. Grigoriadis, E.W.-F. Lam, J.S. Price, A. Sunters, A specific role for phosphoinositide 3-kinase and AKT in osteoblasts?, Front Endocrinol (Lausanne). 3 (2012) 88. https://doi.org/10.3389/fendo.2012.00088.
[130] Z. Qu, S. Guo, G. Fang, Z. Cui, Y. Liu, AKT Pathway Affects Bone Regeneration in Nonunion Treated with Umbilical Cord-Derived Mesenchymal Stem Cells, Cell Biochem. Biophys. 71 (2015) 1543–1551. https://doi.org/10.1007/s12013-014-0378-6.
[131] V. Scanlon, B. Walia, J. Yu, M. Hansen, H. Drissi, P. Maye, A. Sanjay, Loss of Cbl-PI3K interaction modulates the periosteal response to fracture by enhancing osteogenic commitment and differentiation, Bone. 95 (2017) 124–135. https://doi.org/10.1016/j.bone.2016.11.020.
[132] M. Levin, Endogenous bioelectrical networks store non-genetic patterning information during development and regeneration: Bioelectric networks as epi-genetic controls of growth and form, The Journal of Physiology. 592 (2014) 2295–2305. https://doi.org/10.1113/jphysiol.2014.271940.
[133] B.M. Franklin, S.R. Voss, J.L. Osborn, Ion channel signaling influences cellular proliferation and phagocyte activity during axolotl tail regeneration, Mechanisms of Development. 146 (2017) 42–54. https://doi.org/10.1016/j.mod.2017.06.001.
[134] P. Valverde, T. Kawai, M.A. Taubman, Selective Blockade of Voltage-Gated Potassium Channels Reduces Inflammatory Bone Resorption in Experimental Periodontal Disease, Journal of Bone and Mineral Research. 19 (2003) 155–164. https://doi.org/10.1359/jbmr.0301213.

[135] S.J. Petty, C.J. Milligan, M. Todaro, K.L. Richards, P.K. Kularathna, C.N. Pagel, C.R. French, E.L. Hill-Yardin, T.J. O'Brien, J.D. Wark, E.J. Mackie, S. Petrou, The antiepileptic medications carbamazepine and phenytoin inhibit native sodium currents in murine osteoblasts, Epilepsia. 57 (2016) 1398–1405. https://doi.org/10.1111/epi.13474.
[136] R.B. Moraes, L. Corrêa, J.G.C. Luz, Adverse effects of the amlodipine on bone healing of the mandibular fracture: an experimental study in rats, Oral Maxillofac Surg. 15 (2011) 93–101. https://doi.org/10.1007/s10006-010-0237-6.
[137] Y. Atalay, F. Bozkurt, Y. Gonul, O. Cakmak, K.S. Agacayak, I. Kose, O. Hazman, H. Keles, O. Turamanlar, M. Eroglu, The effects of amlodipine and platelet rich plasma on bone healing in rats, Drug Design, Development and Therapy. (2015) 1973. https://doi.org/10.2147/DDDT.S80778.
[138] B.A. Brouwer, I.S.J. Merkies, M.M. Gerrits, S.G. Waxman, J.G.J. Hoeijmakers, C.G. Faber, Painful neuropathies: the emerging role of sodium channelopathies: Painful neuropathies: the emerging role of sodium channelopathies, Journal of the Peripheral Nervous System. 19 (2014) 53–65. https://doi.org/10.1111/jns5.12071.
[139] J. Park, Z.D. Luo, Calcium channel functions in pain processing, Channels (Austin). 4 (2010) 510–517.
[140] C. Tsantoulas, S.B. McMahon, Opening paths to novel analgesics: the role of potassium channels in chronic pain, Trends Neurosci. 37 (2014) 146–158. https://doi.org/10.1016/j.tins.2013.12.002.
[141] C. Tsantoulas, L. Zhu, P. Yip, J. Grist, G.J. Michael, S.B. McMahon, Kv2 dysfunction after peripheral axotomy enhances sensory neuron responsiveness to sustained input, Experimental Neurology. 251 (2014) 115–126. https://doi.org/10.1016/j.expneurol.2013.11.011.
[142] L.-Y. Chien, J.-K. Cheng, D. Chu, C.-F. Cheng, M.-L. Tsaur, Reduced Expression of A-Type Potassium Channels in Primary Sensory Neurons Induces Mechanical Hypersensitivity, Journal of Neuroscience. 27 (2007) 9855–9865. https://doi.org/10.1523/JNEUROSCI.0604-07.2007.
[143] R.J. Bunn, G. Burke, C. Connelly, G. Li, D. Marsh, Inflammation – a double edged sword in high-energy fractures?, Orthopaedic Proceedings. 87-B (2005) 265–266. https://doi.org/10.1302/0301-620X.87BSUPP_III.0870265c.
[144] J. Scheller, A. Chalaris, D. Schmidt-Arras, S. Rose-John, The pro- and anti-inflammatory properties of the cytokine interleukin-6, Biochimica et Biophysica Acta (BBA) - Molecular Cell Research. 1813 (2011) 878–888. https://doi.org/10.1016/j.bbamcr.2011.01.034.
[145] A. Chalaris, B. Rabe, K. Paliga, H. Lange, T. Laskay, C.A. Fielding, S.A. Jones, S. Rose-John, J. Scheller, Apoptosis is a natural stimulus of IL6R shedding and contributes to the proinflammatory trans-signaling function of neutrophils, Blood. 110 (2007) 1748–1755. https://doi.org/10.1182/blood-2007-01-067918.
[146] G. Kaplanski, IL-6: a regulator of the transition from neutrophil to monocyte recruitment during inflammation, Trends in Immunology. 24 (2003) 25–29. https://doi.org/10.1016/S1471-4906(02)00013-3.
[147] N.A. Sims, Cell-specific paracrine actions of IL-6 family cytokines from bone, marrow and muscle that control bone formation and resorption, The International Journal of Biochemistry & Cell Biology. 79 (2016) 14–23. https://doi.org/10.1016/j.biocel.2016.08.003.

[148] C.D. Richards, C. Langdon, P. Deschamps, D. Pennica, S.G. Shaughnessy, STIMULATION OF OSTEOCLAST DIFFERENTIATION IN VITRO BY MOUSE ONCOSTATIN M, LEUKAEMIA INHIBITORY FACTOR, CARDIOTROPHIN-1 AND INTERLEUKIN 6: SYNERGY WITH DEXAMETHASONE, Cytokine. 12 (2000) 613–621. https://doi.org/10.1006/cyto.1999.0635.
[149] R. Jilka, G. Hangoc, G. Girasole, G. Passeri, D. Williams, J. Abrams, B. Boyce, H. Broxmeyer, S. Manolagas, Increased osteoclast development after estrogen loss: mediation by interleukin-6, Science. 257 (1992) 88–91. https://doi.org/10.1126/science.1621100.
[150] F. De Benedetti, N. Rucci, A. Del Fattore, B. Peruzzi, R. Paro, M. Longo, M. Vivarelli, F. Muratori, S. Berni, P. Ballanti, S. Ferrari, A. Teti, Impaired skeletal development in interleukin-6–transgenic mice: A model for the impact of chronic inflammation on the growing skeletal system, Arthritis Rheum. 54 (2006) 3551–3563. https://doi.org/10.1002/art.22175.
[151] S. Kaneshiro, K. Ebina, K. Shi, C. Higuchi, M. Hirao, M. Okamoto, K. Koizumi, T. Morimoto, H. Yoshikawa, J. Hashimoto, IL-6 negatively regulates osteoblast differentiation through the SHP2/MEK2 and SHP2/Akt2 pathways in vitro, J. Bone Miner. Metab. 32 (2014) 378–392. https://doi.org/10.1007/s00774-013-0514-1.
[152] X. Li, Z. Zhou, Y. Zhang, H. Yang, IL-6 Contributes to the Defective Osteogenesis of Bone Marrow Stromal Cells from the Vertebral Body of the Glucocorticoid-Induced Osteoporotic Mouse, PLOS ONE. 11 (2016) e0154677. https://doi.org/10.1371/journal.pone.0154677.
[153] N.E. McGregor, M. Murat, J. Elango, I.J. Poulton, E.C. Walker, B. Crimeen-Irwin, P.W.M. Ho, J.H. Gooi, T.J. Martin, N.A. Sims, IL-6 exhibits both *cis* - and *trans* -signaling in osteocytes and osteoblasts, but only *trans* -signaling promotes bone formation and osteoclastogenesis, Journal of Biological Chemistry. 294 (2019) 7850–7863. https://doi.org/10.1074/jbc.RA119.008074.
[154] M. Kopf, H. Baumann, G. Freer, M. Freudenberg, M. Lamers, T. Kishimoto, R. Zinkernagel, H. Bluethmann, G. Köhler, Impaired immune and acute-phase responses in interleukin-6-deficient mice, Nature. 368 (1994) 339–342. https://doi.org/10.1038/368339a0.
[155] A. Quintana, M. Erta, B. Ferrer, G. Comes, M. Giralt, J. Hidalgo, Astrocyte-specific deficiency of interleukin-6 and its receptor reveal specific roles in survival, body weight and behavior, Brain, Behavior, and Immunity. 27 (2013) 162–173. https://doi.org/10.1016/j.bbi.2012.10.011.
[156] R.L. De Souza, M. Matsuura, F. Eckstein, S.C.F. Rawlinson, L.E. Lanyon, A.A. Pitsillides, Non-invasive axial loading of mouse tibiae increases cortical bone formation and modifies trabecular organization: A new model to study cortical and cancellous compartments in a single loaded element, Bone. 37 (2005) 810–818. https://doi.org/10.1016/j.bone.2005.07.022.
[157] D. Sun, M.D. Brodt, H.M. Zannit, N. Holguin, M.J. Silva, Evaluation of loading parameters for murine axial tibial loading: Stimulating cortical bone formation while reducing loading duration: EVALUATION OF LOADING PARAMETERS FOR MURINE AXIAL TIBIAL, J. Orthop. Res. (2017). https://doi.org/10.1002/jor.23727.

[158] M.D. Brodt, M.J. Silva, Aged mice have enhanced endocortical response and normal periosteal response compared with young-adult mice following 1 week of axial tibial compression, J Bone Miner Res. 25 (2010) 2006–2015. https://doi.org/10.1002/jbmr.96.
[159] Y. Ishimi, C. Miyaura, C.H. Jin, T. Akatsu, E. Abe, Y. Nakamura, A. Yamaguchi, S. Yoshiki, T. Matsuda, T. Hirano, IL-6 is produced by osteoblasts and induces bone resorption, J. Immunol. 145 (1990) 3297–3303.
[160] R. Baron, M. Kneissel, WNT signaling in bone homeostasis and disease: from human mutations to treatments, Nat. Med. 19 (2013) 179–192. https://doi.org/10.1038/nm.3074.
[161] N. Holguin, M.D. Brodt, M.J. Silva, Activation of Wnt Signaling by Mechanical Loading Is Impaired in the Bone of Old Mice, Journal of Bone and Mineral Research. 31 (2016) 2215–2226. https://doi.org/10.1002/jbmr.2900.
[162] G.S. Klasan, D. Ivanac, D.J. Erzen, A. Picard, S. Takasawa, S. Peharec, J. Arbanas, D. Girotto, R. Jerkovic, Reg3G gene expression in regenerating skeletal muscle and corresponding nerve, Muscle & Nerve. 49 (2014) 61–68. https://doi.org/10.1002/mus.23877.
[163] H. Okamoto, The Reg gene family and Reg proteins: with special attention to the regeneration of pancreatic beta-cells, J Hepatobiliary Pancreat Surg. 6 (1999) 254–262. https://doi.org/10.1007/s005340050115.
[164] C.H. Turner, I. Owan, T. Alvey, J. Hulman, J.M. Hock, Recruitment and Proliferative Responses of Osteoblasts After Mechanical Loading In Vivo Determined Using Sustained-Release Bromodeoxyuridine, Bone. 22 (1998) 463–469. https://doi.org/10.1016/S8756-3282(98)00041-6.
[165] A. Kovtun, S. Bergdolt, R. Wiegner, P. Radermacher, M. Huber-Lang, A. Ignatius, The crucial role of neutrophil granulocytes in bone fracture healing, Eur Cell Mater. 32 (2016) 152–162. https://doi.org/10.22203/ecm.v032a10.
[166] R.E. Tomlinson, J.A. McKenzie, A.H. Schmieder, G.R. Wohl, G.M. Lanza, M.J. Silva, Angiogenesis is required for stress fracture healing in rats, Bone. 52 (2013) 212–219. https://doi.org/10.1016/j.bone.2012.09.035.
[167] M.R. Hausman, M.B. Schaffler, R.J. Majeska, Prevention of fracture healing in rats by an inhibitor of angiogenesis, Bone. 29 (2001) 560–564. https://doi.org/10.1016/S8756-3282(01)00608-1.
[168] B.E. Clausen, C. Burkhardt, W. Reith, R. Renkawitz, I. Förster, Conditional gene targeting in macrophages and granulocytes using LysMcre mice, Transgenic Res. 8 (1999) 265–277. https://doi.org/10.1023/a:1008942828960.
[169] L. Liu, M. Li, L.C. Spangler, C. Spear, M. Veenstra, L. Darnall, C. Chang, A.C. Cotleur, R.M. Ransohoff, Functional defect of peripheral neutrophils in mice with induced deletion of CXCR2: neutrophil CXCR2 Conditional Deletion, Genesis. 51 (2013) 587–595. https://doi.org/10.1002/dvg.22401.
[170] K.J. Jepsen, M.J. Silva, D. Vashishth, X.E. Guo, M.C. van der Meulen, Establishing Biomechanical Mechanisms in Mouse Models: Practical Guidelines for Systematically Evaluating Phenotypic Changes in the Diaphyses of Long Bones, J Bone Miner Res. 30 (2015) 951–966. https://doi.org/10.1002/jbmr.2539.
[171] J. Wang, Neutrophils in tissue injury and repair, Cell Tissue Res. 371 (2018) 531–539. https://doi.org/10.1007/s00441-017-2785-7.

[172] R.M. Devalaraja, L.B. Nanney, Q. Qian, J. Du, Y. Yu, M.N. Devalaraja, A. Richmond, Delayed Wound Healing in CXCR2 Knockout Mice, Journal of Investigative Dermatology. 115 (2000) 234–244. https://doi.org/10.1046/j.1523-1747.2000.00034.x.
[173] D.P. Dyer, K. Pallas, L. Medina-Ruiz, F. Schuette, G.J. Wilson, G.J. Graham, CXCR2 deficient mice display macrophage-dependent exaggerated acute inflammatory responses, Sci Rep. 7 (2017) 42681. https://doi.org/10.1038/srep42681.
[174] R.M. Strieter, P.J. Polverini, S.L. Kunkel, D.A. Arenberg, M.D. Burdick, J. Kasper, J. Dzuiba, J. Van Damme, A. Walz, D. Marriott, S.-Y. Chan, S. Roczniak, A.B. Shanafelt, The Functional Role of the ELR Motif in CXC Chemokine-mediated Angiogenesis, J. Biol. Chem. 270 (1995) 27348–27357. https://doi.org/10.1074/jbc.270.45.27348.
[175] C.L. Addison, T.O. Daniel, M.D. Burdick, H. Liu, J.E. Ehlert, Y.Y. Xue, L. Buechi, A. Walz, A. Richmond, R.M. Strieter, The CXC Chemokine Receptor 2, CXCR2, Is the Putative Receptor for ELR $^{+}$ CXC Chemokine-Induced Angiogenic Activity, J Immunol. 165 (2000) 5269–5277. https://doi.org/10.4049/jimmunol.165.9.5269.